

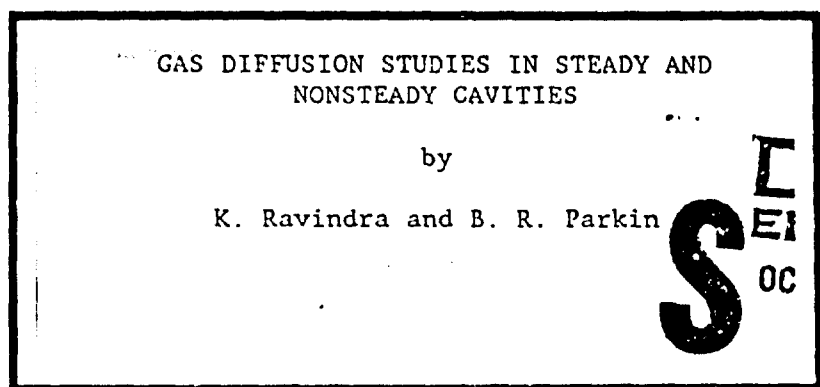
# Applied Research Laboratory

## The Pennsylvania State University

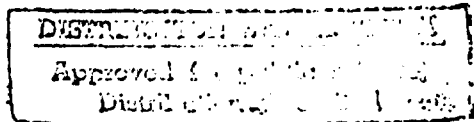
AD-A185 795

DTIC FILE COPY

12



DTIC  
ELECTED  
CCT 13 1987  
S E D



# TECHNICAL REPORT

The Pennsylvania State University  
APPLIED RESEARCH LABORATORY  
P. O. Box 30  
State College, PA 16804

GAS DIFFUSION STUDIES IN STEADY AND  
NONSTEADY CAVITIES

by  
K. Ravindra and B. R. Parkin

DTIC  
SELECTED  
OCT 13 1987  
S D

Technical Report No. TR-87-003  
September 1987

Supported by:  
Naval Sea Systems Command

L. R. Hettche  
Applied Research Laboratory

Approved for public release; distribution unlimited

87 10 6 127

## REPORT DOCUMENTATION PAGE

1a. REPORT SECURITY CLASSIFICATION Unclassified		1b. RESTRICTIVE MARKINGS	
2a. SECURITY CLASSIFICATION AUTHORITY		3. DISTRIBUTION/AVAILABILITY OF REPORT	
2b. DECLASSIFICATION/DOWNGRADING SCHEDULE			
4 PERFORMING ORGANIZATION REPORT NUMBER(S)		5. MONITORING ORGANIZATION REPORT NUMBER(S)	
6a. NAME OF PERFORMING ORGANIZATION Applied Research Laboratory The Penna. State University	6b. OFFICE SYMBOL (if applicable) ARL	7a. NAME OF MONITORING ORGANIZATION Naval Sea Systems Command Department of the Navy	
6c. ADDRESS (City, State, and ZIP Code) P.O. Box 30 State College, PA 16804		7b. ADDRESS (City, State, and ZIP Code) Washington, DC 20362	
8a. NAME OF FUNDING/SPONSORING ORGANIZATION Naval Sea Systems Command	8b. OFFICE SYMBOL (if applicable) NAVSEA	9. PROCUREMENT INSTRUMENT IDENTIFICATION NUMBER	
8c. ADDRESS (City, State, and ZIP Code) Department of the Navy Washington, DC 20362		10. SOURCE OF FUNDING NUMBERS	
		PROGRAM ELEMENT NO.	PROJECT NO.
		TASK NO.	WORK UNIT ACCESSION NO.
11. TITLE (Include Security Classification) Gas Diffusion Studies in Steady and Nonsteady Cavities (Unclassified)			
12. PERSONAL AUTHOR(S) K. Ravindra and B. R. Parkin			
13a. TYPE OF REPORT Ph.D. Thesis	13b. TIME COVERED FROM _____ TO _____	14. DATE OF REPORT (Year, Month, Day) August 1987	15. PAGE COUNT 159
16. SUPPLEMENTARY NOTATION			
17. COSATI CODES		18. SUBJECT TERMS (Continue on reverse if necessary and identify by block number) gaseous diffusion, turbulent entrainment, cavitating flows, gas-liquid interface, two-dimensional flows, hydrofoil oscillation	
19. ABSTRACT (Continue on reverse if necessary and identify by block number)			
<p>These pages present a study of gaseous diffusion into and turbulent entrainment from steady as well as nonsteady fully cavitating flows and characterize the nonsteady cavity as a dynamic element in a water tunnel test section. An approximate theoretical analysis is done for gaseous diffusion across steady axisymmetric cavities. A comparison with experimental results reveals that the present approximate analysis is suited for better estimates of gaseous diffusion across the gas-liquid interface of axisymmetric cavities than past analyses.</p>			
20. DISTRIBUTION/AVAILABILITY OF ABSTRACT <input checked="" type="checkbox"/> UNCLASSIFIED/UNLIMITED <input type="checkbox"/> SAME AS RPT <input type="checkbox"/> DTIC USERS		21. ABSTRACT SECURITY CLASSIFICATION Unclassified	
22a. NAME OF RESPONSIBLE INDIVIDUAL		22b. TELEPHONE (Include Area Code) 814/865-6344	22c. OFFICE SYMBOL

Water tunnel experiments for two-dimensional flows were conducted on cavities behind a stationary and oscillating "flat plate" (wedge) hydrofoil. It is found that the steady cavity pressures were significantly higher than the vapor pressure of water and larger cavities tend to maintain higher cavity pressures. Unsteady cavity pressures were found to be significant only at low frequencies of profile oscillation. Downstream and upstream of the cavity, the oscillating cavity was observed to behave like a dipole source at low frequencies of foil oscillation. An analysis of the oscillating cavity lengths revealed that for sinusoidal motions of the foil, the first two harmonics of the cavity motions are significant.

A mathematical model is then developed to estimate the nonsteady gaseous entrainment behind two-dimensional steady and oscillating cavities. This model takes into account the varying gas pressure as well as varying cavity lengths. It is observed that this model has the proper steady state limit. Steady and nonsteady gas entrainment rates were estimated for the two-dimensional cavity. It is found that gas pressure within the cavity affects the steady entrainment behind the cavity. The phase angle between the foil motion and cavity motion is determined by a physically driven argument that is seen to be consistent with experimental observations. The nonsteady gaseous entrainment behind the cavity is seen to depend only on the cavity volume fluctuations and cavity gas pressure fluctuations.



Accession For	
NTIS	CRA&I <input checked="" type="checkbox"/>
DTIC	TAB <input type="checkbox"/>
Unannounced <input type="checkbox"/>	
Justification .....	
By .....	
Distribution /	
Availability Codes	
Dist	Avail. publ. or Specified
A-1	

## ABSTRACT

These pages present a study of gaseous diffusion into and turbulent entrainment from steady as well as nonsteady fully cavitating flows and characterize the nonsteady cavity as a dynamic element in a water tunnel test section. An approximate theoretical analysis is done for gaseous diffusion across steady axisymmetric cavities. A comparison with experimental results reveals that the present approximate analysis is suited for better estimates of gaseous diffusion across the gas-liquid interface of axisymmetric cavities than past analyses.

Water-tunnel experiments for two-dimensional flows were conducted on cavities behind a stationary and oscillating "flat plate" (wedge) hydrofoil. It is found that the steady cavity pressures were significantly higher than the vapor pressure of water and larger cavities tend to maintain higher cavity pressures.

Unsteady cavity pressures were found to be significant only at low frequencies of profile oscillation. Downstream and upstream of the cavity, the oscillating cavity was observed to behave like a dipole source at low frequencies of oscillation and like a quadrupole source at high frequencies of foil oscillation. An analysis of the oscillating cavity lengths revealed that for sinusoidal motions of the foil, the first two harmonics of the cavity motions are significant.

A mathematical model is then developed to estimate the nonsteady gaseous entrainment behind two-dimensional steady and oscillating cavities. This model takes into account the varying gas

pressure as well as varying cavity lengths. It is observed that this model has the proper steady state limit. Steady and nonsteady gas entrainment rates were estimated for the two-dimensional cavity. It is found that gas pressure within the cavity affects the steady entrainment behind the cavity. The phase angle between the foil motion and cavity motion is determined by a physically driven argument that is seen to be consistent with experimental observations. The nonsteady gaseous entrainment behind the cavity is seen to depend only on the cavity volume fluctuations and cavity gas pressure fluctuations.

## TABLE OF CONTENTS

	<u>Page</u>
ABSTRACT . . . . .	iii
LIST OF TABLES . . . . .	viii
LIST OF FIGURES . . . . .	ix
LIST OF SYMBOLS . . . . .	xi
ACKNOWLEDGMENTS . . . . .	xiv
<u>Chapter</u>	
1. INTRODUCTION . . . . .	1
1.1 Preliminary . . . . .	1
1.2 Cavity Aspects . . . . .	2
1.3 Scope of Present Investigation . . . . .	6
2. GASEOUS DIFFUSION STUDIES ACROSS AN AXISYMMETRIC PERMEABLE CAVITY SURFACE . . . . .	10
2.1 Introduction . . . . .	10
2.2 Convective Slug Flow Model for Mass Diffusion Rate Estimation . . . . .	12
2.3 Modified Parkin Model . . . . .	14
2.4 Mathematical Analysis . . . . .	21
2.5 Recapitulation . . . . .	32
3. EXPERIMENTAL INVESTIGATION OF THE BEHAVIOR OF NONSTEADY CAVITIES BEHIND A WEDGE OSCILLATING IN PITCH . . . . .	33
3.1 Introduction . . . . .	33
3.2 Experimental Apparatus . . . . .	34
3.2.1 Six-Inch Water Tunnel . . . . .	34
3.2.2 Model and Shaft . . . . .	35
3.2.3 Drive System . . . . .	35
3.2.4 Instrumentation . . . . .	37

## TABLE OF CONTENTS [continuation]

<u>Chapter</u>	<u>Page</u>
3.3 Test Procedure . . . . .	43
3.3.1 Video Recording of Cavity Motion . . . . .	43
3.3.2 Source-Like Nature of Cavities . . . . .	43
3.3.3 Measurement of Cavity Pressures . . . . .	44
3.4 Test Results and Discussion . . . . .	44
3.4.1 Cavity Length History . . . . .	46
3.4.2 Source-Like Nature of Cavities . . . . .	56
3.4.3 Cavity Pressure Measurements . . . . .	61
3.4.4 Recapitulation . . . . .	69
4. TWO-DIMENSIONAL UNSTEADY DIFFUSION ACROSS A PERMEABLE CAVITY SURFACE . . . . .	70
4.1 Introduction . . . . .	70
4.2 Assumptions . . . . .	70
4.3 Theoretical Analysis . . . . .	71
4.4 Recapitulation . . . . .	82
5. A STUDY OF NONSTEADY CAVITY CLOSURE . . . . .	83
5.1 Introduction . . . . .	83
5.2 Steady Cavity Closure. . . . .	84
5.3 Nonsteady Cavity Closure, Phase Relations . . . . .	86
5.4 Nonsteady Cavity Closure, Entrainment Rates . . . . .	90
5.5 Recapitulation . . . . .	97
6. CONCLUSIONS AND RECOMMENDATIONS . . . . .	99
BIBLIOGRAPHY . . . . .	102

## TABLE OF CONTENTS [continuation]

	<u>Page</u>
APPENDIX A. DETAILS OF AXISYMMETRIC DIFFUSION ANALYSIS . . . . .	107
A.1 Asymptotic Evaluation of Integral . . . . .	108
A.2 Simplification of Integral Equations . . . . .	112
A.3 Solution of Eq. (2.22a) . . . . .	115
A.4 Solution of Eq. (2.21a) . . . . .	117
APPENDIX B. EXPERIMENTAL RESULTS AND ANALYSIS . . . . .	118
B.1 Sample Data Corresponding to Figure 3.14 . . . . .	119
B.2 Measurement of Free Air Content in the Test Section . . . . .	120
B.3 Analysis of Experimental Error . . . . .	122
B.4 Wall Effect Correction for Cavitation Number . . . . .	125
APPENDIX C. DETAILS OF UNSTEADY DIFFUSION ANALYSIS . . . . .	127
C.1 Fundamental Solution of Eq. (4.13b) . . . . .	128
C.2 Inverse Laplace Transform . . . . .	132
C.3 Integral Evaluation . . . . .	134
APPENDIX D. SENSITIVITY ANALYSIS FOR MASS DIFFUSION RATE . . .	136
APPENDIX E. UNSTEADY ENTRAINMENT DATA AND CALCULATIONS . . . . .	138
E.1 Quasi-Steady Concentration Fluctuation Amplitude . . . . .	139
E.2 Evaluation of $\partial m / \partial t$ in Eq. (5.16b) . . . . .	140
E.3 Unsteady Entrainment Sample Calculation . . . . .	141
E.4 Unsteady Entrainment Data . . . . .	143

## LIST OF TABLES

<u>Table</u>	<u>Page</u>
2.1 Comparison of mass flow rates . . . . .	15

## LIST OF FIGURES

<u>Figure</u>		<u>Page</u>
2.1	Slug Flow Model for Estimating the Gaseous Diffusion across an Axisymmetric Cavity . . . . .	13
2.2	Flow Coefficient versus Cavitation Number, $U_\infty = 1830 \text{ cm/sec}$ . . . . .	18
2.3	Flow Coefficient versus Cavitation Number, $U_\infty = 910 \text{ cm/sec}$ . . . . .	19
2.4	Concentration Layer Profile over a Two-Dimensional Cavity . . . . .	20
2.5	Idealized Cavity Geometry and Boundary Conditions . . . . .	23
2.6	Ring Source Geometry . . . . .	26
3.1	Foil Shaft Assembly . . . . .	36
3.2	Frequency Response of Pitch Drive Assembly . . . .	38
3.3	Typical Cavity behind Wedge Foil . . . . .	39
3.4	Frequency Response of Crystal Transducer . . . .	40
3.5	Schematic of Apparatus for Sound Speed Measurement . . . . .	42
3.6	Variation of Pressure along the Length of the Tunnel due to an Elliptical Cavity . . . . .	45
3.7(a)	Time History of Cavity Motion, 0.5 Hz . . . . .	48
3.7(b)	Time History of Cavity Motion, 1.0 Hz . . . . .	49
3.7(c)	Time History of Cavity Motion, 3.0 Hz . . . . .	50
3.7(d)	Time History of Cavity Motion, 5.0 Hz . . . . .	51
3.8(a)	Spectrum of Cavity Motion, 0.5 Hz . . . . .	52
3.8(b)	Spectrum of Cavity Motion, 1.0 Hz . . . . .	53
3.8(c)	Spectrum of Cavity Motion, 3.0 Hz . . . . .	54
3.8(d)	Spectrum of Cavity Motion, 5.0 Hz . . . . .	55

## LIST OF FIGURES [continuation]

<u>Figure</u>		<u>Page</u>
3.9	Cavity Length Amplitude versus Reduced Frequency . . . . .	57
3.10	R.M.S. Pressure Level at 32.5 Inches Upstream versus Test Section Velocity . . . . .	58
3.11	R.M.S. Pressure Level 32.5 Inches Upstream versus Test Section Velocity . . . . .	59
3.12	R.M.S. Pressure Level at 32.5 Inches Downstream versus Test Section Velocity . . . . .	60
3.13	R.M.S. Pressure Level at 16.325 Inches Upstream versus Test Section Velocity . . . . .	62
3.14	Normalized Steady Cavity Pressure versus $\sigma/\alpha$ . . .	63
3.15	Normalized Steady Cavity Pressure versus $k'$ . . .	64
3.16	Normalized Unsteady Cavity Pressure versus $k'$ , $\alpha = 15^\circ$ . . . . .	67
3.17	Normalized Unsteady Cavity Pressure versus $k'$ , $\alpha = 8^\circ$ . . . . .	68
4.1	Boundary Conditions for Unsteady Gaseous Diffusion Analysis . . . . .	72
5.1	Entrainment Rate Behind a Steady Two-Dimensional Cavity . . . . .	87
5.2a	Two-Dimensional Cavity Around an Oscillating Hydrofoil. . . . .	88
5.2b	Physical Plane Representation of Linearized Two-Dimensional Cavity . . . . .	88
5.3	Unsteady Entrainment Amplitude versus Reduced Frequency . . . . .	96

## LIST OF SYMBOLS

A = constant [see Eq. (2.14)]  
A<sub>T</sub> = exchange coefficient  
a = radius of axisymmetric cavity  
 $\bar{b}$  = characteristic length  
C = absolute concentration at a field point  
C<sub>∞</sub> = concentration of dissolved gases in the free stream  
C<sub>0</sub> = concentration on the permeable surface  
c = concentration difference  
 $\bar{c}$  = time mean concentration difference  
c<sub>0</sub> = C<sub>0</sub> - C<sub>∞</sub>  
F = Laplace transform of source strength distribution f  
f = source strength distribution; frequency of oscillation, Hertz  
I<sub>0</sub> = modified Bessel's function of zeroth order, second kind  
j =  $\sqrt{-1}$   
K<sub>0</sub> = modified Bessel's function of zeroth order, first kind  
k = mass conductivity; reduced frequency  
k' = modified reduced frequency  
L = cavity length  
 $\bar{L}$  = non-dimensional cavity length  
 $\bar{L}_0$  = steady cavity length  
 $\dot{m}$  = dm/dt, mass flow rate of gases  
P<sub>FS</sub> = partial pressure of gas in the free stream  
p = pressure  
p<sub>c</sub> = cavity pressure  
p<sub>G</sub> = cavity gas pressure  
p<sub>∞</sub> = free stream static pressure

## LIST OF SYMBOLS [continuation]

$p_v$  = vapor pressure  
 $q$  = source strength  
 $q_c$  = celerity of cavity surface waves  
 $R$  = radial coordinate; non-dimensional number =  $\frac{U_\infty b}{2v}$   
 $r$  = non-dimensional radial coordinate; lag function  
 $r'$  = distance between field point and origin  
 $r''$  = distance between source point and field point  
 $s$  = Laplace variable  
 $t$  = time  
 $U_\infty$  = velocity in the X direction  
 $u$  = instantaneous velocity fluctuation in the X-direction  
 $v$  = instantaneous velocity fluctuation in the Y-direction  
 $w$  = instantaneous velocity fluctuation in the Z-direction  
 $x$  = non-dimensional X coordinate  
 $y$  = non-dimensional Y coordinate  
 $z$  = non-dimensional Z coordinate  
 $\alpha$  = angle of attack  
 $\bar{\alpha}$  = complex constant  
 $\alpha_1$  = dissolved gas content in ppm  
 $\beta$  = Henry's law constant  
 $\epsilon$  = amplitude of cavity oscillation  
 $\delta$  = turbulent boundary layer thickness  
 $\phi$  = phase angle between foil motion and cavity length motion  
 $\phi_a$  = phase angle between foil motion and cavity pressure fluctuations  
 $\phi_e$  = phase angle between foil motion and entrainment rate fluctuations

## LIST OF SYMBOLS [continuation]

$\theta$  = angular measure in  $\eta$ ,  $\xi$  plane  
 $\kappa$  = molecular mass diffusivity  
 $\lambda$  =  $U_a/2\kappa$ , a dimensionless parameter  
 $v_t$  = eddy mass diffusivity  
 $\rho$  = density  
 $\sigma$  = cavitation number  
 $\sigma_0$  = cavitation number based on vapor pressure

## ACKNOWLEDGMENTS

The author wishes to express his sincere appreciation to Professor Blaine R. Parkin for suggesting the problem and all the patient discussions on the subject. The help provided by Mr. George B. Gurney and Mr. George F. Sayers during various phases of the experimental investigation is sincerely acknowledged. The experimental investigation itself could not have been carried out but for the generous help extended by the tunnel crew. The author is indebted to the Applied Research Laboratory, The Pennsylvania State University, and the United States Navy for making this research possible through E/F Grant No. 6171. The research funds, provided by the Long Range Planning and Development Committee of Dowling College, are gratefully acknowledged. The author wishes to thank sincerely Mrs. Leanne Zindler, Mrs. Lynne Stewart, and Mrs. Helen Williams for their expert typing of this manuscript.

## CHAPTER 1

### INTRODUCTION

#### 1.1 Preliminary

In many liquid flow systems, some form of unsteady cavity flow exists at one or more locations in the circuit. Such unsteady cavity flow may arise intentionally as in the case of water tunnel experiments on nonsteady cavity flows or unintentionally as in the case of high speed, high performance turbomachines in various liquid flow systems such as nuclear reactors and liquid rocket engines. In any case, the presence of an unsteady cavity within a liquid might create disturbances that could tend to make the system unstable. The propagation of such disturbances becomes even more significant when small gas bubbles are present in the liquid, wherein the acoustic celerity of the gas-liquid mixture is greatly reduced. A classic example is the "POGO" instability observed in liquid rocket engines (1,2). In closed circuit water tunnel operation involving unsteady cavity flow experimentation, mass oscillations of the entire circuit and "breathing of the tunnel" have been reported (3-5). In order to obtain valid nonsteady force measurements involving cavity flow in closed circuit water tunnels, the nature of the unsteady cavity as a disturbance source and the dynamics of the water tunnel itself must be clearly understood.

It is the purpose of this thesis to examine the physical aspects (such as gaseous diffusion into the cavity and its turbulent entrainment into the cavity wake) that govern the nature of unsteady

cavities so that system responses to unsteady cavity flows may be more accurately predicted and related to force measurements on oscillating struts and foils. This latter aspect, involving the dynamics of any particular facility, is outside the scope of this study, however.

### 1.2 Cavity Aspects

Whenever the local pressure in a region within the liquid falls below the vapor pressure of the liquid at the ambient temperature, the liquid evaporates and a cavity is formed. The size and shape of the cavity is governed by the cavity pressure and the shape and attitude of the body on which the cavity is formed. The cavity is usually characterized by a quantity known as the "cavitation number" which is defined as:

$$\sigma = \frac{p_{\infty} - p_c}{1/2 \rho_{\infty} U_{\infty}^2} , \quad (1.1)$$

where

$\sigma$  = cavitation number,

$p_{\infty}$  = free stream static pressure,

$p_c$  = cavity pressure,

$\rho_{\infty}$  = free stream density of the liquid,

$U_{\infty}$  = free stream velocity.

In a purely vaporous cavity, the cavity pressure is equal to the vapor pressure of the liquid at the ambient temperature of the liquid. Gadd and Grant (6), among others, have demonstrated that the measured cavity pressure,  $p_c$ , within fully developed natural cavities exceeds the liquid vapor pressure,  $p_v$ , because of the unavoidable presence of

gases dissolved in the liquid. These gases diffuse through the cavity interface and set up a partial pressure of gas  $p_G$ , in the cavity so that

$$p_c = p_v + p_G . \quad (1.2)$$

Thus, the presence of dissolved gases in the liquid affect the cavitation number  $\sigma$  and the behavior of the cavity itself to a great extent.

The influence of dissolved gases on the behavior of single bubble cavities, viz., growth and collapse, has been the subject of many previous investigations. Epstein and Plesset (7) studied the stability of gas bubbles in liquid gas solutions. Parkin and Kermeen (8) studied steady gaseous molecular diffusion into a microbubble. They investigated the influence of gaseous diffusion on the growth of small bubbles in a flow field containing dissolved gases. In cavity flows, when the boundary layer on the cavity surface is turbulent, Brennen (9) has shown that turbulent gaseous diffusion into the cavity may be more significant than molecular diffusion. Brennen (9) also extended his two-dimensional theory to include the gaseous diffusion across an axisymmetric cavity by wrapping the two-dimensional solution around the cavity.

Several experimental investigations have been devoted to the understanding of gaseous diffusion across steady cavities (10-13). A majority of these studies are devoted to the understanding of axisymmetric cavities because of frequent occurrence of such shapes in marine applications. Swanson and O'Neill (10) investigated the stability aspects of ventilated cavities behind circular discs in

steady flow. Cox and Clayden (11) studied the air entrainment behind cavities. Billet and Weir (13) measured the entrainment rates behind ventilated axisymmetric cavities.

The unsteadiness of a cavity arise in two distinct forms. The first one is the auto oscillation of steady cavities (particularly the ventilated cavities) that is prevalent at certain cavitation numbers. This phenomenon has been studied in great detail by Song (14) and Silberman and Song (15). The second form is the forced oscillation of the cavity due to the oscillation of the body on which the cavity is formed. Typical examples are a cavity behind an oscillating hydrofoil and a cavity on a propeller blade. The oscillations of the cavity may be classified into two distinct forms of motion (16): First, the motion of the cavity wherein the volume of the cavity changes significantly; second, the motion of the cavity wherein the shape of the cavity changes significantly but the cavity volume remains essentially constant. As the cavity volume changes, the partial pressure of gas inside the cavity changes. Since the time scale of the process of vapor release and absorption is very much smaller than the period of cavity oscillations typically encountered, the vapor pressure inside the cavity essentially remains constant. Thus the cavity pressure within an oscillating cavity may be written as

$$p_c(t) = p_v + p_G(t) , \quad (1.3)$$

where  $p_G(t)$  is the cavity gas pressure. Then the cavitation number  $\sigma(t)$  of an oscillating cavity is given by

$$\sigma(t) = \sigma_0 - \frac{p_G(t)}{1/2 \rho_\infty U_\infty^2} , \quad (1.4)$$

where  $\sigma_0$  is the cavitation number based on the vapor pressure of the liquid. Jiang and Leehey (17) have measured the cavity pressure within an oscillating cavity behind an elliptical wing oscillating in pitch. They found that the unsteady cavity pressure depends on the frequency of oscillation and that the unsteady pressures are significant at low frequencies of oscillation.

One of the earliest models used in characterizing the unsteady cavity as a source of disturbances in fluid flow system was in connection with the analysis of "POGO" instability in liquid rocket engines. By defining a quantity called "cavitation compliance" which relates the mass flow fluctuations and the corresponding pressure fluctuations, Rubin (2) was able to model the oscillating cavitating bubble as a simple spring mass system. Brennen and Acosta (18) showed that Rubin's model for a cavitating pump inducer is rather simple. The results of their experimental investigation revealed appreciable departure from Rubin's quasi-steady model due to dynamic effects at high frequency. Huse (16), in an attempt to predict cavitation damage on the hull of a ship due to a cavitating propeller, represented the unsteady cavity at the tip of the propeller as a combination of acoustic monopole and dipole sources. His analytical results compared well with the experiments.

### 1.3 Scope of Present Investigation

The gas pressure within the cavity is a quantity of fundamental importance in steady and nonsteady cavity flows. The gas pressure within the cavity dictates the amount of gas diffusion across the cavity surface. Hence we seek to describe the diffusion phenomenon analytically and to compare the results with the best available experimental data. To our knowledge, the data of Billet and Weir (13) are the best available and they pertain to axisymmetric flows.

In Chapter 2 we first demonstrate using a heuristic model, the lack of correlation between existing mathematical models for gaseous diffusion across axisymmetric cavities and corresponding experimental results. Then, we use the convective diffusion theory proposed by Parkin (8) with the molecular diffusivity being replaced by a turbulent diffusivity to predict the gaseous diffusion across an axisymmetric cavity surface. We then show that two-dimensional gaseous diffusion models cannot always be used to predict gaseous diffusion across axisymmetric cavities. This naturally led us to the formulation of convective diffusion of gases for axisymmetric cavity shapes. We solve the steady diffusion equation in cylindrical coordinates as it applies to the gaseous diffusion across an axisymmetric cavity surface. Although the general solution of the governing differential equation is fairly straightforward, the peculiar set of boundary conditions for the present idealized representation of the flow and cavity of interest here makes the problem challenging.

The solution of the problem is built up by superposition starting from the known point source solution in a moving fluid. First, we use

the point source solution to derive the solution to the governing differential equation for a "unit ring source." Second, we integrate the ring source of unknown strength over the length of the doubly infinite circular cylinder in the streamwise direction. The application of boundary conditions on this cylindrical cavity surface results in a system of integral equations which must be solved in order to determine the source strength. From this solution, the mass flow rate of gases diffusing across the cavity may be obtained.

As pointed out by Greitzer (20), there is a general lack of theoretical and experimental results available in the literature that characterize the unsteady cavity as an active dynamic element. Therefore, an effort was made to understand the behavior of unsteady cavities experimentally in this study. We conducted experiments on a cavitating wedge foil oscillating in pitch. Specifically, we were interested in measuring the cavity lengths and cavity pressures (steady and nonsteady) as a function of oscillation frequency and characterizing the source-like nature of oscillating cavities. We found that an oscillating cavity has the behavior of a dipole source and that the unsteady cavity pressures are significant at low frequencies of oscillation. We also found that the motion of the cavity is far from being sinusoidal even though the motion of the foil was sinusoidal. In particular, the first harmonic overtone was found to be significant. In Chapter 3 the details of this experimental investigation are presented and the results are discussed.

The experimental results presented in Chapter 3 as well as those of Jiang and Leehey (17) have indicated clearly the effect of non-condensable gas on the behavior of an unsteady cavity. While several investigations in the past have addressed the effect of steady gaseous diffusion into the cavity, there is very little literature, if any, that deals with the analysis of unsteady diffusion across cavity surfaces. In Chapter 4, we formulate and solve the two-dimensional unsteady diffusion problem. The problem, as formulated, accounts for both the cavity pressure fluctuations and cavity length fluctuations. The solution of the unsteady diffusion equation is obtained by the separation of variables. The expression for mass diffusion rate is obtained in a manner similar to the method outlined by Parkin (8) for steady two-dimensional flow. The result for unsteady mass diffusion rate across a two-dimensional cavity surface matches the steady state solution predicted by Parkin (8) in the limit when the frequency of cavity oscillation vanishes.

In Chapter 5, we consider the two dimensional steady cavity closure as well as nonsteady cavity closure condition when the cavity is not purely vaporous. The steady closure condition is seen to be rather straightforward to formulate and analyze. In analyzing the nonsteady gaseous cavity closure, we find that it is important to consider the phase differences that exist between the body motion and i) cavity volume (or almost equivalently the cavity length) fluctuation, ii) the unsteady gaseous diffusion through the entire cavity surface, and iii) gas pressure fluctuation within the cavity respectively. In the absence of any available theoretical or experimental data on the phase lag between the body motion and cavity

length motion, we appeal to a physically driven argument that cavity surface waves originating from the upper surface and lower surface of a foil must terminate at the same point at the same instant. This results in the phase lag being numerically equal to the modified reduced frequency of foil oscillation. The nonsteady gaseous cavity closure is then formulated using the nonsteady continuity equation. With the help of the experimental data reported above, continuity enables the determination of magnitude and phase of the nonsteady entrained gas behind the cavity in terms of the reduced frequency of oscillation  $k'$ , the nonsteady mass diffusion through the cavity surface, the cavity pressure fluctuations and the cavity volume fluctuations.

The reader will find that an analytical approach has been used throughout the present study. The reason for this being, analytical solutions render better physical insight than numerical solutions.

## CHAPTER 2

GASEOUS DIFFUSION STUDIES ACROSS AN AXISYMMETRIC  
PERMEABLE CAVITY SURFACE2.1 Introduction

A thorough analysis of the gaseous diffusion process across a cavity surface is fundamental to the understanding of both natural and ventilated cavity flows because diffusion into or out of the liquid can influence the cavity pressure to a great extent. Analysis of gaseous diffusion across axisymmetric cavity surfaces is of particular interest because of the frequent occurrence of such cavity flows in marine applications.

Steady diffusion of gases across a two-dimensional cavity has been studied by Parkin (8). Parkin used this planar solution to approximate the rate of molecular diffusion into a microbubble. Brennen (9) considered turbulent gaseous diffusion into a large two-dimensional cavity by using a model which assumes that the turbulence is associated with the turbulent shear layer on the cavity surface. Billet and Weir (13) have attempted to use Brennen's model to predict the rate of diffusion across axisymmetric cavity surfaces. They found when Brennen's two-dimensional solution is extended to the axisymmetric case by wrapping the two-dimensional solution around the cavity, that the observed diffusion rate exceeds the analytical prediction by nearly one order of magnitude. They circumvented this discrepancy by using their experimental data to choose a constant multiplicative factor in Brennen's model.

Brennen's solution assumes that the diffusion occurs through the turbulent eddies within the turbulent boundary layer on the cavity surface. Hence Brennen's solution is applicable only where the boundary layer has had a chance to grow on the surface of the body before a cavity is formed, as for example, behind the trailing edge of a hydrofoil. But in cases where the cavity emerges from the leading edge of a hydrofoil at small angle of attack or the cavity is on a zero caliber ogive as in the experiments of Billet and Weir, the boundary layer on the cavity near the leading edge is laminar and very thin; and since the cavity surface is then a laminar free shear layer, the rate of growth of this part of the boundary layer is small. For such flows it appears as though a different approach has to be followed in modeling the turbulent diffusion phenomenon. In many cases, this laminar shear layer is of short axial extent and the shear layer is turbulent thereafter.

In this chapter, an attempt is made to clear some of the discrepancies observed by Billet and Weir (13) in their effort to compare their measurements with Brennen's theory. A convective slug flow model is first used to estimate the maximum possible mass convective diffusion rate of gas through the turbulent boundary layer on the axisymmetric cavity surface. These estimates are then compared with the experimental results of Billet and Weir (13) and Brennen's theory. Then, a turbulent diffusivity (that is representative of free shear flows) is used instead of molecular diffusivity as in Parkin's model, to compare with the experimental results. A mathematical model is then formulated for gaseous diffusion across an axisymmetric cavity surface.

## 2.2 Convective Slug Flow Model for Mass Diffusion Rate Estimation

Brennen's theory assumes that all of the diffusion occurs from turbulent eddies that are within the boundary layer. For cavity flows wherein the cavity emerges from the leading edge, the boundary layer on the cavity surface is very thin and Brennen's theory may not quite be applicable. In order to demonstrate whether or not Brennen's theory is applicable in such situations and to assist speculations about other possible mechanisms for gaseous diffusion in cavity flows, the following conservative estimates are carried out using a slug flow model.

We assume that the quantity of dissolved gases available for diffusion is contained within a volume of liquid determined by the maximum thickness of the turbulent boundary layer and the length of the cavity as shown in Figure 2.1. We also assume that all gas in this volume diffuses into the cavity instantaneously and then the slug of volume in the shape of a hollow cylinder of mean radius "a," length "L" and thickness " $\delta$ ," equal to the maximum shear layer thickness at the cavity terminus, is swept downstream and a fresh supply of gases becomes available every  $L/U_{\infty}$  seconds.

If we denote by  $c$ , the concentration difference across the cavity surface, the maximum possible diffusion rate is estimated as

$$\dot{M} = (2\pi a L \delta) c (U_{\infty} / L)$$

or

$$\dot{M} = 2\pi a U_{\infty} \delta c . \quad (2.1)$$

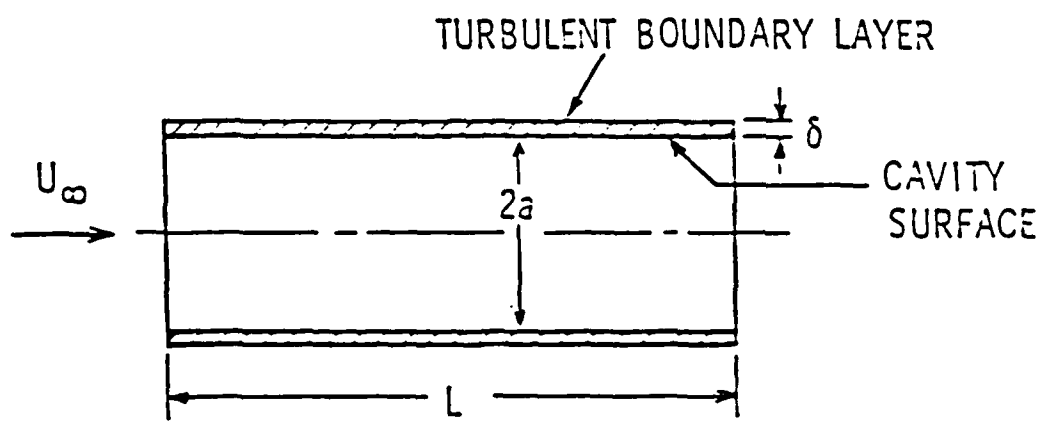


Figure 2.1. Slug Flow Model for Estimating the Gaseous Diffusion across an Axisymmetric Cavity.

The mass diffusion rates predicted by the slug-flow model are shown in Table 2.1 for cavities behind zero caliber ogive models. Also shown in the table are the experimental values of mass diffusion rates from Billet and Weir (13) and the mass diffusion rates predicted by Brennen's theory (9). A comparison of the diffusion rates predicted by the slug-flow model and the experiments shows that even by conservative estimates, the maximum gas diffusion possible through the turbulent boundary layer is nearly one order of magnitude less than the experimentally observed values.

### 2.3 Modified Parkin Model

Following the analysis in Ref. (8), the mass diffusion rate across a two-dimensional cavity surface, with the molecular diffusivity  $\kappa$  being replaced by a turbulent diffusivity  $v_t$  is given by

$$\dot{M}_{2D} = \frac{4\rho v_t c}{\sqrt{\pi}} \left[ \sqrt{2\lambda l} - \frac{\sqrt{\pi}}{2} \right] , \quad (2.2)$$

where

$\dot{M}$  = mass flow rate per unit cavity width

$\rho$  = density of water

$v_t$  = turbulent diffusivity

$c$  = concentration difference

$\lambda$  =  $U_\infty a / 2v_t$

$l$  = length of two-dimensional cavity.

Table 2.1. Comparison of Mass Flow Rates

Cavitation Number	Diameter of Ogive: 0.635 cms			Diameter of Ogive: 0.635 cms		
	$U = 1839 \text{ cms/sec}$			$U = 910 \text{ cms/sec}$		
	$c = 14.5 \times 10^{-6}$			$c = 14.5 \times 10^{-6}$		
Slug Flow Model in	Billet & Weir (13) in	Brennen (9) in	Slug Flow Model in	Billet & Weir (13) in	Brennen (9) in	Brennen (9) in
0.15	0.0036	0.032	0.004	0.0018	0.024	0.005
0.20	0.0033	0.024	0.003	0.00162	0.018	0.0038
0.25	0.003	0.019	0.0023	0.00151	0.014	0.0031
0.30	0.0029	0.016	0.0021	0.00142	0.012	0.0026
0.35	0.0027	0.014	0.0018	0.00134	0.010	0.0023

Wrapping the two-dimensional solution around an axisymmetric cavity of radius "a," one can write the mass flow rate across an axisymmetric cavity as

$$\dot{M} = 8\rho v_t c \sqrt{\pi} a \left[ \sqrt{2\lambda l} - \frac{\sqrt{\pi}}{2} \right] . \quad (2.3)$$

For a zero caliber ogive, the non-dimensional cavity length  $l$  and cavity radius is related to the cavitation number  $\sigma$  by the relations\*

$$l = \frac{0.955}{\sigma} , \quad (2.4a)$$

and

$$a = \frac{0.715}{0.34} D . \quad (2.4b)$$

In Eq. (2.4b),  $D$  represents the diameter of the axisymmetric ogive body. With Eqs. (2.4) substituted in Eq. (2.3),

$$\dot{M} = 10.14 \rho c D v_t \sigma^{0.34} [1.382 \lambda^{1/2} \sigma^{-1/2} - 0.886] . \quad (2.5)$$

We now devise a turbulent diffusivity parameter  $v_t$  characteristic of a free shear layer as

$$v_t \sim l_m \sqrt{\frac{v^2}{v^2}} \quad (2.6)$$

where

$$\sqrt{\frac{v^2}{v^2}} = \text{r.m.s. turbulence level}$$

$$l_m = \text{mixing length.}$$

---

\*(See, for example, Billet, M. L., J. W. Holl and D. S. Weir, "Geometric Description of Developed Cavities on Zero and Quarter Caliber Ogive Bodies," ARL/PSU TM 74-136 [1974].)

For a planar mixing layer\*

$$l_m \sim 0.076 , \quad (2.7a)$$

and

$$\sqrt{\frac{v^2}{2}} \sim 0.09U_\infty , \quad (2.7b)$$

where  $\delta$  is the layer thickness. Therefore we will take

$$v_t = 0.0063 \delta U_\infty \gamma . \quad (2.7c)$$

In the following comparison, the constant of proportionality  $\gamma$  is taken to be unity. Figures 2.2 and 2.3 show the variation of volume flow rates predicted by Eq. (2.5) and the corresponding experimental values of Billet and Weir (13). It is observed that the theoretical and experimental values compare well; at least they are of the same order of magnitude! This good agreement is to be expected if it is recognized that near the leading edge (where the concentration gradients are very high) the boundary layer thickness is very small and thus extension of a two-dimensional result to axisymmetric cases appears to give a good approximation even though the concentration layer is comparable to the cavity radius at the tail end of the cavity (see Figure 2.4 below).

---

\*See, for example, Launder, B. E. and D. B. Spalding, Mathematical Models for Turbulence, Academic Press [1972].

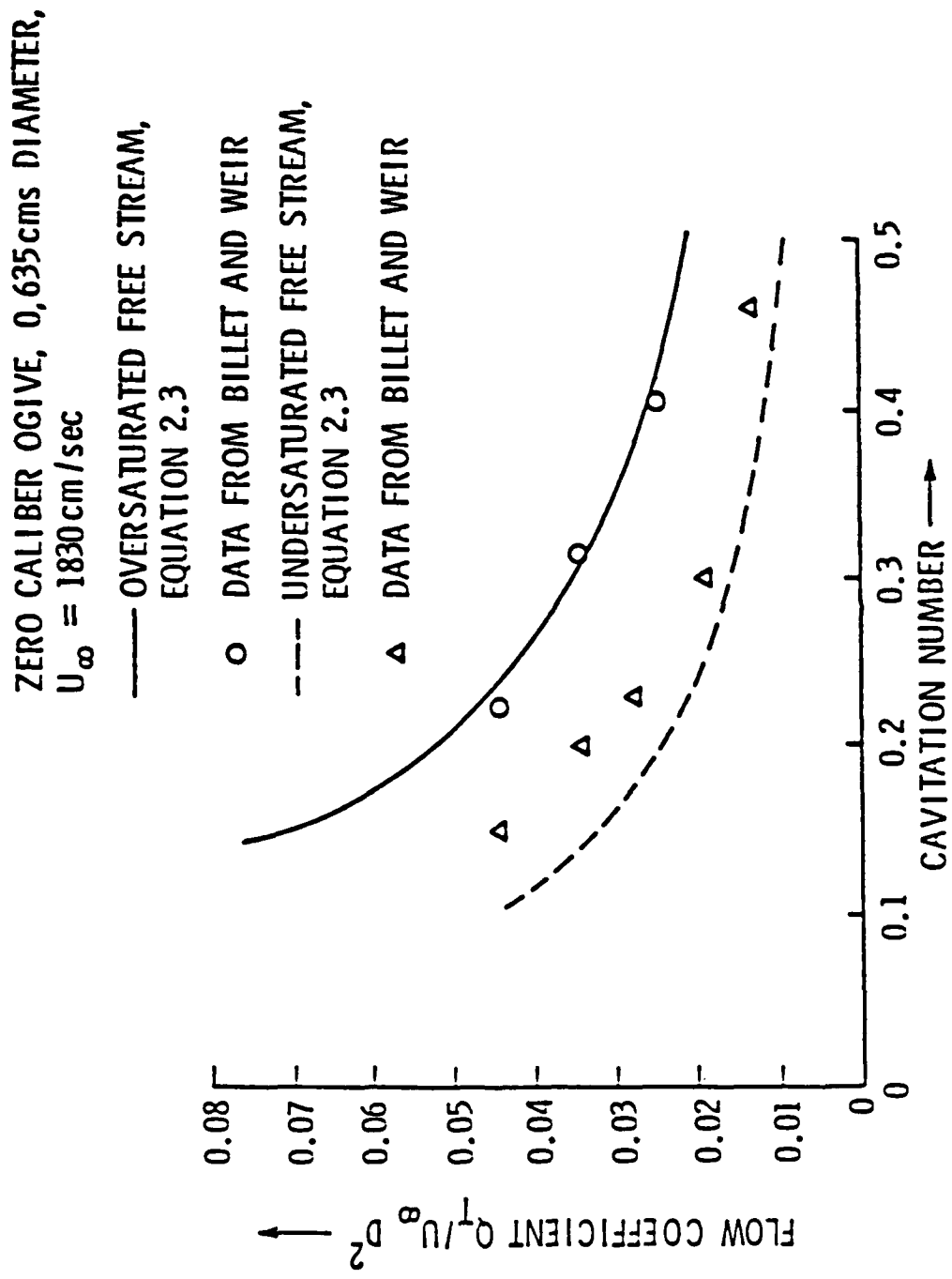


Figure 2.2 Flow Coefficient versus Cavitation Number,  $U_{\infty} = 1830 \text{ cm/sec}$ .

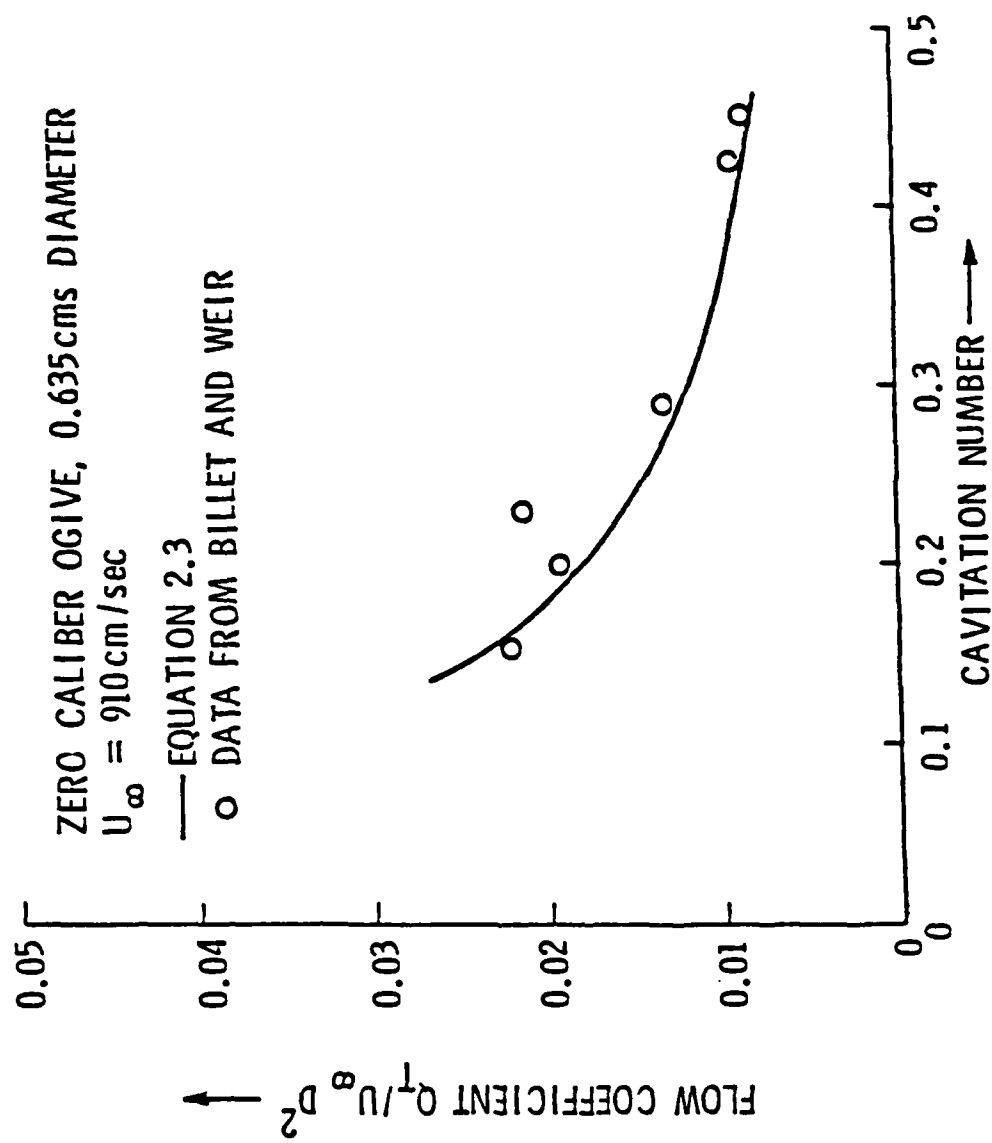


Figure 2.3 Flow Coefficient versus Cavitation Number,  $U_\infty = 910 \text{ cm/sec.}$

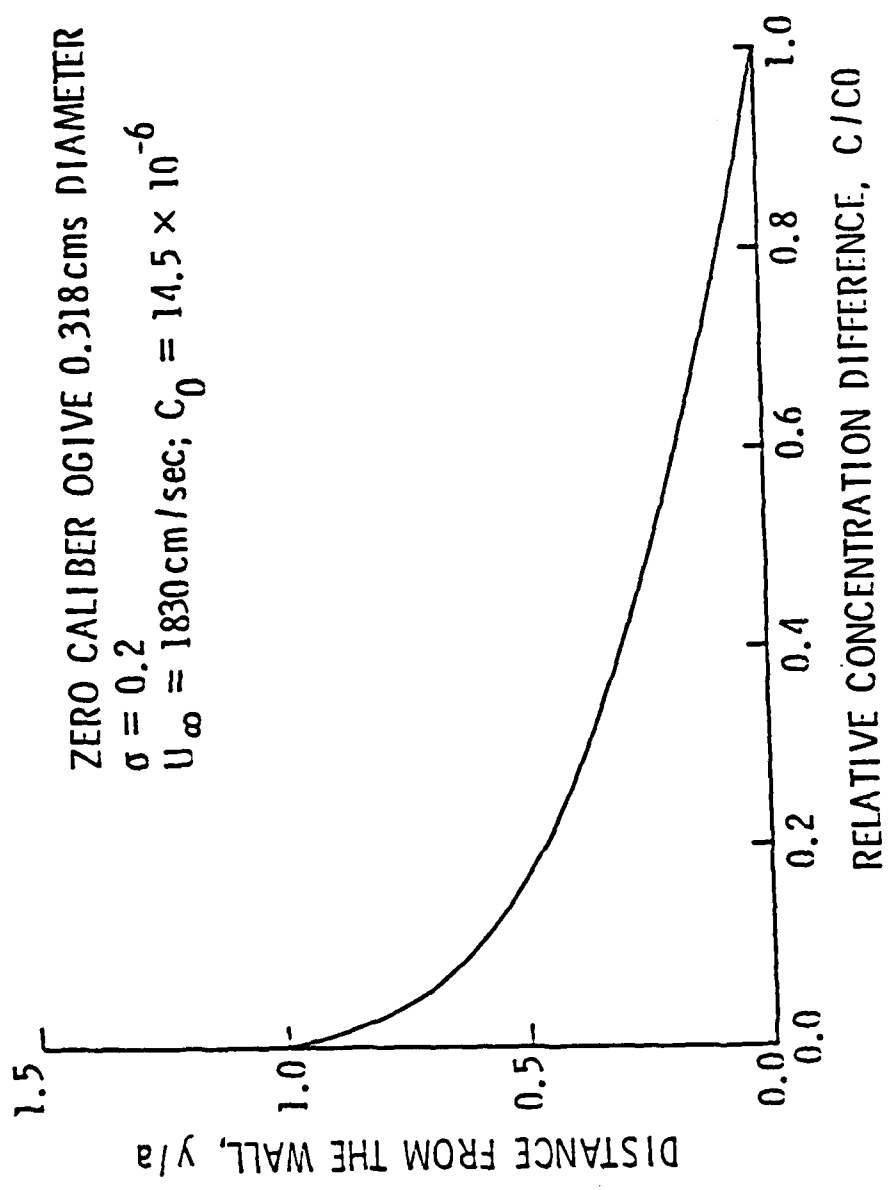


Figure 2.4. Concentration Layer Profile over a Two-Dimensional Cavity.

#### 2.4 Mathematical Analysis

The discrepancy that exists between the experimental results and existing mathematical models for gaseous diffusion across axisymmetric cavities prompted us to look at the validity of extending existing two-dimensional diffusion models to axisymmetric diffusion studies. While it is true that two-dimensional solutions can be extended to include axisymmetric cases, such extensions hold good only when the concentration boundary layer thickness on the cavity is small compared to the radius of cavity. This is a rather serious restriction for flows normally encountered where the concentration layer thickness is not necessarily small, relative to the radius of the cavity. Just to exemplify this point, the concentration layer profile at the end of the cavity has been plotted in Figure 2.4, the flow conditions being representative of experiments reported in Ref. (13). It is clear that the concentration layer thickness is comparable to the radius of cavity. Thus, a more accurate mathematical representation for gaseous diffusion across an axisymmetric cavity surface is clearly warranted.

Gaseous diffusion will occur when there is a dissolved gas concentration gradient between the free stream and the liquid on the cavity surface. If  $a_1$  is the measured dissolved gas content in parts per million (ppm) by moles, then by Henry's law, the saturation partial pressure of the gas in the free stream is given by

$$P_{FS} = a_1 \beta \quad (2.8)$$

where  $\beta$  is the Henry's law constant which depends on temperature. If  $p_G$  is the partial pressure of non-condensable gas in the cavity, then the mean concentration difference expressed in ppm by moles is

$$c = a_1 - \frac{p_G}{\beta} . \quad (2.9)$$

Consider an axisymmetric flow of water containing dissolved gases which has the concentration  $C(X, R)$  at any point in the region  $R > a$ , where "a" is the radius of the axisymmetric cavity. The undisturbed flow is taken to have a constant velocity  $U_\infty$  in the positive X-direction. In the interest of simplicity, all momentum boundary layer perturbation velocities  $u$  and  $v$  in the X and R directions respectively are neglected. The free stream velocity applies to the entire flow field. The mass diffusion of gases through the permeable axisymmetric cavity surface occurs between  $X = 0$  and  $X = L$  as shown in Figure 2.5. The remaining portion of the X-axis is supposed to be impermeable to gas diffusion. On the permeable surface, let the concentration have the constant value  $C_0$  and the concentration of dissolved gases at points far from the permeable surface have the value  $C_\infty$ . Then, the concentration difference  $c(X, R)$  is defined as

$$c(X, R) = C(X, R) - C_\infty . \quad (2.10)$$

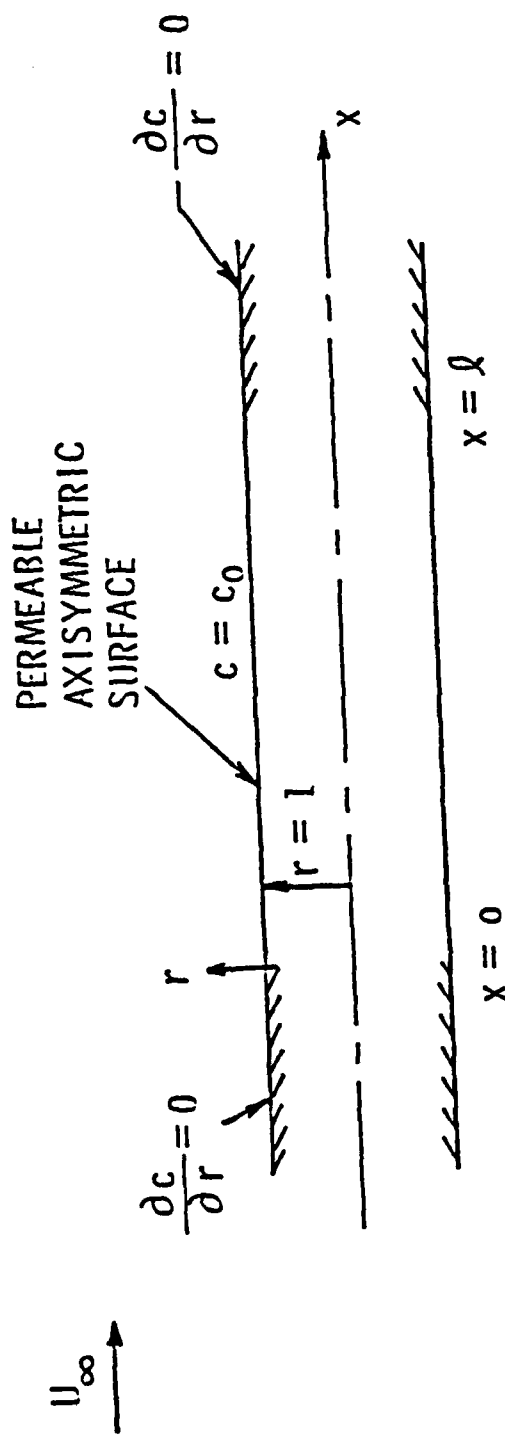


Figure 2.5. Idealized Cavity Geometry and Boundary Conditions.

Let  $\kappa$  be the mass diffusivity parameter. We do not identify the nature of the mass diffusivity parameter as either molecular or turbulent. In either case, the governing differential equation for the concentration difference has the form [see, for example, Carslaw and Jaeger (22)]

$$U_{\infty} \frac{\partial c}{\partial x} = \kappa \nabla^2 c , \quad (2.11)$$

where  $\nabla^2$  is the Laplacian operator. By non-dimensionalizing the linear distances along X, Y, Z and R by the radius of the cavity such that  $x = X/a$ ,  $y = Y/a$ ,  $z = Z/a$  and  $r = R/a$ , we can write Eq. (2.11) as

$$\frac{\partial c}{\partial x} = \frac{\kappa}{a U_{\infty}} \nabla^2 c . \quad (2.12)$$

In order to determine the solution of Eq. (2.12) subject to the prescribed boundary conditions, we first write the solution of Eq. (2.12) when a source of strength "q" is located at the origin in a moving fluid (22), as

$$c(x, y, z) = \frac{q}{4\pi k r' a} e^{-\lambda(r' - x)} , \quad (2.13)$$

where

$q$  = mass flux of gas

$k$  = mass conductivity =  $\kappa \rho$

$r' = \sqrt{x^2 + y^2 + z^2}$  , the distance between the field point and the origin

$\kappa$  = mass diffusivity

$\rho$  = density of the liquid

$\lambda = U_{\infty}/2\kappa$  , a dimensionless parameter.

If the source is located at  $(\xi, \eta, \zeta)$  instead of at the origin, the solution of Eq. (2.12) will be modified as follows:

$$c(x, y, z; \xi, \eta, \zeta) = \frac{q}{4\pi kr'' a} e^{-\lambda(r'' - x)} , \quad (2.14)$$

where  $r'' = \sqrt{(x - \xi)^2 + (y - \eta)^2 + (z - \zeta)^2}$ , is the distance between the source point  $(\xi, \eta, \zeta)$  and the field point  $(x, y, z)$ .

We now consider a "ring source" of unit radius and unit strength located at  $x = \xi$ . The plane of the ring is perpendicular to the  $x$ -axis and the  $x$ -axis passes through the center of the ring. Consider an element of the ring  $d\theta$ , as shown in Figure 2.6. Then the strength of this element will be  $d\theta/2\pi$  and from Eq. (2.14), the concentration at a point  $(x, r)$  due to the flux of concentration at  $(\xi, 1, \theta)$  will be

$$\delta c(x, r; \xi, 1, \theta) = \frac{d\theta}{8\pi^2 kr'' a} e^{-\lambda(r'' - (x - \xi))} . \quad (2.15)$$

Integrating the right-hand side of the above equation between the limits of 0 and  $2\pi$ , we obtain the concentration at a field point  $(x, r)$  due to a unit ring source at  $x = \xi$  as

$$c(x, r; \xi) = \frac{e^{\lambda(x - \xi)}}{8\pi^2 ka} \int_0^{2\pi} \frac{e^{-\lambda r''}}{r''} d\theta , \quad (2.16)$$

where the distance  $r''$  is now given by

$$r'' = \sqrt{(x - \xi)^2 + r^2 + 1 - 2r \cos \theta} . \quad (2.17)$$

The integral in Eq. (2.16) has been evaluated in Appendix A.1 for large values of  $\lambda$  (of the order 2000) by using Laplace's method and the result for the concentration is

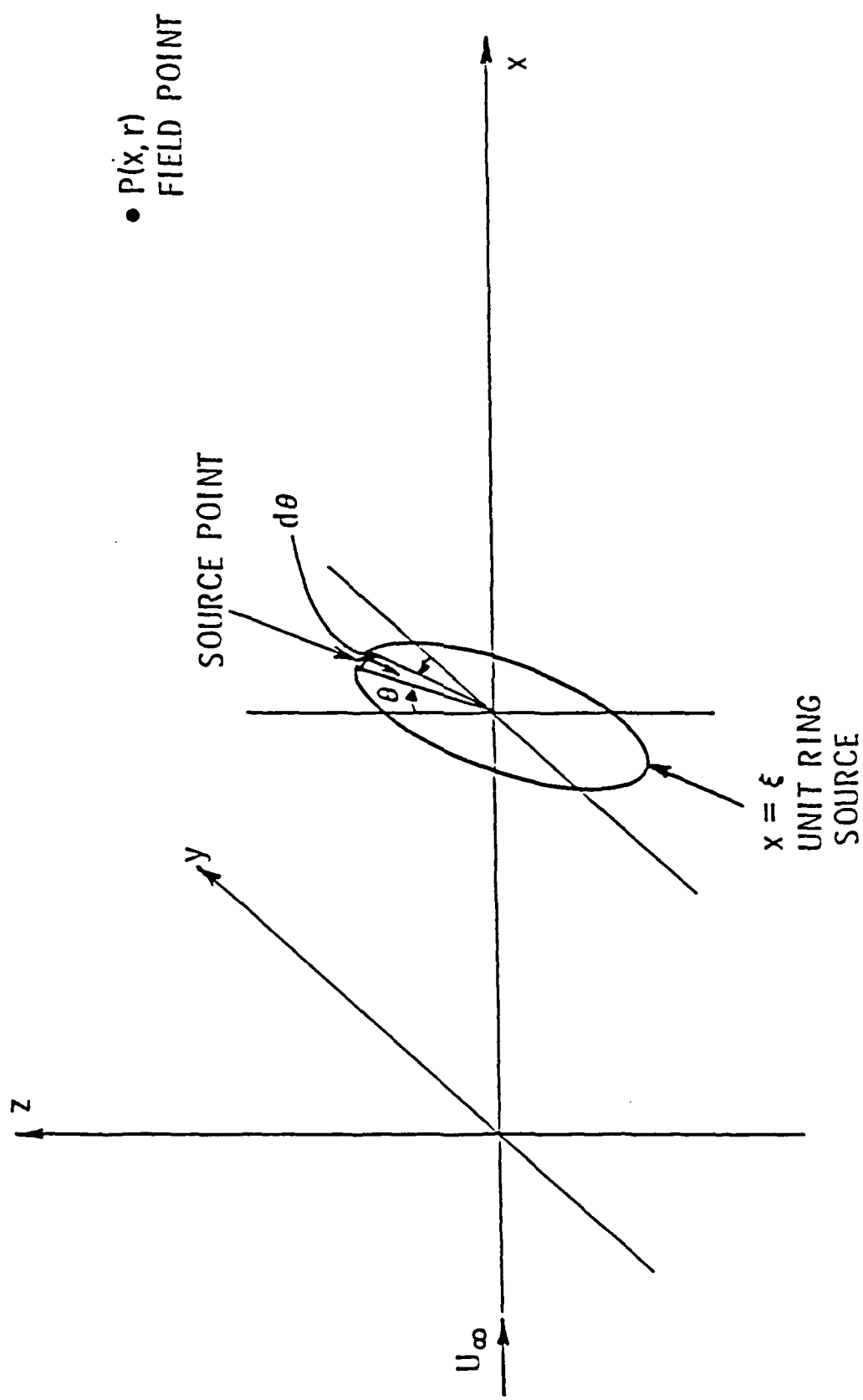


Figure 2.6. Ring Source Geometry.

$$c(x, r; \xi) = \frac{e^{\lambda(x-\xi)}}{8\pi^{3/2} \rho a^{3/2} \sqrt{\kappa U_\infty}} \frac{e^{-\lambda} \sqrt{(x-\xi)^2 + (r-1)^2}}{[(x-\xi)^2 + (r-1)^2]^{1/4}} . \quad (2.18)$$

Equation (2.18) has the desired properties relevant to the physical problem, viz.,  $c \rightarrow 0$  as  $x \rightarrow -\infty$  and  $c \rightarrow 0$  as  $r \rightarrow \infty$ .

Now suppose that the mass flux per unit length between  $x = -\infty$  and  $x = +\infty$  is given by the function  $f(x)$ . Then the function  $c(x, r)$  can be expressed in terms of this source strength per unit length as

$$c(x, r) = \frac{A}{\sqrt{r}} \int_{-\infty}^{\infty} f(\xi) e^{\lambda(x-\xi)} \left[ \frac{e^{-\lambda} \sqrt{(x-\xi)^2 + (r-1)^2}}{[(x-\xi)^2 + (r-1)^2]^{1/4}} \right] d\xi , \quad (2.19)$$

where

$$A = \frac{1}{8\pi^{3/2} \rho a^{3/2} \sqrt{\kappa U_\infty}} . \quad (2.20)$$

In the integral in Eq. (2.19), the limit  $-\infty$  to  $+\infty$  appears instead of 0 to  $\ell$  because the unit ring source solution does not satisfy the boundary condition at  $r = 1$ :  $dc/dr|_{x \neq \xi} = 0$ . If we now require that  $c(x, 1) = c_0 = C_0 - C_\infty$ , in the interval  $0 < x < \ell$ , and  $dc/dr|_{r=1} = 0$  in the intervals  $-\infty < x < 0$  and  $\ell < x < \infty$ , the source strength  $f(x)$  is determined by the three integral equations of the form

$$\begin{aligned} \frac{c_0}{A} = & \int_{-\infty}^0 \frac{f_1(\xi)}{\sqrt{x_2 - \xi}} d\xi + \int_0^{x_2} \frac{f_2(\xi)}{\sqrt{x_2 - \xi}} d\xi + \int_{x_2}^{\ell} \frac{f_2(\xi) e^{-2\lambda(\xi - x_2)}}{\sqrt{\xi - x_2}} d\xi \\ & + \int_{\ell}^{\infty} \frac{f_3(\xi) e^{-2\lambda(\xi - x_2)}}{\sqrt{\xi - x_2}} d\xi , \end{aligned} \quad (2.21)$$

$$0 = \int_{-\infty}^{x_1} \frac{f_1(\xi)}{\sqrt{x_1 - \xi}} d\xi + \int_{x_1}^0 \frac{f_1(\xi)e^{-2\lambda(\xi - x_1)}}{\sqrt{\xi - x_1}} d\xi + \int_0^l \frac{f_2(\xi)e^{-2\lambda(\xi - x_1)}}{\sqrt{\xi - x_1}} d\xi \\ + \int_l^{\infty} \frac{f_3(\xi)e^{-2\lambda(\xi - x_1)}}{\sqrt{\xi - x_1}} d\xi , \quad (2.22)$$

and

$$0 = \int_{-\infty}^0 \frac{f_1(\xi)}{\sqrt{x_3 - \xi}} d\xi + \int_0^l \frac{f_2(\xi)}{\sqrt{x_3 - \xi}} d\xi + \int_l^{x_3} \frac{f_3(\xi)}{\sqrt{x_3 - \xi}} d\xi \\ + \int_{x_3}^{\infty} \frac{f_3(\xi)e^{-2\lambda(\xi - x_3)}}{\sqrt{\xi - x_3}} d\xi , \quad (2.23)$$

where the positive branch of the square root has been taken. The functions  $f_1$ ,  $f_2$  and  $f_3$  are the source strength distributions in the intervals  $-\infty < x_1 < 0$ ,  $0 < x_2 < l$  and  $l < x_3 < \infty$  respectively. These three source functions are taken to be zero outside their specified intervals.

The three integral equations (2.21) to (2.23) are coupled and rather difficult to solve in their present form. In order to make the solution tractable, we simplify some of the integrals appearing in the three equations (see Appendix A.2) recognizing the fact that the nondimensional number  $\lambda$  is fairly large. Thus, the simplified integral equations are

$$\frac{c_0}{A} = \int_{-\infty}^0 \frac{f_1(\xi)}{\sqrt{x_2 - \xi}} d\xi + \int_0^{x_2} \frac{f_2(\xi)}{\sqrt{x_2 - \xi}} d\xi + \frac{\pi}{2\lambda} f_2(x_2) , \quad (2.21a)$$

$$\int_{-\infty}^{x_1} \frac{f_1(\xi)}{\sqrt{x_1 - \xi}} d\xi + \frac{\pi}{2\lambda} f_1(x_1) = 0 , \quad (2.22a)$$

$$\int_{-\infty}^0 \frac{f_1(\xi)}{\sqrt{x_3 - \xi}} d\xi + \int_0^{x_3} \frac{f_2(\xi)}{\sqrt{x_3 - \xi}} d\xi + \int_0^{x_3} \frac{f_3(\xi)}{\sqrt{x_3 - \xi}} d\xi + f_3(x_3) - \frac{\pi}{2\lambda} = 0 . \quad (2.23a)$$

The integral equation (2.22a) has been solved using Picard's method\* in Appendix A3 and the result for  $f_1$  is

$$f_1(x_1) = c_1 e^{2\lambda x_1} \quad x_1 < 0 , \quad (2.24)$$

and  $c_1$  is an arbitrary constant. The function  $f_1(x_1)$  may now be substituted in the integral equation (2.21a) and the function  $f_2(x_2)$  obtained by the Laplace transform method (see Appendix A.4) as

$$f_2(x_2) = \left( \frac{c_0}{A} - \frac{2\lambda}{\pi} + c_1 \right) e^{2\lambda x_2} \operatorname{erfc} \sqrt{2\lambda x_2} - \frac{c_1}{\sqrt{2\lambda \pi x_2}} , \quad (2.25)$$

where the parameter  $\lambda$  has been defined as part of Eq. (2.13), the quantity  $A$  is given by Eq. (2.20) and

\*See, for example, Hildebrand, Methods in Applied Mathematics, Prentice Hall Inc. N. Y. 1952.

where  $\text{erfc}(t)$  denotes the complimentary error function

$$\text{erfc}(t) = \frac{2}{\sqrt{\pi}} \int_t^{\infty} e^{-x^2} dx . \quad (2.26)$$

Having found  $f_1(x_1)$  and  $f_2(x_2)$ , one can find the function  $f_3(x_3)$  from Eq. (2.23a). We have not given this last solution here even though the way to find it seems clear. The reason is that  $f_2(x_2)$  controls the diffusion into the cavity and  $f_3$  is not required to determine  $f_2$ . We note also that the source strength is strongest near the cavity separation point so most of the mass flux will occur at the start of the cavity and not near the downstream end.

The rate at which mass is diffused along the entire length of the axisymmetric cavity is

$$\dot{m} = \frac{dM}{dt} = \int_0^l f_2(x_2) dx_2 , \quad (2.27)$$

$$\dot{m} = \left( \frac{c_0}{A} \sqrt{\frac{2\lambda l}{\pi}} + c_1 \right) \left[ \frac{e^{2\lambda l} \text{erfc} \sqrt{2\lambda l}}{2\lambda} + \sqrt{\frac{2l}{\pi\lambda}} - \frac{1}{2\lambda} \right] - c_1 \sqrt{\frac{2l}{\pi\lambda}} . \quad (2.28)$$

Equation (2.28) may be rewritten as

$$\dot{m} = 8\pi\rho a^2 U_\infty c_0 \left[ \frac{e^{2\lambda l} \text{erfc} \sqrt{2\lambda l}}{2\lambda} + \sqrt{\frac{2l}{\pi\lambda}} - \frac{1}{2\lambda} \right] + c_1 \left[ \frac{e^{2\lambda l} \text{erfc} \sqrt{2\lambda l}}{2\lambda} \right] . \quad (2.28a)$$

We note here the fact the first term in Eq. (2.28a) represents the two-dimensional wrap around solution. For large values of  $\lambda l$ , one can write

$$e^{2\lambda\ell} \operatorname{erfc}\sqrt{2\lambda\ell} \sim \frac{1}{\sqrt{\pi}} \left[ \frac{1}{\sqrt{2\lambda\ell}} - \frac{1}{2(2\lambda\ell)^{3/2}} + \dots \right] , \quad (2.29)$$

in which case,

$$\begin{aligned} \dot{m} &= 16\sqrt{\pi} kc_0 a \left[ \sqrt{2\lambda\ell} - \sqrt{\frac{\pi}{2}} + \frac{1}{2\sqrt{2\lambda\ell}} - \frac{1}{4(2\lambda\ell)^{3/2}} + \dots \right] \\ &+ \frac{c_1}{\lambda\sqrt{\pi}} \left[ \frac{1}{2\sqrt{2\lambda\ell}} - \sqrt{\frac{\pi}{2}} - \frac{1}{4(2\lambda\ell)^{3/2}} + \dots \right] . \end{aligned} \quad (2.30)$$

If we assume that the constant  $c_1$  has the same order of magnitude as  $8\pi pa^2 U_\infty c_0$ , we can conclude from Eq. (2.30) that the expression for mass flow rate across an axisymmetric cavity is the same as the two-dimensional wrap around solution. This conclusion, of course, is based on the simplifications we have effected in the three coupled integral equations (2.21), (2.22) and (2.23). These same approximations were employed by Parkin in his theory. Nonetheless, the good correlations observed between Billet-Weir experimental results and modified Parkin's model (see Figures 2.2 and 2.3) support the conclusions that we draw from the axisymmetric cavity diffusion analysis. The reason for this being that most of the diffusion takes place across the upstream parts of the cavity where the diffusion layer is still thin and wrap-around is still useful.

## 2.5 Recapitulation

We have explored some of the aspects of gaseous diffusion into axisymmetric cavities. A modified Parkin model may be better suited for the prediction of gaseous diffusion across cavities that emerge from the leading edge than Brennen's model. We have demonstrated through an axisymmetric gaseous diffusion analysis that (within the assumptions and approximations) two-dimensional gaseous diffusion solutions can be extended to the axisymmetric cavity with the result that the turbulent mixing length diffusivity of Launder and Spalding will be useful for the determination of diffusive mass flow into the two-dimensional flows studied below.

## CHAPTER 3

## EXPERIMENTAL INVESTIGATION OF THE BEHAVIOR OF NONSTEADY

## CAVITIES BEHIND A WEDGE OSCILLATING IN PITCH

3.1 Introduction

An unsteady cavity flow about a solid body in a pure liquid may be represented mathematically with the help of cavity flow theory and it can also be understood physically. The presence of dissolved gases in the liquid makes the same phenomenon difficult to understand. A cavity in a pure liquid is filled only with the liquid vapor. So the volume of an unsteady cavity filled only with vapor grows and collapses in volume according to the motion of the body or according to the imposed pressure field. In the absence of other flow disturbances, the vapor is absorbed and released almost instantaneously because the time scale of the process of vapor release and absorption is extremely small compared to the time scale of cavity motion and hence cavity vapor pressure fluctuations are not seen. In such a case, the pressure inside the cavity equals that of vapor pressure of the ambient liquid at the equilibrium temperature at all times, provided the temperature is not too near the critical temperature.

This situation, however, does not occur in the laboratory or in practice. There are always certain amounts of free and dissolved gases present in the liquid. On a cavitating body, these gases diffuse across the cavity surface and are entrained by the turbulent flow at the trailing edge of the cavity. This diffusion-entrainment process is thought to influence cavity volume fluctuations and associated cavity pressure fluctuations in an unsteady cavity.

Several investigations have been devoted in the past to the analysis of steady gaseous diffusion across the cavity surface. Parkin and Kermeen (8) studied the molecular gaseous diffusion into a microbubble, whereas Brennen (9) considered gaseous diffusion from a turbulent flow into a large cavity. Very few unsteady cavity flow studies (both analytical and experimental) have been done in the past in which cavity pressure fluctuations are considered, largely due to the complexities involved in such studies. Although Leehey and Jiang (16) measured the unsteady cavity pressures behind a three-dimensional elliptical foil oscillating in pitch, there appears to be no experimental study available aimed at a better understanding of the behavior of unsteady cavities, particularly (a) the cavity pressure fluctuations and their dependence on the frequency of oscillations of the body; (b) the source-like nature of the unsteady cavity; and (c) the cavity length fluctuation as a function of frequency. The present experimental study is aimed at understanding these aspects of unsteady two-dimensional cavities.

### 3.2 Experimental Apparatus

#### 3.2.1 Six-Inch Water Tunnel

The experiment was conducted in the 6-inch recirculating variable pressure water tunnel at ARL/PSU (21). In this tunnel, the test section velocity was variable between 0 and 50 feet per second and the static pressure was variable continuously between 0.5 psia and 50 psia. The velocity was indicated on a digital voltmeter which read the pressure drop between the settling chamber and the

test section. The test section static pressure was read by a Heise type Bourdon-tube pressure gage. The test section was 24 inches long and was made of lucite to enable visual observations and video recordings to be made of the unsteady cavity flow phenomena.

### 3.2.2 Model and Shaft

The foil used in this test was a wedge of rectangular planform measuring two inches wide and four inches long and was made of stainless steel. A small slot was made on the cavitating surface of the foil to mount a pressure transducer that would measure the unsteady cavity pressures. A small hole was made in the shaft running axially to the middle of the foil to lead the pressure transducer wires and also a static cavity pressure tap out of the tunnel. The support shaft was made of stainless steel and the middle portion of the shaft formed the trailing section of the wedge foil. The foil and shaft were fastened together by a pair of dowel pins and set screws. Two views of the foil-shaft assembly mounted in the test section along with the hydraulic drive are shown in Figure 3.1.

### 3.2.3 Drive System

The drive system used was essentially a modified control surface actuator. It consisted of two plungers actuated by a hydraulic servo. The plungers were connected to the pitch drive plate fastened to the shaft by means of a wire rope. When the servo was actuated by an amplified sine wave signal, the shaft executed nearly sinusoidal motion in pitch. Because of the slider crank mechanism, though the

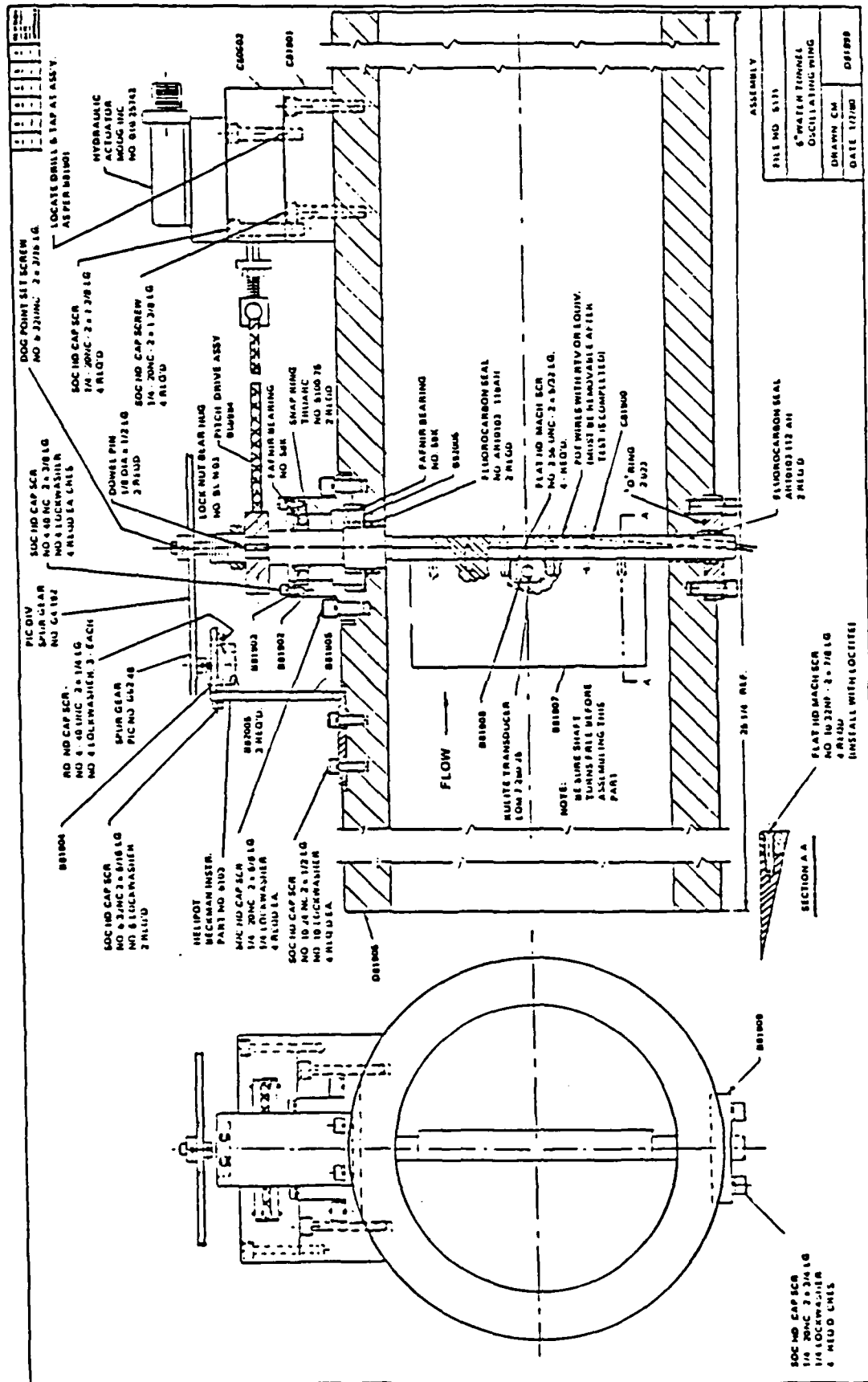


Figure 3.1. Full Shaft Assembly.

motion of the plunger was sinusoidal, the motion of the shaft was not. However, an analysis of the error signals from the feed back unit showed higher harmonics whose amplitudes were at least 40 dB lower than the fundamental frequency of oscillation. The angle of attack of the foil was varied by changing the d.c. offset to the hydraulic servo. The frequency response of the pitch drive assembly which is flat up to about 10 Hertz is shown in Figure 3.2. The static angle of attack of the foil was variable continuously from zero to twenty degrees. The dynamic angle of attack amplitude was variable continuously from zero to fifteen degrees peak to peak. Using this setup, the static angle of attack could be adjusted to an accuracy of 0.02 degrees and the amplitude of foil oscillation could be adjusted to an accuracy of  $\pm 0.05$  degrees. Figure 3.3 shows a typical cavity behind the wedge foil.

#### 3.2.4 Instrumentation

Unsteady cavity pressure was measured by mounting a crystal transducer flush with the cavitating surface of the foil. This Barium Titanate crystal transducer was calibrated in a slosh tube (22) with a LC-10 hydrophone as the reference. The frequency response of the crystal transducer mounted on the foil is shown in Figure 3.4. The static pressure in the cavity was measured by a pressure tap leading to the cavity from a Validyne diaphragm type pressure transducer. The unsteady pressures upstream and downstream of the foil were also measured with a Validyne pressure transducer. This transducer was suspended from an independent support to eliminate possible effects of tunnel vibration on the pressure transducer output.

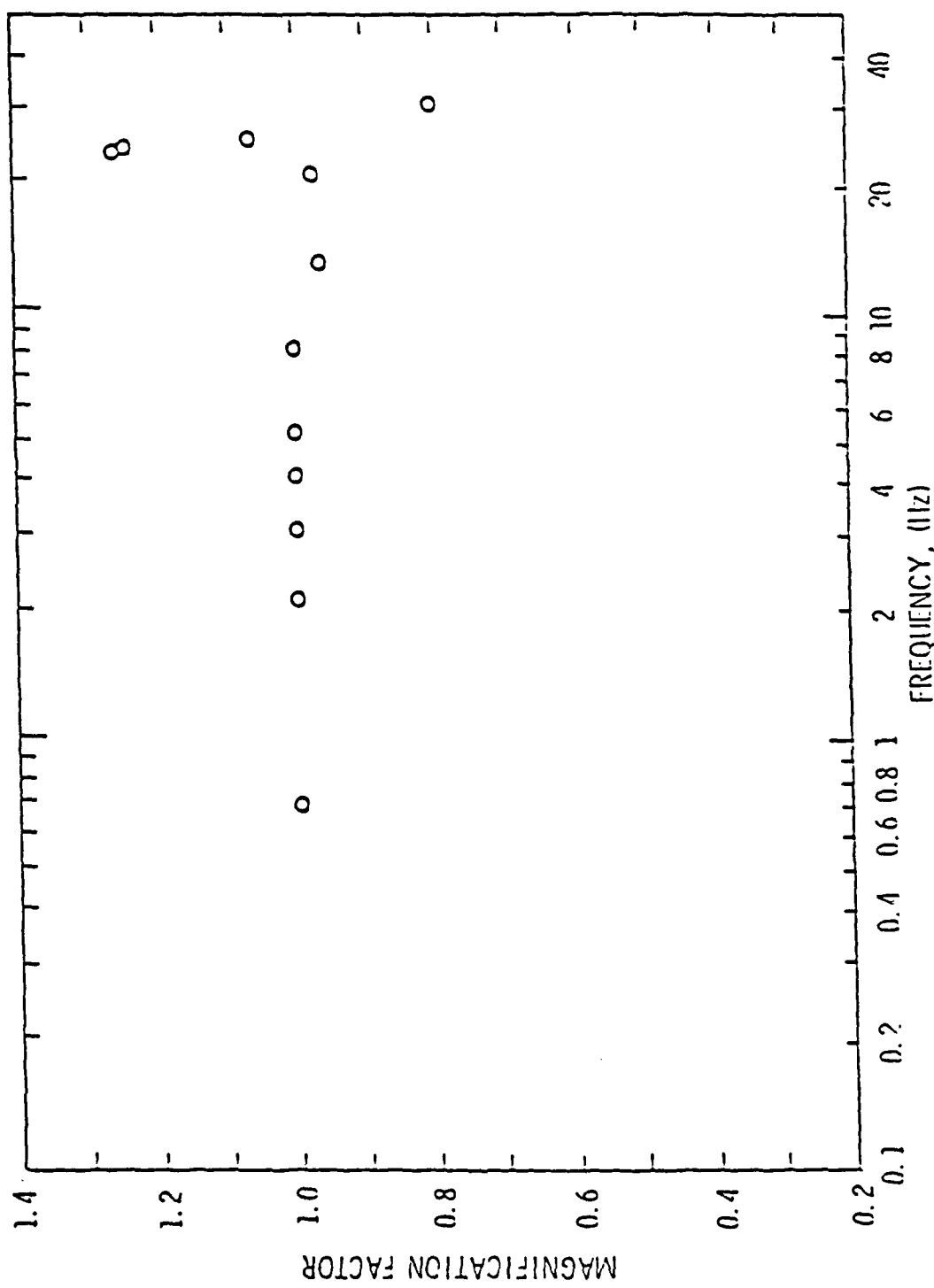


Figure 3.2. Frequency Response of Pitch Drive Assembly.

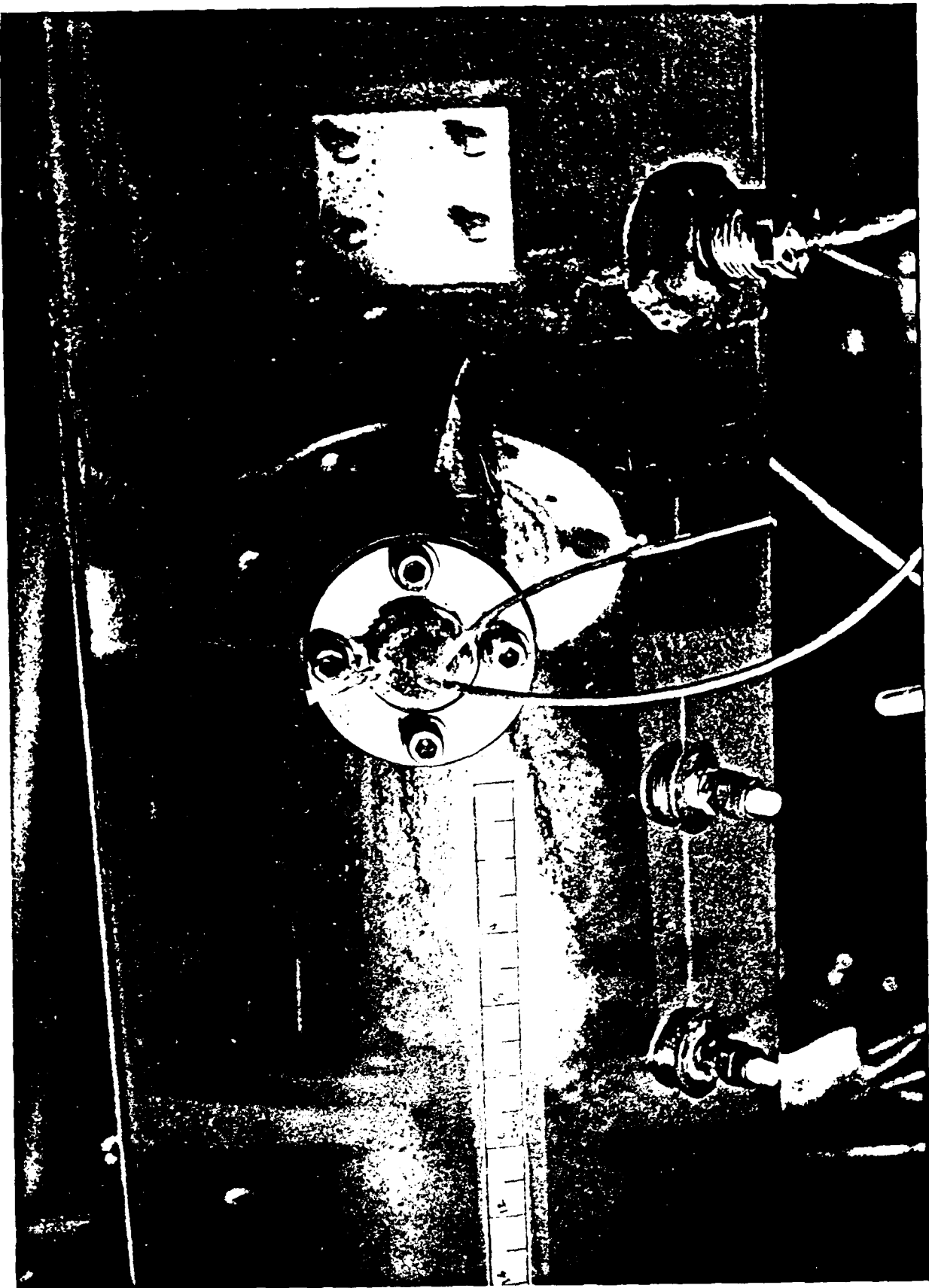


Figure 3.3. Typical Cavity behind Wedge Foil.

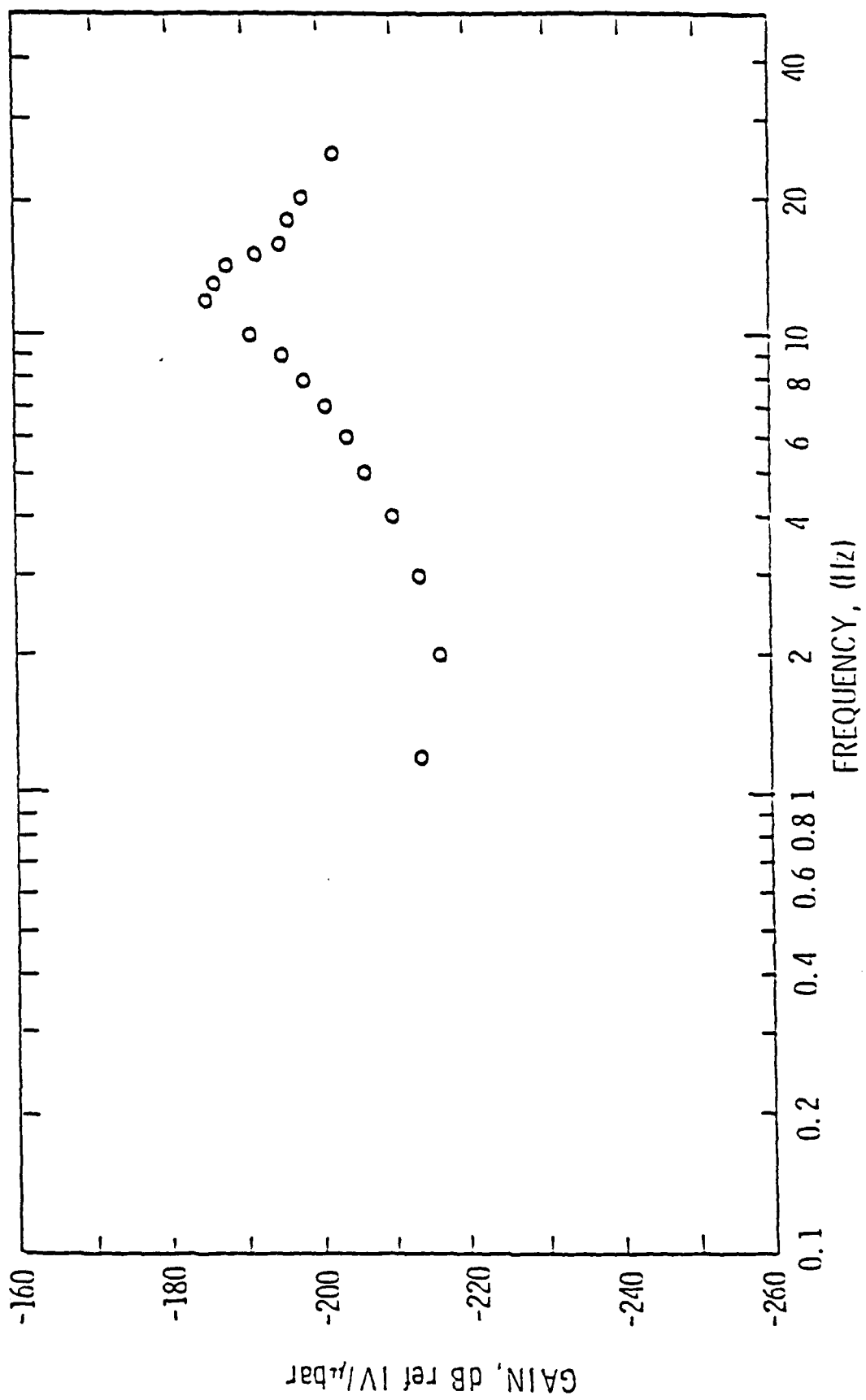


Figure 3.4. Frequency Response of Crystal Transducer.

The amount of free air in the tunnel water was determined by measuring the speed of sound in the upstream part of the test section. This was achieved by transmitting a gated high frequency pulse (about 120 kHz) through a LC-10 hydrophone and receiving it diametrically across the test section by a crystal transducer (Barium Titanate crystal) as shown in Figure 3.5. The distance between the two transducers for the sound speed measurement was 7.443 inches. By measuring the time delay between the transmitted and received pulse on a high speed oscilloscope (Tektronix 7633), the speed of sound was determined. The accuracy of speed measurement is within  $\pm 30$  ft/sec. An example of the sound speed calculation and the estimation of free air in the tunnel water is given in Appendix B.2. The dissolved air in the tunnel water was measured by the conventional Van Slyke Apparatus. During the course of the experiment, the dissolved air content ranged between 7 ppm by moles while the free air ranged from 3 ppm (speed of sound = 4490 ft/sec) to 10 ppm by volume (speed of sound = 3730 ft/sec). The measurement of free gas and dissolved gas in the tunnel ensured that there was enough gas supply in the tunnel water to maintain dissolved gas diffusion and entrainment at all times.

All the unsteady pressure data were analyzed through a real time spectral analyzer (Spectral Dynamics SD-300 and SD-360). The cavity motions were recorded on a video recorder using a video camera.

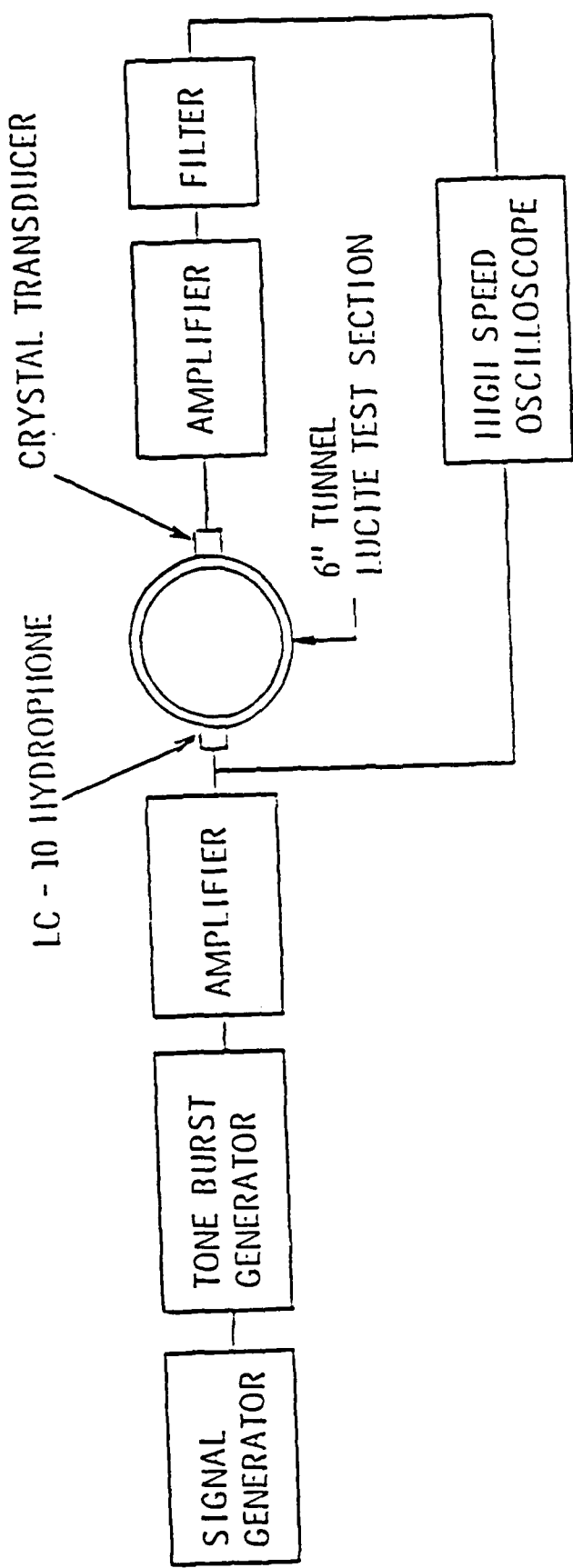


Figure 3.5. Schematic of Apparatus for Sound Speed Measurement.

### 3.3 Test Procedure

The range of test parameters considered for the experiments were: (a) tunnel pressure: 1 psia -10 psia; (b) tunnel velocity: 10 ft/sec -45 ft/sec; and (c) foil oscillation frequency: 0.2 Hz -30 Hz. Three distinct phases of investigations were undertaken as described below.

#### 3.3.1 Video Recording of Cavity Motion

The unsteady motions of the cavity were recorded on a video tape using a video camera for several frequencies of foil oscillation for sufficiently long periods to record many complete motion cycles at each frequency. The plan view of the cavity was recorded and it demonstrated that the flow was nearly two dimensional. A strobe was used to obtain time history of cavity motion. Care was taken to set the frequency of the strobe at a value that was different from the foil oscillation frequency so that the variations of cavity length with time could be determined. In this way, the variation of cavity length for one complete cycle of oscillation could be determined by measuring the length at a number of points in the phase of the oscillation as explained below.

#### 3.3.2 Source-Like Nature of the Oscillating Cavity

These tests were performed by measuring the unsteady pressures at three field points at the tunnel wall: 32.5 inches upstream and downstream from the axis of oscillation and 16.25 inches upstream from the axis of oscillation. These field points were chosen such that any "potential flow" pressures at these wall points due to an

oscillating cavity being present in the cylindrical test section were negligible and the results can be thought of as far-field free stream fluctuations. A computer code, developed by Fernandez (23), was used to find an upper bound for this effect assuming the shape of the cavity to be an ellipse. Figure 3.6 shows the variation of pressure coefficient along the length of the tunnel for the extreme condition when a body in the shape of an ellipse of semi-major axis measuring 3 inches and semi-minor axis measuring 1.5 inches is kept in the test section. At each field point, unsteady pressures were measured for several tunnel velocities keeping the cavitation number constant.

### 3.3.3 Measurement of Cavity Pressures

Steady and unsteady cavity pressures were measured for several foil frequencies, cavitation numbers and static angles of attack. The steady pressure was measured from the pressure tap leading into the cavity. This pressure tap was connected to the pressure transducer through a valve venting the line to the atmosphere in the laboratory. By closing the valve only after the formation of the cavity, the presence of water bubbles in the pressure tap line was completely eliminated. Unsteady pressure data were analyzed through a real time analyzer.

### 3.4 Test Results and Discussion

Sample data from the experiments are tabulated in Appendix B.1. (A complete tabulation of the experimental data is available upon request from the author.) The cavitation number was calculated based on the measured steady cavity pressure. The maximum error

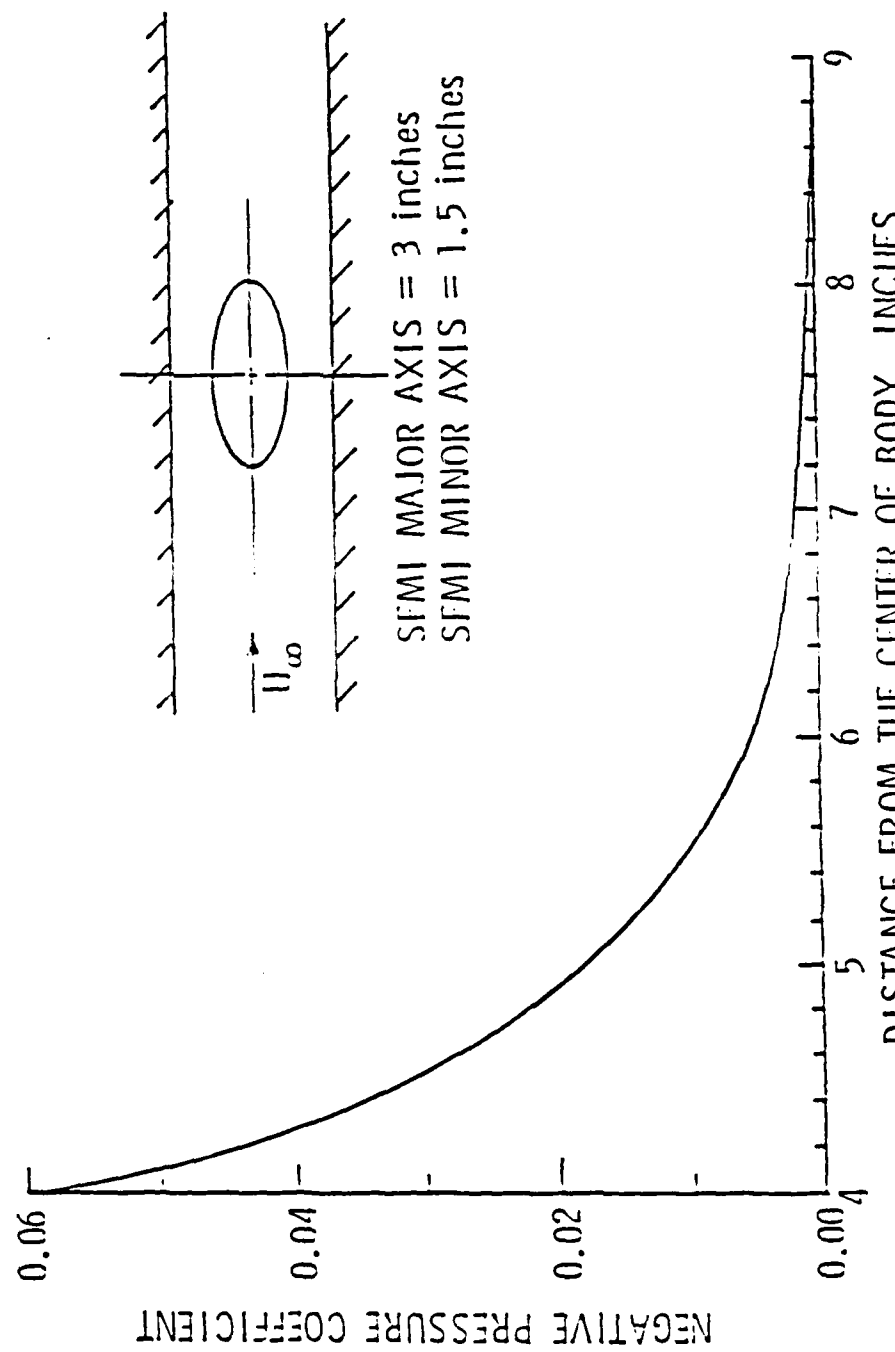


Figure 3.6. Variation of Pressure along the length of the Tunnel due to an Elliptical cavity.

in calculating the cavitation number is estimated to be 4.8% (see Appendix B.3). The region of the cavity where the cavity pressure was measured was nearly two-dimensional. Hence a wall effect correction appropriate to such flows developed by Hsu (24) was used to correct the measured cavitation number. An example of this correction procedure is contained in Appendix B.4.

### 3.4.1 Cavity Length History

At low frequencies of foil oscillation (0.2 Hz - 3.0 Hz) it was noticed visually that the cavity behind the foil seemed to follow the motion of the foil without any noticeable phase difference between input foil motion and the resulting cavity length change. However, as the driving frequency was increased beyond 5 Hz, the phase lag of the cavity motion was noticeable. Beyond about 20 Hz, there was very little, if any, motion of the cavity due to the oscillation of the foil. It was clear from these visual observations that the cavity has the appearance of an inertial effect.

The cavity length history was obtained by playing back the video tape manually on a large television screen and measuring the cavity lengths at equal time intervals, the time interval being governed by the frequency of the strobe. The magnification of the cavity on the television screen was properly accounted for in obtaining true cavity lengths. The cavity length measurement on the screen was at times hampered by the "not so clear" terminal end of the cavity. However, all the measurements were consistently made and the cavity lengths were measured within an accuracy of three millimeters.

The time histories of cavity motions for a cavitation number of 0.47 at four different foil frequencies are shown in Figures 3.7(a) through 3.7(d). It is apparent from these figures that the motion of the cavity is far from being sinusoidal. The Fourier components of these time histories are shown in Figures 3.8(a) through 3.8(d), respectively. It is observed from these results that the cavity motion consists of frequencies other than the fundamental driving frequency and in particular the first overtone is significant in all the cases. An observation of the spectra at different foil oscillation frequencies shows that at 0.5 Hz, the motion of the cavity is close to harmonic motion whereas at 1 Hz the great increase in the first overtone of the unsteady cavity is apparent. As the frequency is increased, the cavity motion is again close to harmonic motion as evidenced from the spectra in Figures 3.8(c) and 3.8(d). It is of interest to compare qualitatively these amplitudes of harmonics of cavity motion with the linearized unsteady cavity theory. If we denote  $\ell(t)$  as the cavity length at an instant, we may write (see Chapter 5)

$$\ell(t) = \sqrt{\frac{2\alpha(t)}{\sigma}} , \quad (3.1)$$

where  $\alpha(t)$  is the angle of attack and  $\sigma$  is the cavitation number.

For the oscillating foil motion, we may write

$$\alpha(t) = \alpha_0(1 + \epsilon e^{j\omega t}) , \quad (3.2)$$

where  $\epsilon\alpha_0$  denotes the amplitude of pitching motion. Recognizing the fact that  $\epsilon$  is a small number, we can write for  $\ell(t)$ ,

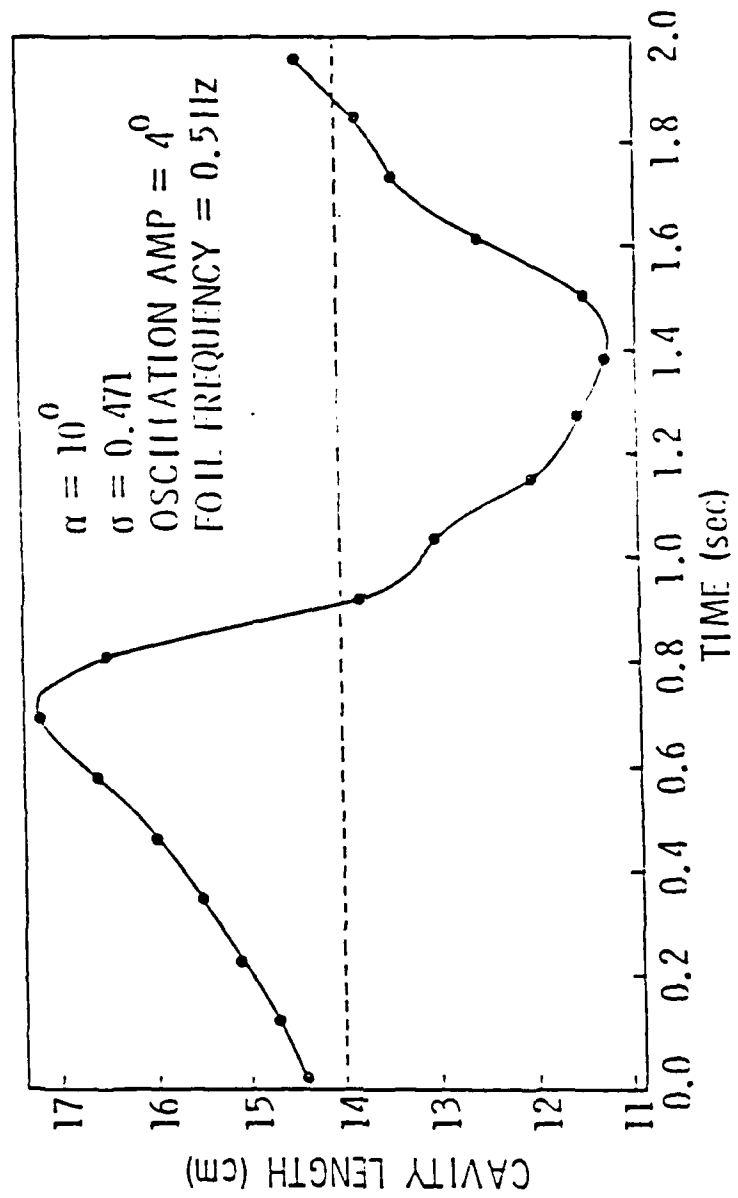


Figure 3.7(a). Time History of Cavity Length, 0.5 Hz.

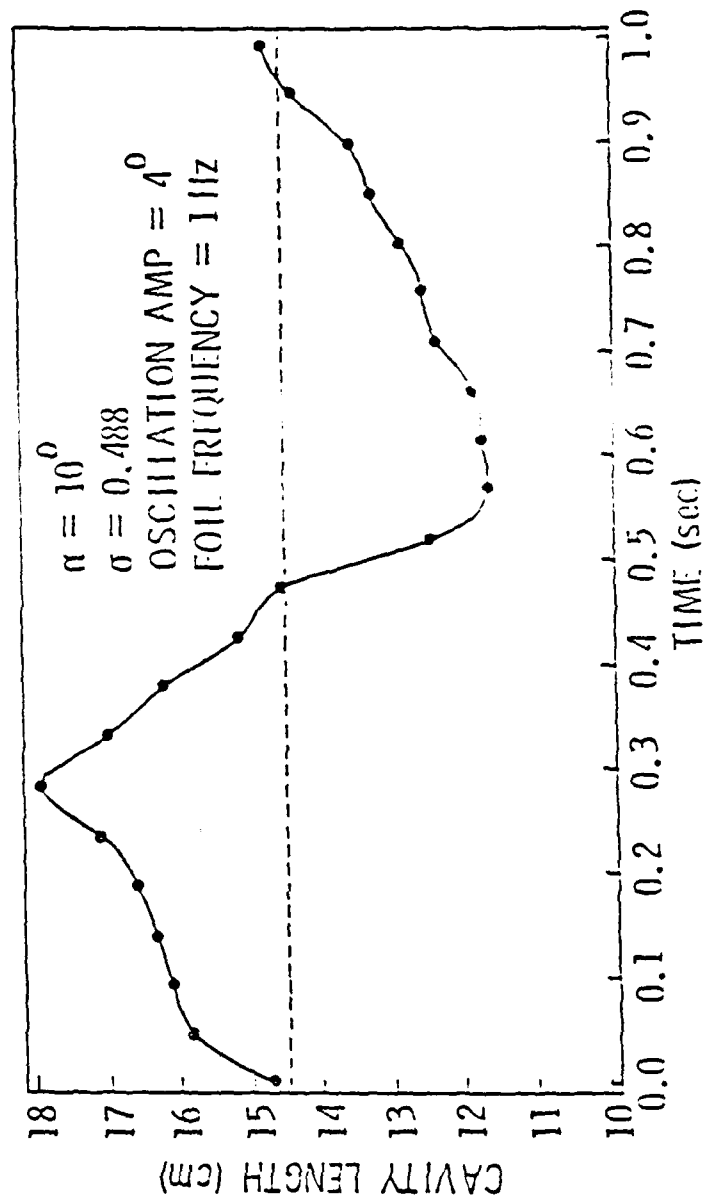


Figure 3.7(b). Time History of Cavity Length, 1.0 Hz.

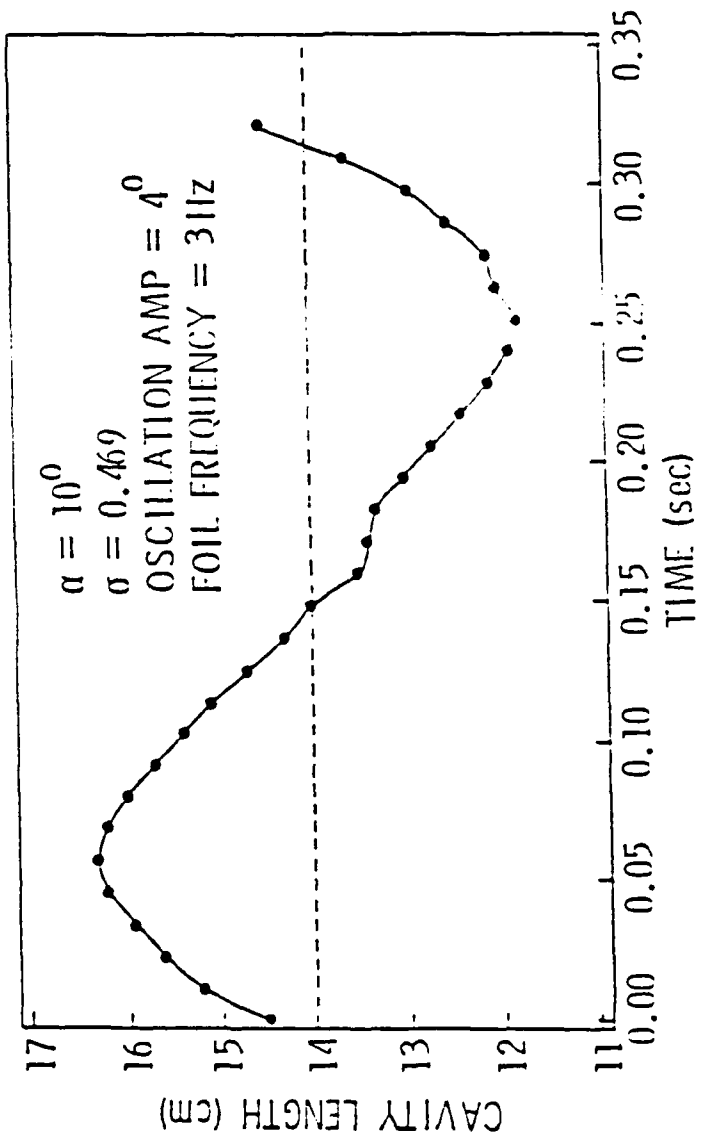


Figure 3.7(c). Time History of Cavity Motion, 3.0 Hz.

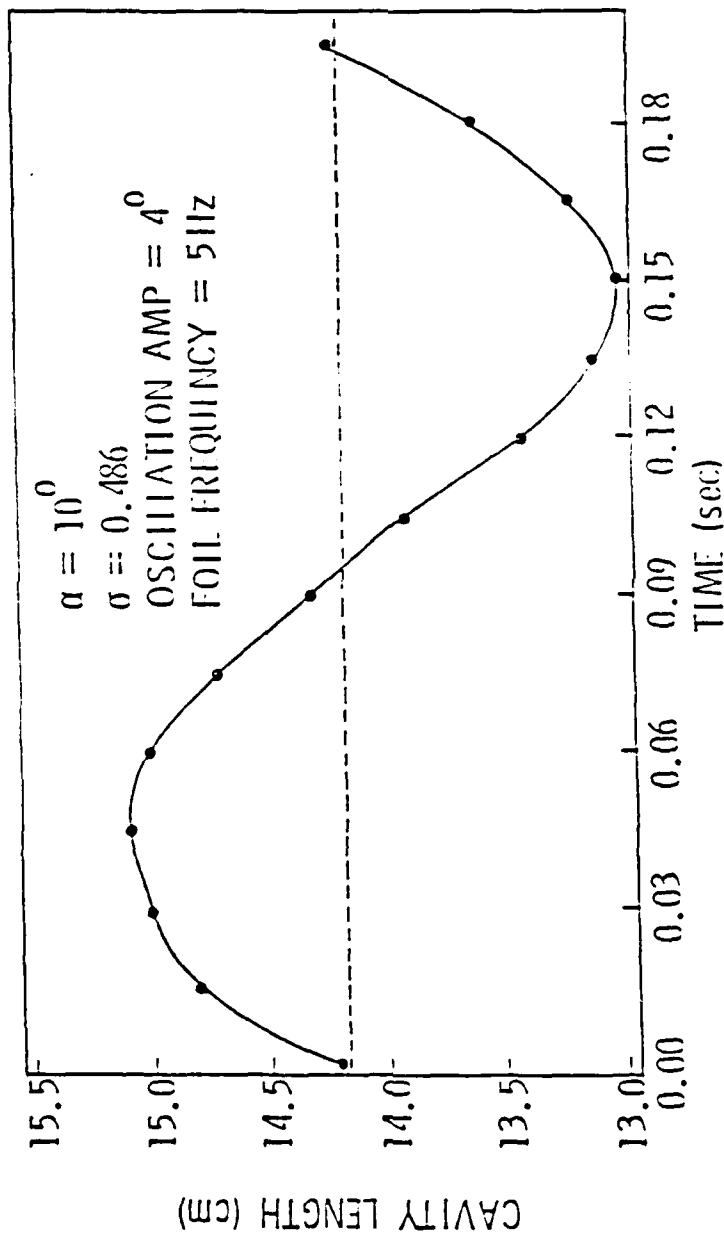


Figure 3.7(d). Time history of cavity length, 5.0 Hz.

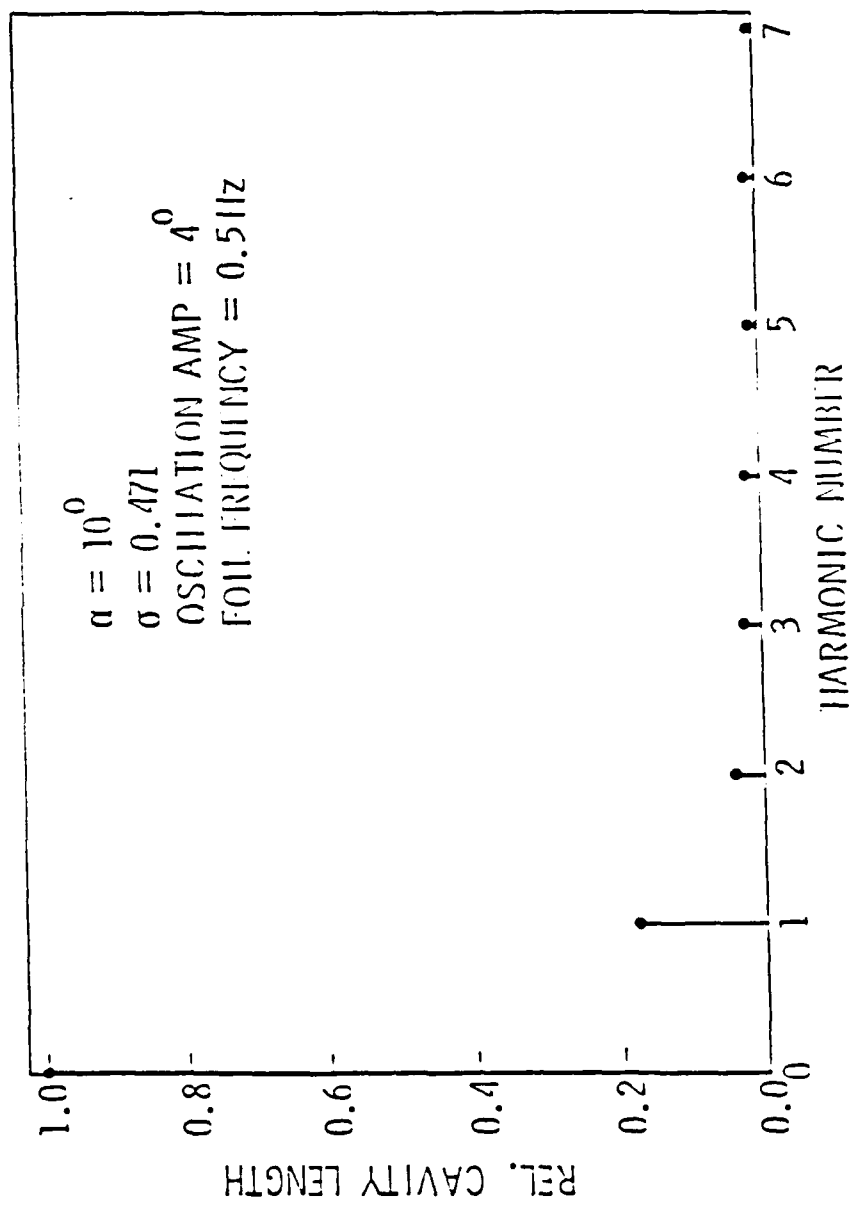


Figure 3.8(a). Spectrum of Cavity Length, 0.5 Hz.

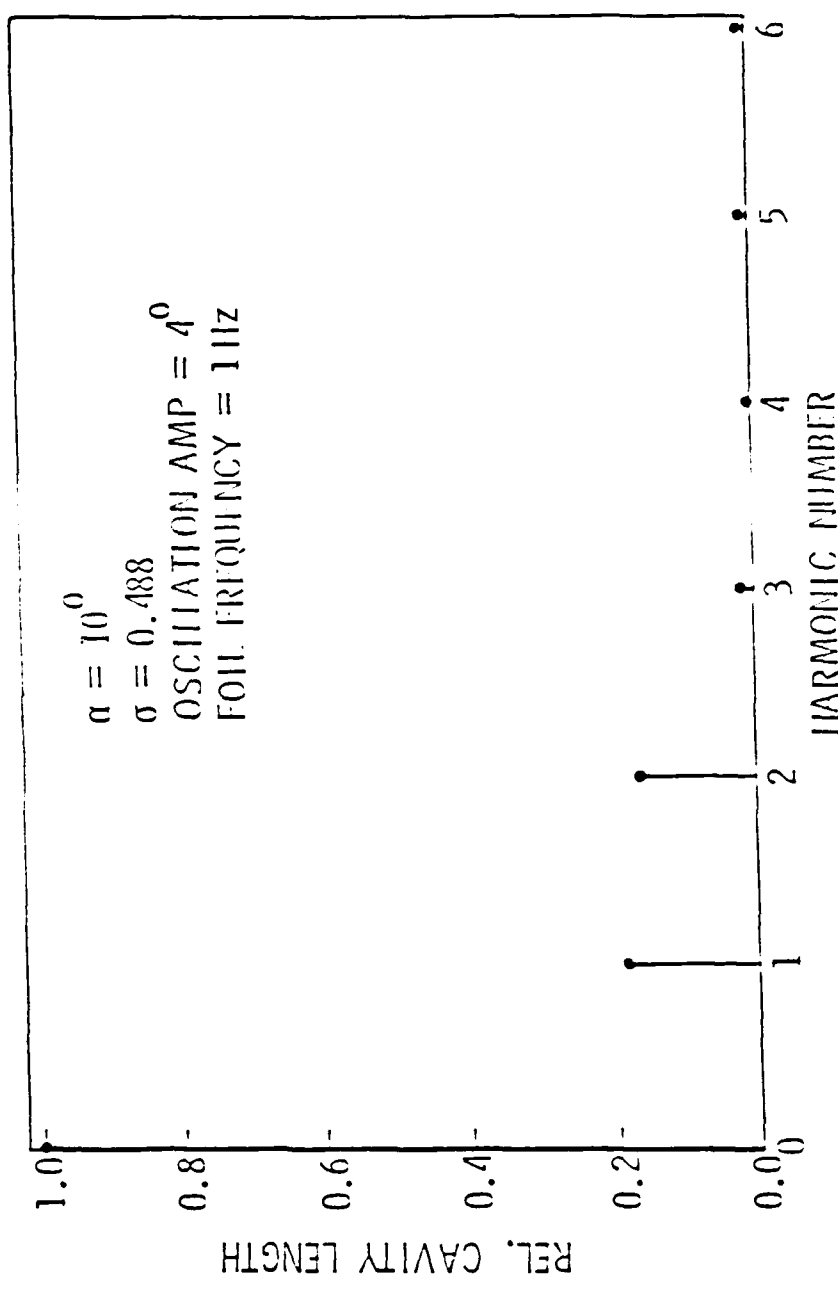


Figure 3.8(b). Spectrum of cavity length, 1.0 Hz.

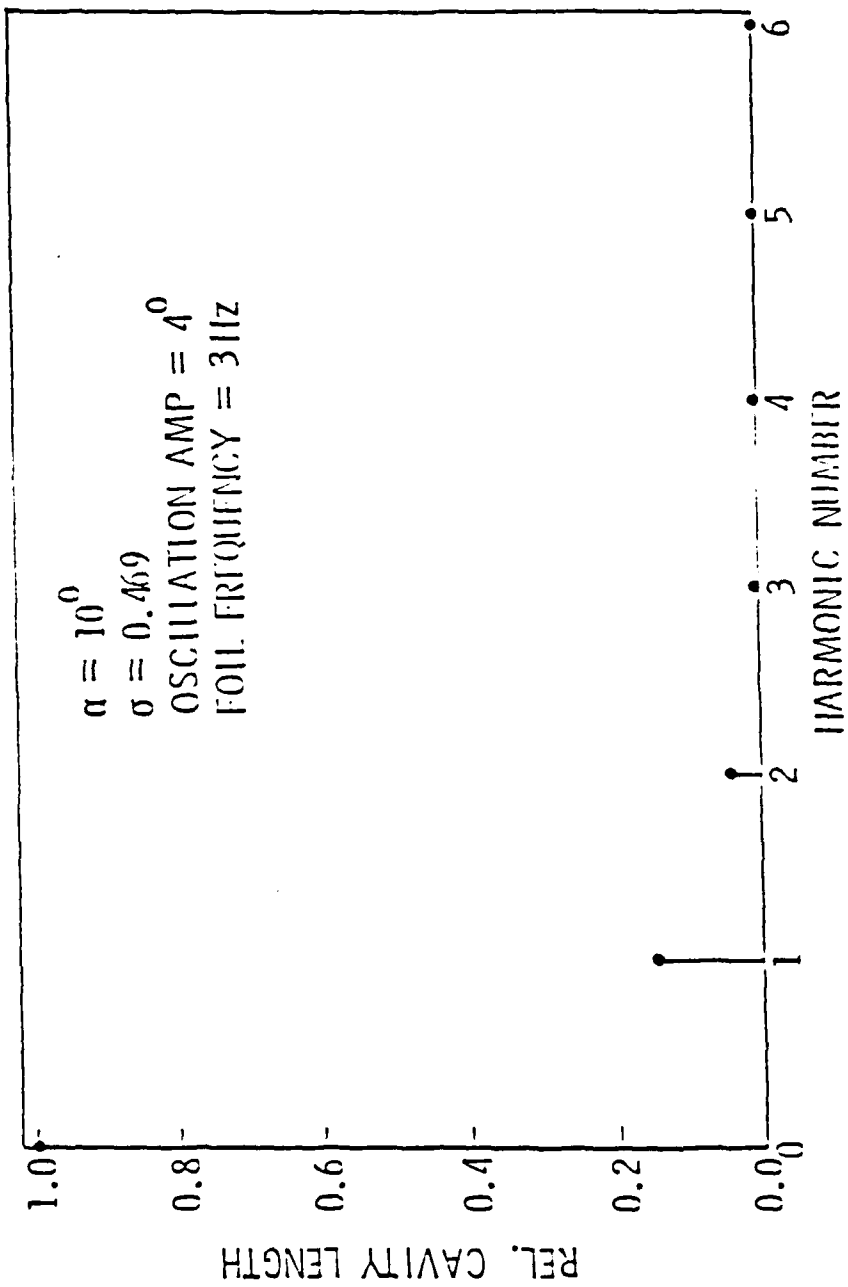


Figure 3.8(c). Spectrum of Cavity Motion, 3.0 Hz.

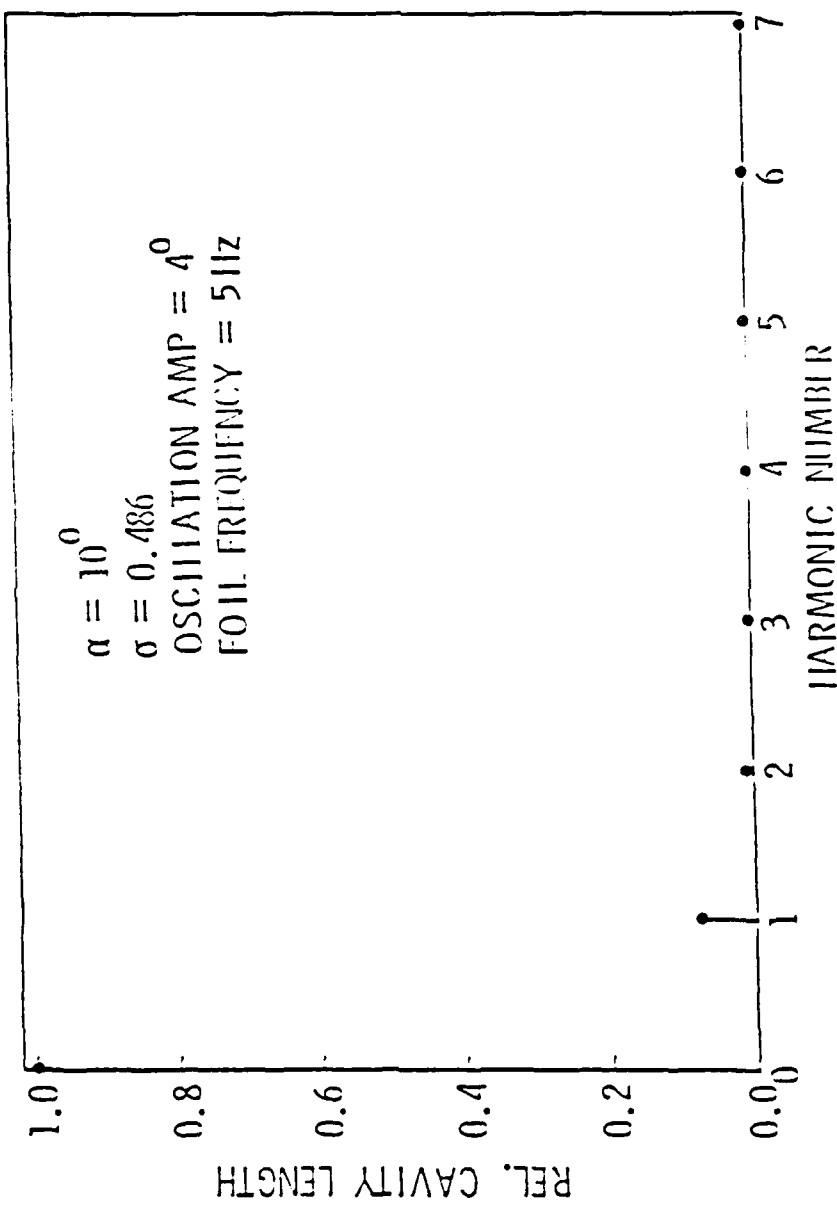


Figure 3.8(d). Spectrum of cavity motion, 5.0 Hz.

$$l(t) \approx \sqrt{\frac{2\alpha_0}{\sigma}} \left( 1 + \frac{\epsilon}{2} e^{j\omega t} - \frac{\epsilon^2}{8} e^{j2\omega t} + \dots \right) . \quad (3.3)$$

The similarity between the measured harmonic contents of cavity length and those obtained from Eq. (3.3) is now evident. Figure 3.9 shows the variation of amplitude of unsteady cavity motion (defined as the peak to peak amplitude normalized with respect to steady cavity length) as a function of the reduced frequency. It is clear that the amplitude of unsteady cavity motion decreases rapidly with increasing frequency. It is also of interest to observe that the amplitude of unsteady cavity motion peaks at a particular value of reduced frequency. Several attempts were made to measure the phase difference between the cavity motion and foil motion. Because of the extreme difficulty involved in such measurements, it is not surprising that no meaningful data were obtained, using the present measurement technique.

### 3.4.2 Source-Like Nature of Oscillating Cavity

Figures 3.10 and 3.11 show the plots of the relative root mean square pressure level in decibels at 32.5 inches upstream of the pitch axis as a function of the test section velocity. The foil oscillation frequency is relatively low, being less than 2 Hz. It is seen that the unsteady pressure varies as the sixth power of the test section velocity. This indicates that the oscillating cavity behaves like a dipole source even at these low frequencies [see for example, Donald Ross (26) and Billet and Thompson (27)]. Figure 3.12 shows a similar plot of unsteady pressure versus test section velocity at a point 32.5 inches downstream of the pitch axis. Here again, the

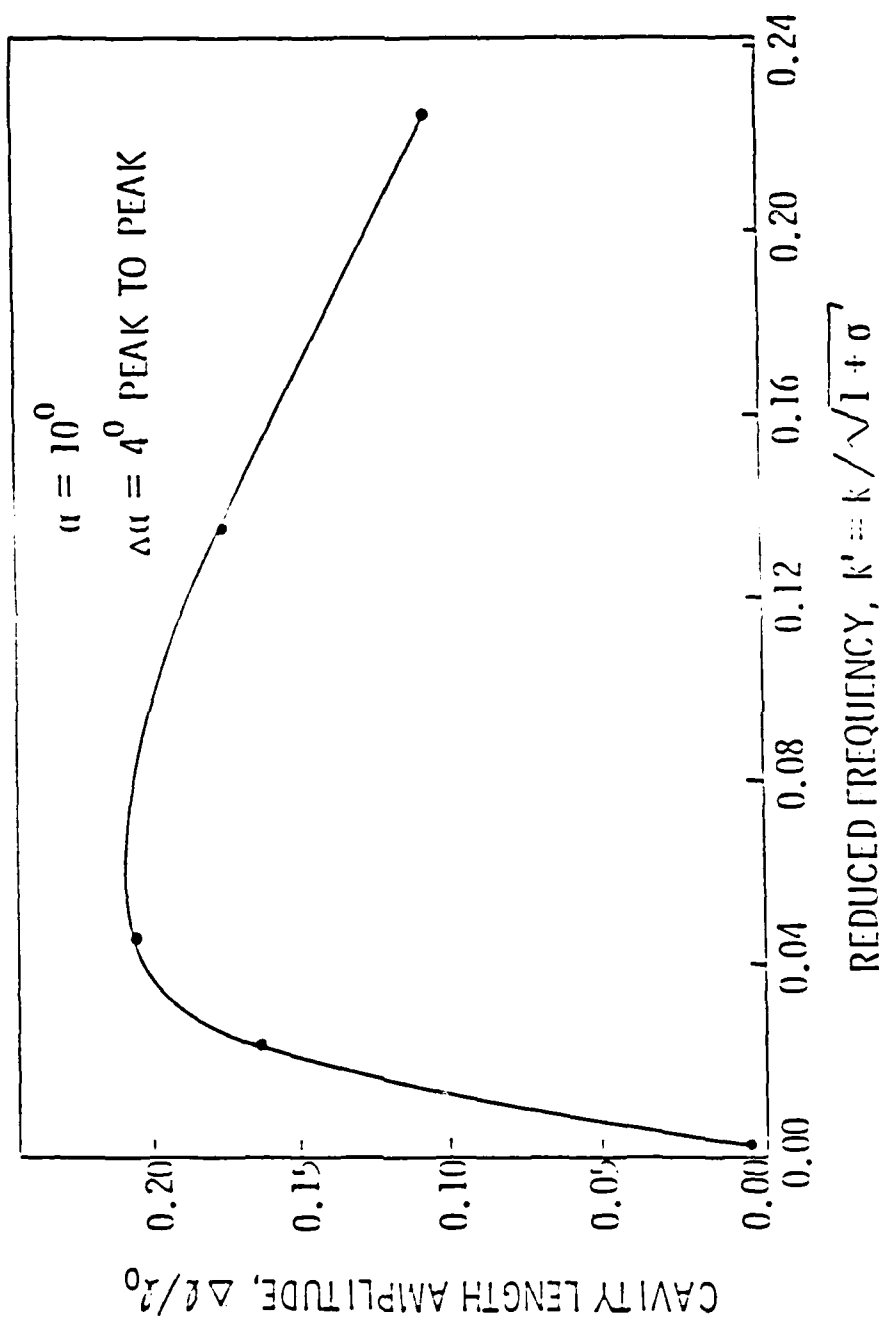


Figure 3.9. Cavity Length Amplitude Versus Reduced Frequency.

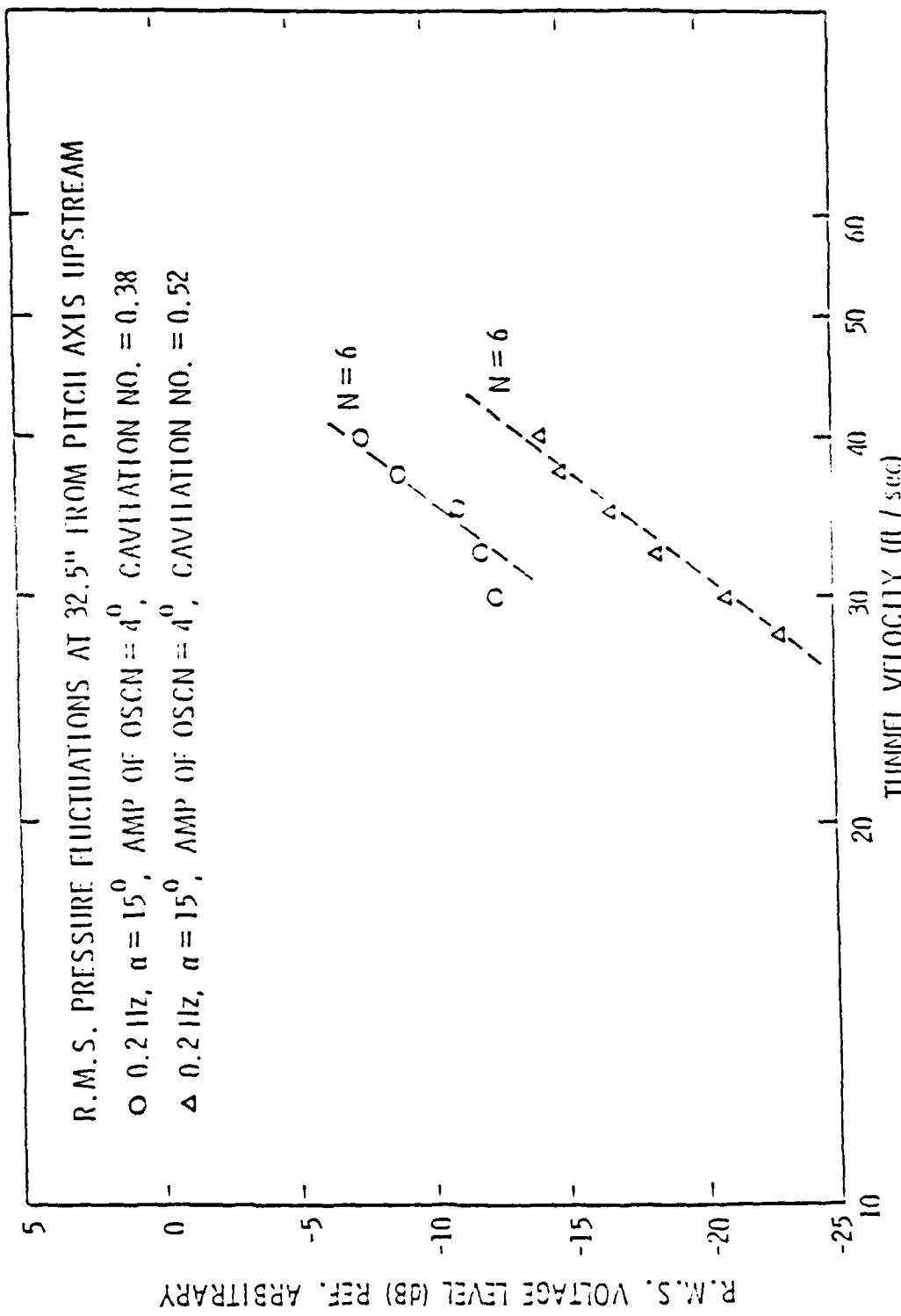


Figure 3.10. R.M.S. Pressure Level at 32.5 inches upstream versus Test Section Velocity.

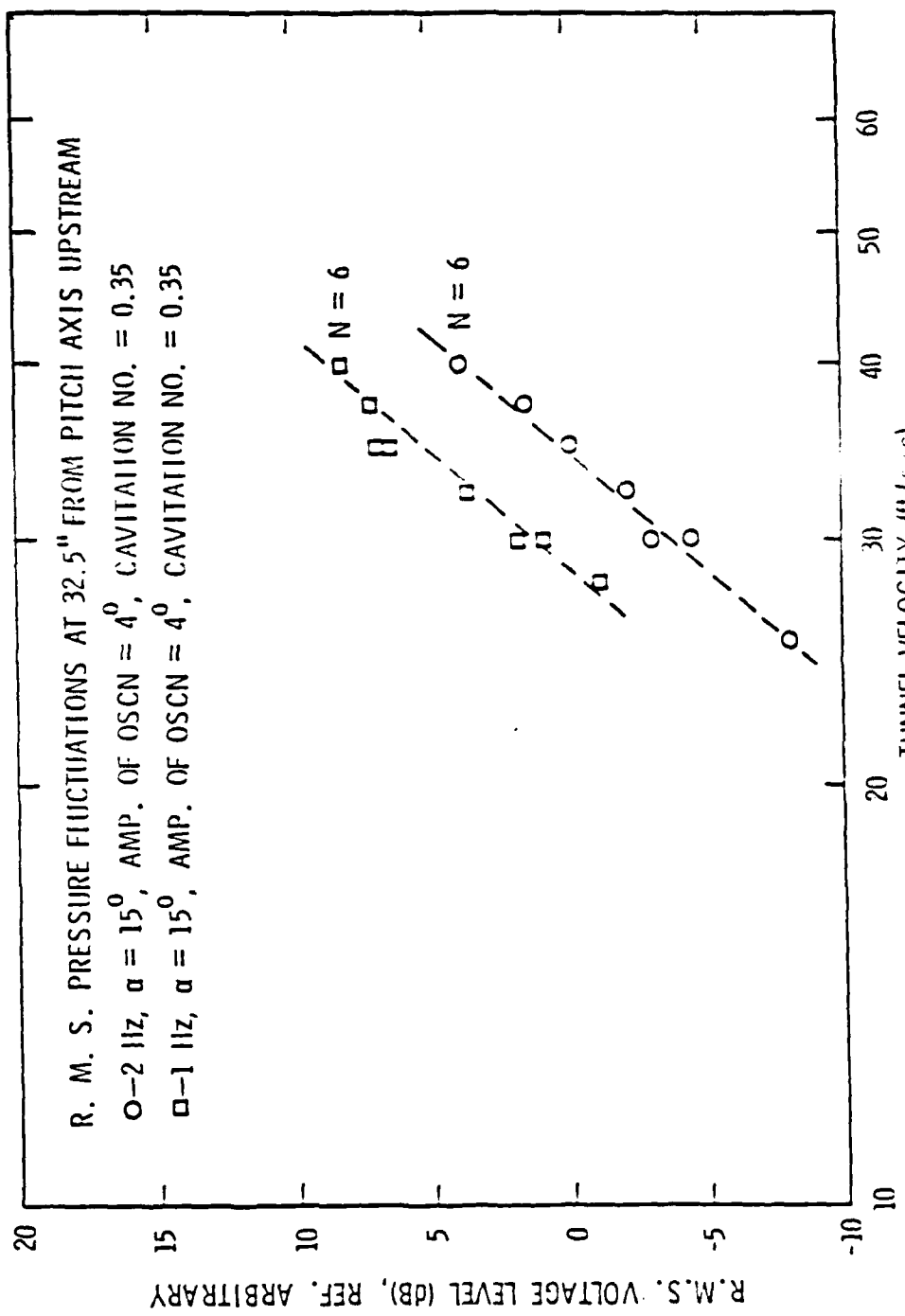


Figure 3.11 R.M.S. Pressure Level 32.5 Inches Upstream versus Test Section Velocity.

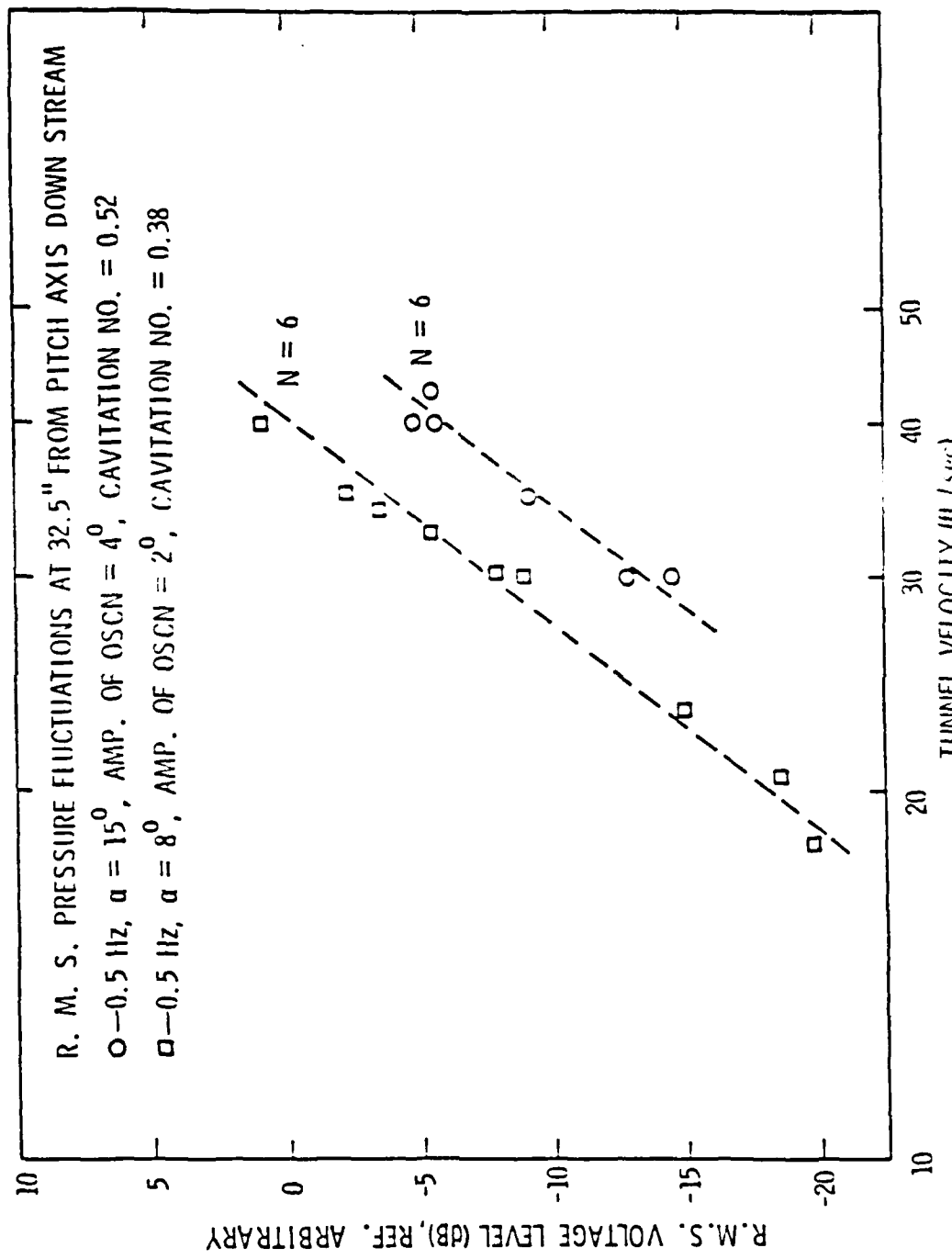


Figure 3.12 R.M.S. Pressure level at 32.5 inches downstream versus Test Section Velocity.

dipole behavior of the oscillating cavity is very clear. Figure 3.13 depicts the measurements at a location 16.325 inches upstream of the pitch axis. At an oscillation frequency of 10 Hz, the unsteady pressure varies as the eighth power of the test section velocity. This variation suggests that the oscillating cavity behaves like a quadrupole at this frequency. This is possibly due to the phase lag that exists between the motion of the foil and the motion of the cavity at high frequencies. The oscillating foil and the oscillating cavity each constitute a dipole source and with the adequate phase lag that exists between them at high frequencies, they jointly constitute a quadrupole source.

#### 3.4.3 Cavity Pressure Measurements

The measurement of steady cavity pressures as well as the unsteady cavity pressures were accurate to within 2%. The steady cavity pressure is normalized with respect to the ambient vapor pressure of water. The variation of normalized steady cavity pressure as a function of the parameter  $\sigma/\alpha$  is shown in Figure 3.14. The average value of the dissolved gas content in the tunnel water was 9 ppm by moles and the average value of the free air in the tunnel water was 4 ppm by volume during these tests. The steady cavity pressure is seen to be always greater than the vapor pressure of water at the ambient temperature. It is observed that larger cavities (lower cavitation numbers and/or higher angles of attack) sustain higher cavity pressures than smaller cavities. In the range of  $\sigma/\alpha$  between 2 and 6, it is observed that the steady cavity pressure has a nearly linear relation with  $\sigma/\alpha$ . Figure 3.15 shows the

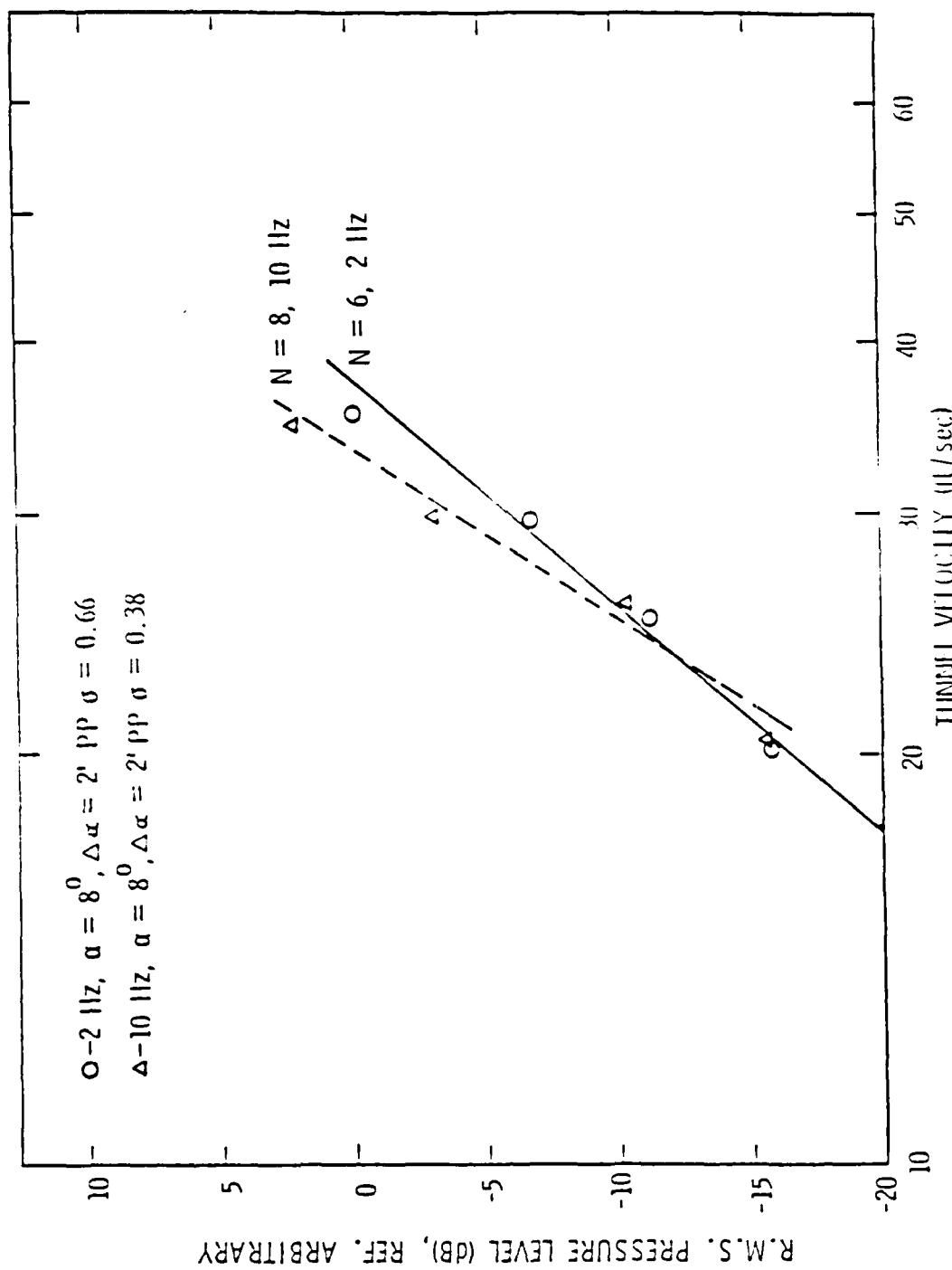


Figure 3.13. R.M.S. Pressure Level at 16.325 ft/sec Upstream versus Test Section Velocity.

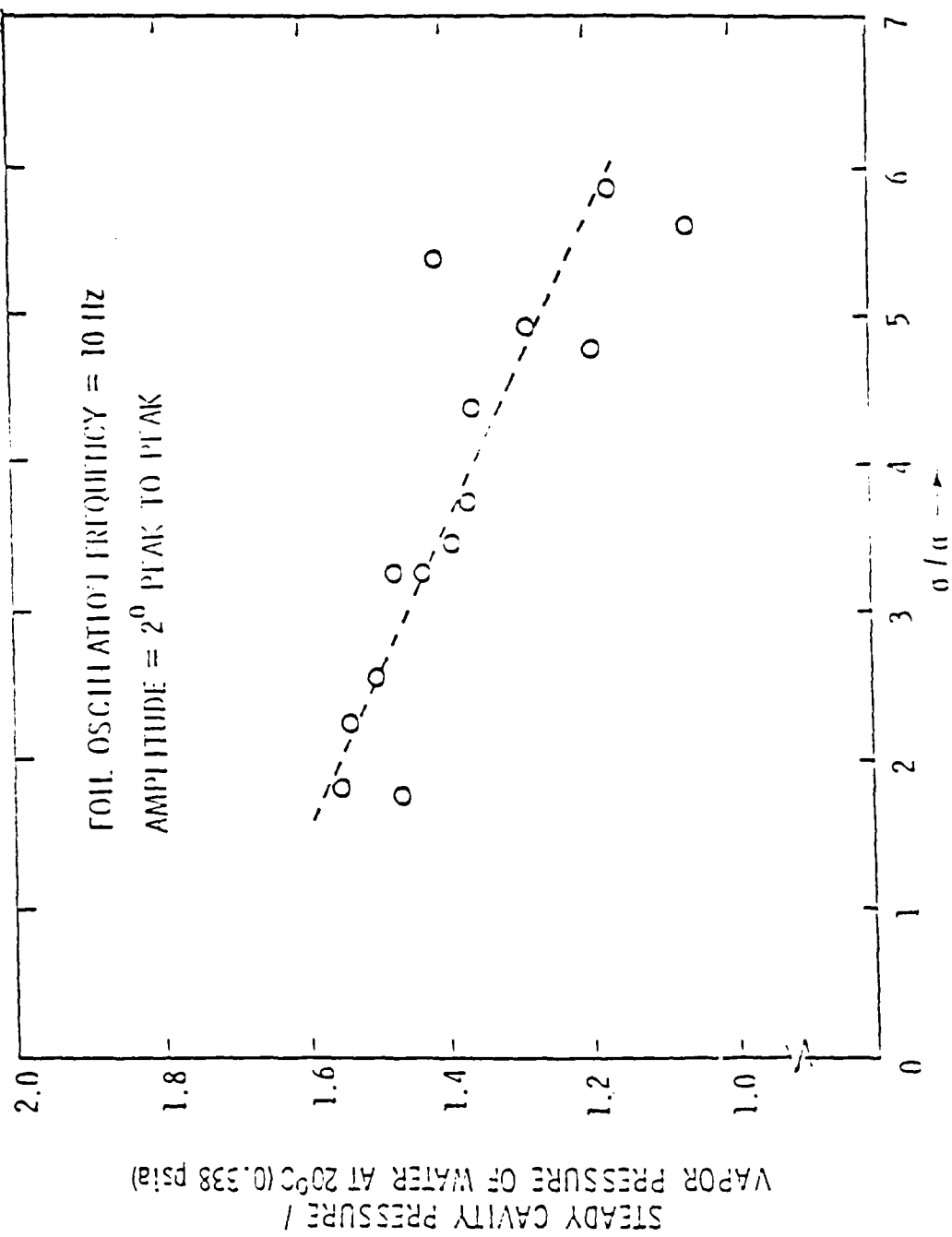


Figure 3.14. Normalized Steady Cavity Pressure versus  $\alpha / \alpha$ .

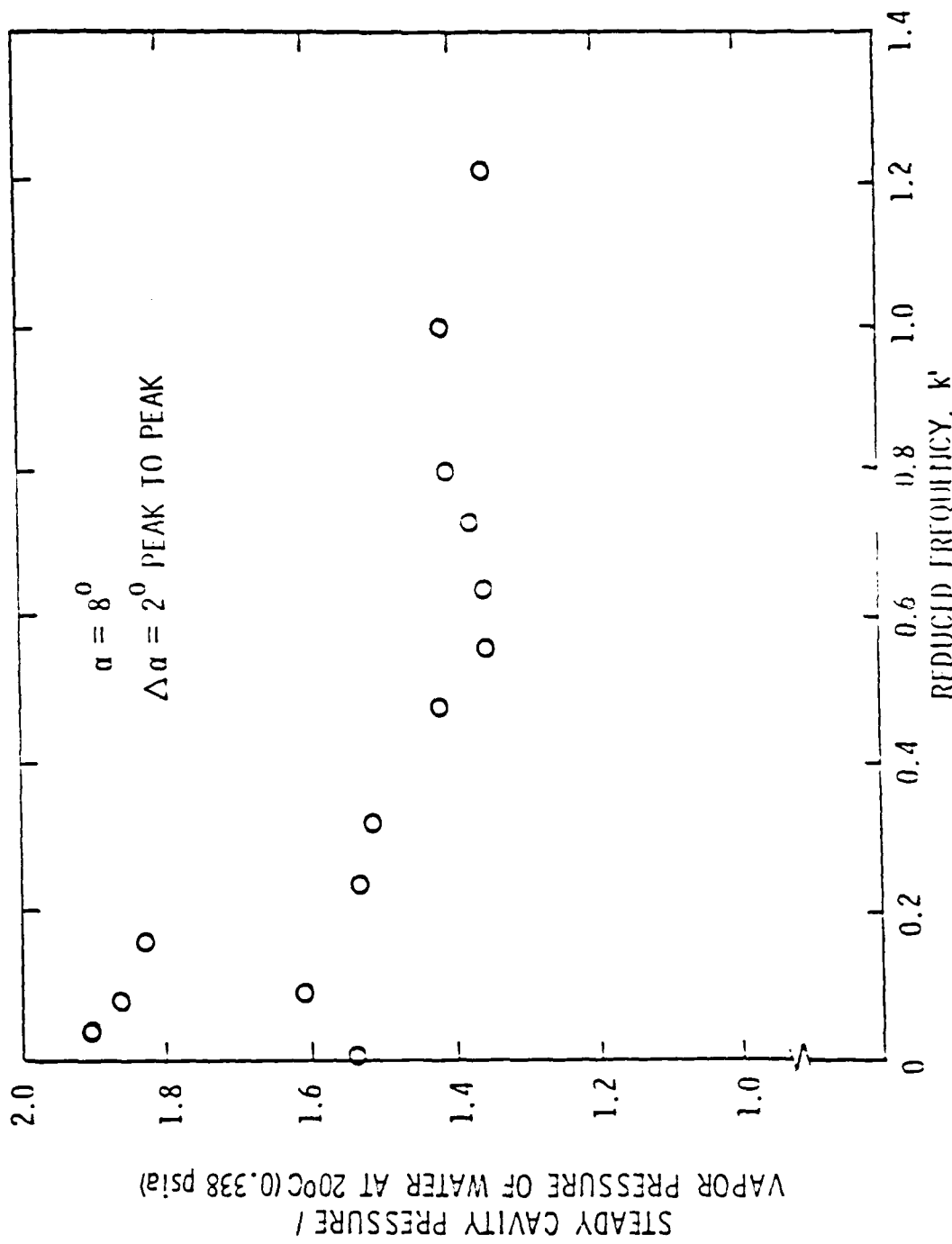


Figure 3.15. Normalized Steady Cavity Pressure versus  $k'$ .

variation of normalized steady cavity pressure at a steady angle of attack of 8 degrees as a function of the reduced frequency parameter  $k'$ . [Parkin (28) has shown that for cavitating oscillating foils, the appropriate non-dimensional frequency is  $k' = k/\sqrt{1 + \sigma}$ , where  $k$  is the reduced frequency in the non-cavitating case,  $k = \omega b/U_\infty$ .] The amplitude of oscillation is 2 degrees peak to peak. It is observed that the steady cavity pressure increases with frequency, reaches a maximum value and then decreases with further increase in frequency. This can possibly be explained by the entrainment process behind an oscillating cavity. As the oscillation frequency increases, it appears as though the re-entrant jet behind the cavity becomes increasingly stable until a certain frequency is reached. The stable re-entrant jet reduces air entrainment behind the cavity and hence the cavity is able to sustain higher cavity pressures. This situation however changes at high frequencies of foil oscillation wherein the re-entrant jet becomes unstable due to the high frequency surface waves interacting with the re-entrant jet. At high foil oscillation frequencies, the cavity remains essentially stationary and therefore the entrainment rate is equal to the gas diffusion rate resulting in constant cavity pressure. In other words, so far as steady cavity pressure is concerned, very low frequency oscillations of the cavity and very high frequency oscillations of the cavity have the same effect. It is quite interesting to observe that the frequency at which the maximum steady cavity pressure occurs and the frequency at which the maximum change in cavity length occurs (see Figure 3.9) are quite nearly the same, at  $k' = 0.04$ .

The variation of unsteady cavity pressure normalized with respect to the steady cavity pressure as a function of the reduced frequency is shown in Figure 3.16. Here the steady angle of attack is 15 degrees and the amplitude of foil oscillation is 4 degrees peak to peak. It is clear that the unsteady pressure peaks at a reduced frequency of about 0.05 and then drops off rapidly with increase in frequency. This behavior of unsteady cavity pressure with frequency may be explained from the unsteady cavity length data. At very high frequencies, there is very little motion of the cavity and hence the cavity pressure is very small. These trends in unsteady cavity pressures agree well with those of Jiang and Leehey (17). Figure 3.17 similarly shows the normalized unsteady cavity pressure as a function of reduced frequency at a steady angle of attack of 8 degrees and amplitude of oscillation of 2 degrees peak to peak. Here the peak unsteady cavity pressure occurs at a reduced frequency of 0.16. This is to be expected because the cavity at a foil angle of 8 degrees is smaller compared to the cavity at 15 degrees and hence it has a higher resonant frequency.

It is interesting to observe from Figure 3.14 that the linear relation between the cavity pressure and the parameter  $\sigma/\alpha$  enables one to estimate the cavitation number, based on cavity pressure, in terms of free stream static pressure, the vapor pressure at the ambient temperature, the free stream dynamic pressure and the angle of attack:

$$\sigma = \frac{p_\infty - 0.74 p_v}{q_\infty - \frac{0.0976}{\alpha} p_v} . \quad (3.4)$$

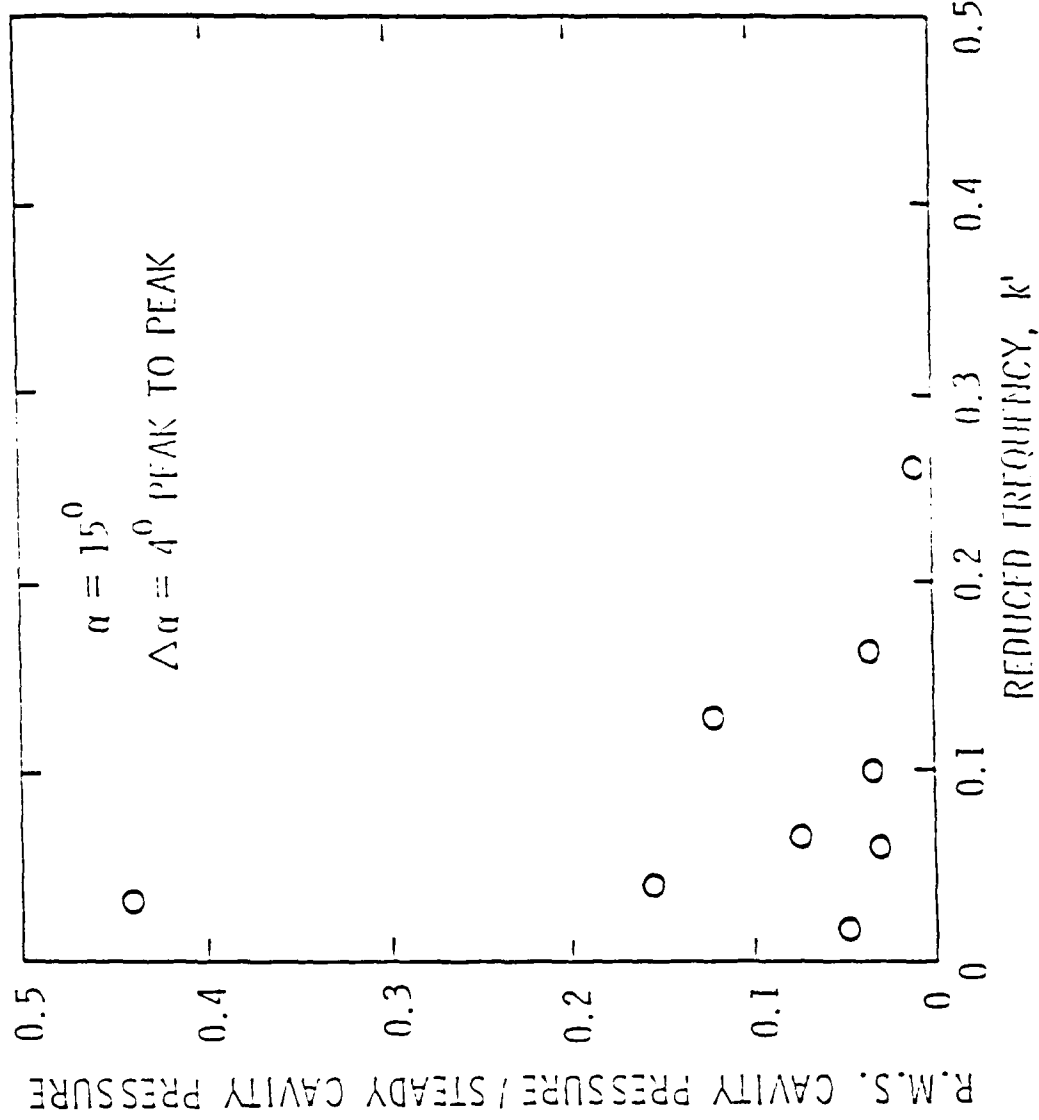


Figure 3.16. Normalized Unsteady Cavity Pressure versus  $k'$ ,  $\alpha = 15^0$ .

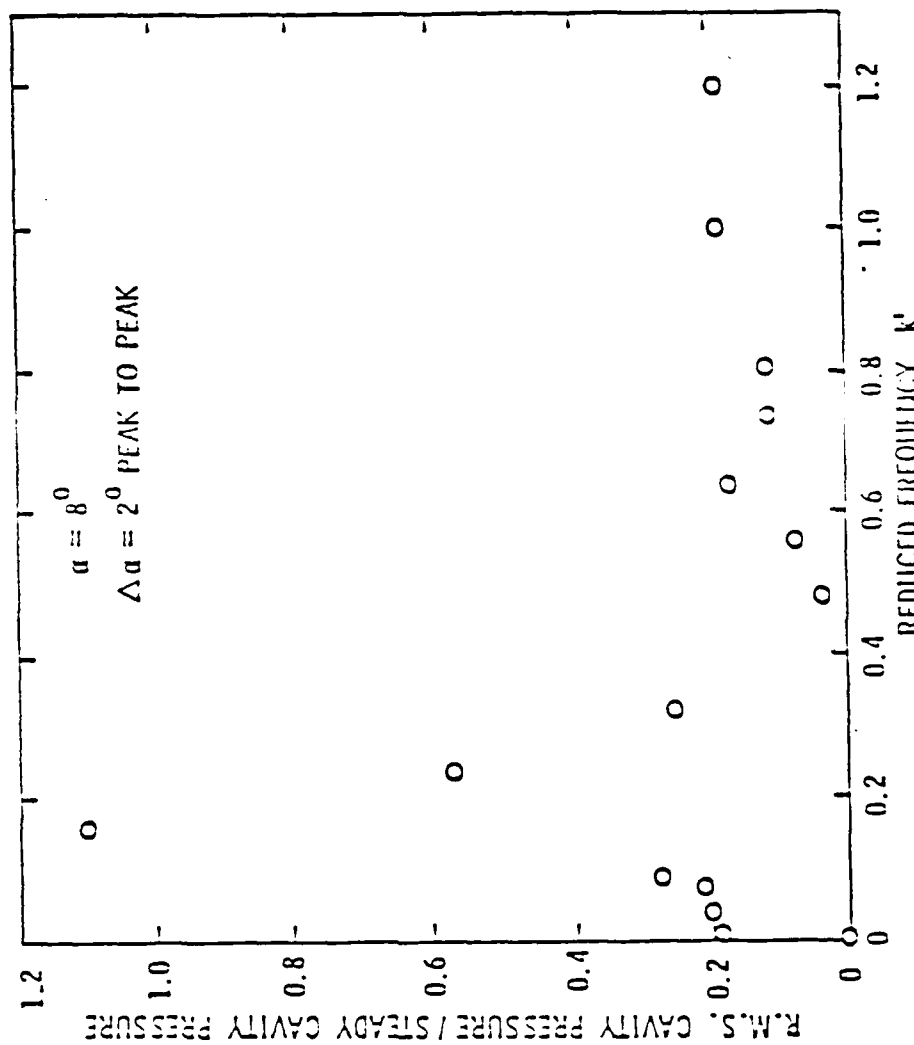


Figure 3.17. Normalized Unsteady Cavity Pressure versus  $k'$ ,  $\alpha = 8^\circ$

#### 3.4.4 Recapitulation

These experiments on unsteady cavities have given us some insight into their behavior. The variations in harmonic content for the motion of the cavity have been clearly established. The source-like nature of the oscillating cavity has been characterized as a dipole source at low frequencies of oscillation and approaches a quadrupole source at high frequencies. One would expect to see a monopole contribution as well because of the cavity volume fluctuations and Fig. 3.13 suggests such a possibility. However, this experimental fragment is overwhelmed by the bulk of the presently available data favoring higher-order singularities. Since the cavity and foil generally are rather large for a six-inch diameter test section, the influence of tunnel walls on these experimental findings remains to be investigated. Low cavitation numbers and/or high angles of attack result in higher cavity pressures. Unsteady cavity pressure is seen to be significant only at low frequencies of oscillation.

## CHAPTER 4

TWO-DIMENSIONAL UNSTEADY DIFFUSION ACROSS  
A PERMEABLE CAVITY SURFACE4.1 Introduction

From the previous studies on cavity pressure fluctuations by Jiang and Leehey (17) and the present experimental investigations described in Chapter 3, it is clear that gaseous diffusion plays a very important role in the behavior of unsteady cavities. Parkin (8) studied steady diffusion across a two-dimensional cavity surface, while Brennen (9) considered steady diffusion across a cavity surface from a turbulent flow.

It appears however, that a corresponding analysis for unsteady diffusion in an unsteady cavity flow is, to the best of our knowledge, non-existent. Unsteady gaseous diffusion into a cavity may result from two distinct mechanisms. First, since the cavity length fluctuates, the gaseous diffusion into the cavity fluctuates. Second, since the cavity gas pressure itself fluctuates, the concentration gradient across the cavity surface is a function of time. In this chapter, we formulate and solve analytically, the unsteady gaseous diffusion across a two-dimensional unsteady cavity surface. The results of this analysis will give a better understanding of the parameters that affect the unsteady gaseous diffusion across a cavity surface.

4.2 Assumptions

It is assumed in the following analysis that the flow is incompressible, two-dimensional, isotropic and turbulent. (Turbulence is inherently three-dimensional in nature. Nonetheless, a two-dimensional flow field with unit depth may be considered for diffusion

analysis.) Boussinesq's hypothesis (29) is used in turbulence modeling and G. I. Taylor's (30) statistical theory of turbulence is used in estimating the mass diffusivity for the flow field. It is assumed that the mechanism for turbulent momentum transfer and turbulent concentration transfer are identical. It is also assumed that the gaseous diffusion occurs instantaneously across the cavity surface.

#### 4.3 Theoretical Analysis

Gaseous diffusion will occur when there exists a dissolved-gas concentration difference between the free stream and the liquid on the cavity surface. If  $\alpha_1$  denotes the dissolved gas content in the free stream in parts per million, by moles, then by Henry's law, the maximum partial pressure of gas in the free stream  $P_{FS}$  is

$$P_{FS} = \alpha_1 \beta , \quad (4.1)$$

where  $\beta$  is the Henry's law constant. If  $p_G(t)$  is the instantaneous partial pressure of non-condensable gas in the cavity, then the mean concentration difference  $c(t)$  expressed in moles is

$$c(t) = \left( \alpha_1 - \frac{p_G}{\beta} \right) . \quad (4.2)$$

We assume, as is customary, that the mechanism for turbulent diffusion of gas in the liquid and across the wall and the turbulent momentum transfer are similar and that gradients in mean velocity can be neglected. Then, the turbulent diffusion is due solely to the gradient of the mean concentration  $c(x,y)$ . Consider a turbulent flow field having a uniform mean velocity  $U_\infty$  in the positive x-direction, as shown in Figure 4.1. Let the instantaneous concentration at a point  $(x,y)$  be  $C(x,y,t)$ . Also, let  $C_\infty$  be the concentration at large distances

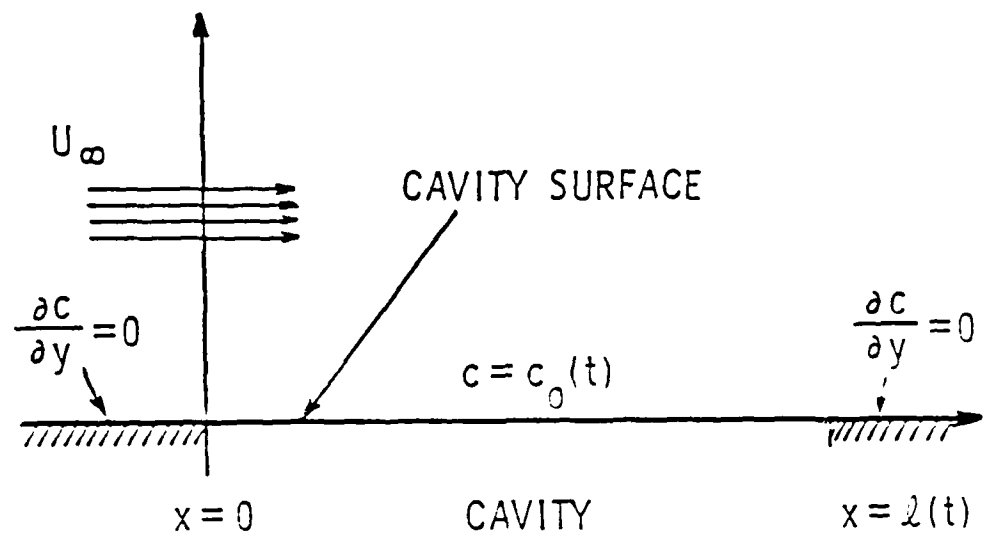


Figure 4.1 Boundary Conditions for Unsteady Gaseous Diffusion Analysis

from the origin and  $C_0$  be the saturation concentration on the cavity wall. Let  $c = C - C_\infty$  be the concentration difference. From Fick's law of diffusion and conservation of mass [see, for example, Batchelor (31)] it follows that

$$(\vec{U} \cdot \nabla)c + \frac{\partial c}{\partial t} = \kappa \nabla^2 c \quad (4.3)$$

where  $\nabla^2$  denotes the Cartesian Laplacian operator and  $\kappa$  is the molecular diffusivity.

Let the instantaneous velocity components be represented by  $(U_\infty + u')$ ,  $v'$  and  $w'$  in the three orthogonal directions and let  $c = \bar{c} + c'$  where  $\bar{c}$  is the time mean concentration difference. The components  $u'$ ,  $v'$  and  $w'$  are the instantaneous velocity fluctuations and  $c'$  is the instantaneous concentration difference. Then, Eq. (4.3) becomes [see, for example, Goldstein (32)]

$$\begin{aligned} \frac{\partial \bar{c}}{\partial t} + U_\infty \frac{\partial \bar{c}}{\partial x} - \kappa \nabla^2 \bar{c} + \frac{\partial c'}{\partial t} + [U_\infty \frac{\partial c'}{\partial x} + u' \frac{\partial \bar{c}}{\partial x} + u' \frac{\partial c'}{\partial x} + v' \frac{\partial \bar{c}}{\partial y} + v' \frac{\partial c'}{\partial y} \\ + w' \frac{\partial \bar{c}}{\partial z} + w' \frac{\partial c'}{\partial z}] - \kappa \nabla^2 c' = 0 \end{aligned} \quad (4.4)$$

Time-averaging the above equation, we obtain

$$\frac{\bar{\partial} \bar{c}}{\partial t} + U_\infty \frac{\bar{\partial} \bar{c}}{\partial x} = \frac{\partial}{\partial x} (\kappa \frac{\bar{\partial} \bar{c}}{\partial x} - \bar{u}' \bar{c}') + \frac{\partial}{\partial y} (\kappa \frac{\bar{\partial} \bar{c}}{\partial y} - \bar{v}' \bar{c}') + \frac{\partial}{\partial z} (\kappa \frac{\bar{\partial} \bar{c}}{\partial z} - \bar{w}' \bar{c}') \quad (4.5)$$

where the overbar indicates time averaging. Equation (4.5) shows that in turbulent flows the eddy concentration transport terms  $-\bar{u}' \bar{c}'$ ,  $-\bar{v}' \bar{c}'$  and  $-\bar{w}' \bar{c}'$  add to the molecular concentration transports  $\kappa \frac{\bar{\partial} \bar{c}}{\partial x}$ ,  $\kappa \frac{\bar{\partial} \bar{c}}{\partial y}$  and  $\kappa \frac{\bar{\partial} \bar{c}}{\partial z}$

$\propto \frac{\partial \bar{c}}{\partial z}$  respectively. The eddy transport terms are large compared to molecular transport terms (32). Therefore, the latter are neglected and Eq. (4.5) reduces to

$$\frac{\partial \bar{c}}{\partial t} + U_\infty \frac{\partial \bar{c}}{\partial x} = - \frac{\partial}{\partial x} (\bar{u}'\bar{c}') - \frac{\partial}{\partial y} (-\bar{v}'\bar{c}') - \frac{\partial}{\partial z} (-\bar{w}'\bar{c}') . \quad (4.6)$$

We now restrict our study to two-dimensional flows. We represent the turbulent shear stress  $\rho \bar{u}'\bar{c}'$  and  $\rho \bar{v}'\bar{c}'$  using Boussinesq's hypothesis as

$$- \rho \bar{u}'\bar{c}' = A_T \frac{\partial \bar{c}}{\partial x} , \quad (4.7a)$$

and

$$- \rho \bar{v}'\bar{c}' = A_T \frac{\partial \bar{c}}{\partial y} , \quad (4.7b)$$

where  $A_T$  is the exchange coefficient or eddy mass conductivity. Let  $v_T$  denote the eddy mass diffusivity. Then,

$$v_T = A_T / \rho , \quad (4.8)$$

where  $\rho$  is the density of the liquid. Substitution of Eqs. (4.7) and (4.8) in (4.6) yields

$$\frac{\partial \bar{c}}{\partial t} + U_\infty \frac{\partial \bar{c}}{\partial x} = v_T \left( \frac{\partial^2 \bar{c}}{\partial x^2} + \frac{\partial^2 \bar{c}}{\partial y^2} \right) . \quad (4.9)$$

The boundary conditions pertinent to the two-dimensional unsteady diffusion are:

$$\frac{\partial \bar{c}}{\partial y} = 0 ; \quad y = 0, \quad x < 0 , \quad x > l \quad (4.10a)$$

and

$$\bar{c} = c_o (1 + \hat{c}(t)) ; y = 0, 0 < x < l \quad (4.10b)$$

where  $l(t)$  is the unsteady cavity length given by

$$l(t) = l_o (1 + \hat{\epsilon} l(t)) , \quad (4.11)$$

where  $\epsilon$  is a small quantity.

We now let

$$\bar{c}(x, y, t) = \bar{c}_s(x, y) + \bar{c}_u(x, y, t) , \quad (4.12)$$

where  $\bar{c}_s$  and  $\bar{c}_u$  represent respectively, the steady part and unsteady part of the concentration  $\bar{c}$ .

Substitution of Eq. (4.12) in Eq. (4.9) results in two equations

$$U_\infty \frac{\partial \bar{c}_s}{\partial x} = v_t \left( \frac{\partial^2 \bar{c}_s}{\partial x^2} + \frac{\partial^2 \bar{c}_s}{\partial y^2} \right) , \quad (4.13a)$$

and

$$\frac{\partial \bar{c}_u}{\partial t} + U_\infty \frac{\partial \bar{c}_u}{\partial x} = v_t \left( \frac{\partial^2 \bar{c}_u}{\partial x^2} + \frac{\partial^2 \bar{c}_u}{\partial y^2} \right) . \quad (4.13b)$$

The steady partial differential equation (4.13a) satisfies the steady part of the boundary condition (4.10b) viz.,

$$\bar{c}_s = c_o ; y = 0, 0 < x < l_o . \quad (4.14)$$

The unsteady partial differential equation (4.13b) satisfies the unsteady part of the boundary condition (4.10b) viz.,

$$\bar{c}_u = c_0 \hat{c}(t) ; y = 0, 0 < x < l(t) . \quad (4.15)$$

The steady partial differential equation has been solved by Parkin (8). The solution of Eq. (4.13b) subject to the boundary conditions (4.15) is obtained in stages. First, a point source solution that has the proper radial symmetry and behavior is obtained. Second, the point source solution is used to formulate an integral equation relating the concentration at a fixed point and the mass flux per unit length along the cavity. Third, the concentration difference at the cavity surface is used to solve the integral equation.

The fundamental solution of Eq. (4.13b) for an oscillating unit source at the origin is (See Appendix C.1)

$$\bar{c}(x, y; k) = \frac{i}{2\pi A_T} K_0(R \sqrt{x^2 + y^2}) e^{(R-jk)x} , \quad (4.16)$$

where  $K_0(z)$  is the modified Bessel's function of the second kind. It should be noted that  $r$ ,  $x$  and  $y$  appearing in Equation (4.16) are

dimensionless and that  $R = \frac{U_\infty b}{2v_t}$ , a "diffusive Reynold's number."

We now introduce the harmonic oscillations of the unsteady boundary conditions resulting from the angle of attack oscillations at a circular frequency of  $\omega$  radians per second. Suppose that the cavity length oscillations lag the foil oscillations (see Chapter 5) by a phase angle of  $\phi$ . Then, the unsteady cavity length at  $x = l_0$  is given by  $\epsilon l_0 e^{j(\omega t + \phi)}$  or  $\epsilon l_0 e^{j\phi} e^{j\omega t}$ .

The gas pressure within the cavity  $P_G(t)$  may be written as

$$p_G(t) = p_{G0}(1 + \delta \hat{p}(t)) , \quad (4.17)$$

where  $\delta$  is a small quantity.

With the assumption that the harmonic cavity pressure fluctuations lag the foil oscillations by  $\phi_a$ , we may write from Eq. (4.2),

$$c(t) = (\alpha_1 - \alpha_a) - \alpha_a \delta \hat{p} , \quad (4.18)$$

So that the concentration fluctuation  $c_u(t)$  across the permeable surface is given by

$$c_u(t) = - \alpha_a \delta e^{i(\omega t + \phi_a)} ,$$

i.e.,

$$c_u(t) = + \alpha_a \delta e^{i(\tau + \phi_a)} e^{j\omega t} , \quad (4.19)$$

where  $\phi_a$  is the phase angle between foil motion and cavity pressure fluctuations. Equation (4.19) clearly indicates a phase lag of  $\pi$  radians between the concentration fluctuations and cavity pressure fluctuations.

The steady concentration difference  $c_0$  at the permeable surface is

$$c_0 = (\alpha_1 - \alpha_a) . \quad (4.20)$$

Let  $f(x;k)$  be the mass flux per unit length. Then the function  $c(x,y;k)$  can be expressed in terms of  $f(x;k)$  as follows:

$$c(x,y;k) = \frac{1}{2\pi A_T} \int_0^{\tilde{x}} f(\xi;k) e^{(R-jk)(x-\xi)} K_0(R(x-\xi)^2 + y^2) d\xi , \quad (4.21)$$

where

$$\tilde{x} = \frac{\ell_0}{b} (1 + \epsilon e^{j\phi}) .$$

If we now require that  $c(x,0;k) = c_0 - \alpha_a \delta e^{jk\phi}$  in the interval  $0 < x < \bar{l}$ ,

the source strength is determined from the integral equation

$$c_0 - \alpha_a \delta e^{jk\phi} = \frac{1}{2\pi A_T} \left[ \int_0^x f(\xi;k) e^{R(x-\xi)} K_0(R(x-\xi)) e^{-jk(x-\xi)} d\xi \right. \\ \left. + \int_x^{\bar{l}} f(\xi;k) e^{-R(\xi-x)} K_0(R(\xi-x)) e^{jk(\xi-x)} d\xi \right] , \quad (4.22)$$

where the positive branch of the square root has been taken. The function  $c(x,y;k)$  also satisfies the conditions that  $c \rightarrow 0$  as  $(x^2 + y^2) \rightarrow \infty$  and that  $\partial c / \partial y(x,0) = 0$  when  $x < 0$  and  $x > \bar{l}$ .

In Eq. (4.22) we have combined the steady as well as the unsteady boundary conditions for both cavity length and cavity pressure. The reason for this is that the point source solution in the unsteady case reduces to the steady source solution as the reduced frequency  $k$  goes to zero. This fact also implies that  $\delta = \delta(k,\sigma)$ ,  $\epsilon = \epsilon(k,\sigma)$  and that  $\delta$  and  $\epsilon$  both vanish as  $k \rightarrow 0$ .

In order to determine  $f(x;k)$ , we shall make use of the fact that  $R$  is a large number for the present study. Therefore,  $K_0$  in Eq. (4.22) can be replaced by the first term of its asymptotic expansion,

$$K_0(z) \approx e^{-z} \sqrt{\frac{\pi}{2z}} . \quad (4.23)$$

A further simplification can be obtained in the second integral in Eq. (4.22) by noting that the strong negative exponential will cause  $f(\xi;k)$  to contribute to the integration only near  $\xi = x$ . Therefore, we replace the second integral in Eq. (4.22) by the approximate value,  $\sqrt{\frac{\pi}{2R}} f(x;k) \frac{\sqrt{\pi}}{\sqrt{2R-jk}}$ .

With these approximations, Eq. (4.22) may be written as

$$c_0 - \alpha_a \delta e^{j\phi_a} = \frac{1}{2\pi A_T} \frac{\pi}{2R} \left[ \int_0^x \frac{f(\xi; k) e^{-jk(x-\xi)}}{\sqrt{x-\xi}} d\xi + \frac{f(x; k) \sqrt{\pi}}{\sqrt{2R-jk}} \right]. \quad (4.24)$$

If the Laplace transform of  $f(x; k)$  is denoted by  $F(s; k)$ , we can transform Eq. (4.24) to find

$$F(s; k) = \frac{2A_T \sqrt{2R} (c_0 - \alpha_a \delta e^{j\phi_a})}{s \left[ \frac{1}{(s+jk)^{1/2}} + \frac{1}{(2R-jk)^{1/2}} \right]}. \quad (4.25a)$$

Rearranging terms, we have

$$F(s; k) = \frac{2A_T \sqrt{2R} (c_0 - \alpha_a \delta e^{j\phi_a}) \sqrt{2R-jk} \sqrt{s+jk}}{s [\sqrt{2R-jk} + \sqrt{s+jk}]} \quad (4.25b)$$

The inverse of this transform gives (see Appendix C.2) for  $f(x; k')$  the result,

$$f(x; k) = Q \left[ \frac{a}{\bar{a}} - \frac{b^2}{\bar{a}} e^{-\bar{a}x} \operatorname{erfc}(b\sqrt{x}) - \frac{b\sqrt{a}}{\bar{a}} \operatorname{erf}\sqrt{ax} \right], \quad (4.26)$$

where

$$Q = 2A_T \sqrt{2R} (c_0 - \alpha_a \delta e^{j\phi_a}) \sqrt{2R-jk}, \quad (4.27a)$$

$$a = jk, \quad (4.27b)$$

$$b = \sqrt{2R-jk}, \quad (4.27c)$$

$$\bar{a} = 2jk - 2R, \quad (4.27d)$$

$$\bar{b} = \bar{b}(t)/\bar{b} \text{ as before,}$$

and  $\text{erf}(x)$  and  $\text{erfc}(x)$  denote the error function and complimentary error function respectively. We note here the fact that the function  $f(x;k)$  which represents the mass flux per unit length is independent of the cavity length.

The rate at which the mass is diffused per unit width along the entire length of the permeable interval is obtained from

$$\dot{M}(k) = \int_0^l f(x,k) dx, \quad (4.28)$$

$$\text{i.e., } \dot{M}(k) = 0 \int_0^l \left( \frac{a}{\alpha} - \frac{b^2}{\alpha} e^{-\alpha x} \text{erfc } b\sqrt{x} - \frac{b\sqrt{a}}{\alpha} \text{erf } \sqrt{ax} \right) dx. \quad (4.29)$$

The integral in Eq. (4.29) has been evaluated in Appendix C.3 and the result is

$$\begin{aligned} \dot{M}(k) = & \frac{0}{\alpha} \left[ a\tilde{\lambda} + \frac{b^2}{\alpha} e^{-\alpha\tilde{\lambda}} \text{erfc}(b\sqrt{\tilde{\lambda}}) + \frac{b^3}{\alpha\sqrt{a}} \text{erf } \sqrt{a\tilde{\lambda}} - \frac{b^2}{\alpha} - b\sqrt{a} \tilde{\lambda} \text{erf } \sqrt{a\tilde{\lambda}} \right. \\ & \left. - b\sqrt{\frac{\tilde{\lambda}}{\pi}} e^{-\alpha\tilde{\lambda}} + \frac{b}{2\sqrt{a}} \text{erf } \sqrt{a\tilde{\lambda}} \right]. \end{aligned} \quad (4.30)$$

Equation (4.30) gives the instantaneous unsteady mass flow rate along the cavity surface. We now compare this instantaneous mass flow rate relative to  $M_0$ , the mass flow rate obtained in the steady limit. By letting the reduced frequency  $k$  go to zero, we obtain the steady limit for mass flow rate as

$$\dot{M}_o = 4A_T R c_o \left[ \frac{e^{-2R\dot{l}_o}}{2R} \operatorname{erfc} \sqrt{2R\dot{l}_o} + \sqrt{\frac{2\dot{l}_o}{\pi R}} - \frac{1}{2R} \right] . \quad (4.31)$$

We can now write the instantaneous mass flow rate in terms of the quasi-steady mass flow rate as

$$\dot{M} = \dot{M}_o [1 + r(k)e^{j\psi(k)}] , \quad (4.32)$$

where  $\dot{M}_o r(k)$  represents the absolute value of the frequency dependent mass flow rate and  $\psi$  is the phase angle by which the instantaneous mass flow rate leads or lags the steady value.

It is of interest now to look at the relative effects of varying the concentration and cavity length on the unsteady mass flow rate. By a simple sensitivity analysis of the quasi steady mass flow rate (see Appendix D.1) we obtain

$$\frac{\dot{M}}{\dot{M}_o} = \frac{\Delta c_o}{c_o} + \frac{\Delta \dot{l}_o}{2\dot{l}_o} , \quad (4.33)$$

where the  $\Delta$  before a quantity represents a small change in that particular quantity. For the experimental investigation reported in Chapter 3, the

maximum value of  $\frac{\Delta c_o}{c_o}$  is of the order of 5%, whereas the maximum value of

$\frac{\Delta \dot{l}_o}{\dot{l}_o}$  is of the order of 20%. Thus, it is clear that for the experiments reported in Chapter 3, the contribution to gas diffusion across the cavity from changing cavity lengths and changing cavity gas pressure are equally significant.

#### 4.4 Recapitulation

We have developed an analytical model for the prediction of gaseous diffusion across a two-dimensional unsteady cavity surface. This model takes into account the change in cavity length as well as changes in cavity pressure in predicting the gas diffusion across the cavity surface. The expressions for mass flux per unit length and mass diffusion rate across the entire cavity length reduce to those obtained by Parkin (8) when the reduced frequency  $k$  is zero. The instantaneous mass flow rate across the unsteady cavity may be easily obtained from the quasi-steady mass flow rate and the lag function. We reiterate here the general fact that this unsteady gaseous diffusion analysis is valid only for harmonic variations in cavity gas pressure and possibly in cavity length. Nonetheless, this analysis could be extended to encompass a general nonharmonic motion of the cavity by Fourier representation of the cavity length and cavity gas pressure fluctuations, provided that one first accounts for the nonsteady cavity closure conditions to be considered next.

## CHAPTER 5

## A STUDY OF NONSTEADY CAVITY CLOSURE

5.1 Introduction

The analysis of a two-dimensional unsteady cavity of finite extent (i.e., non-zero cavitation number) has been studied among others, by Parkin (28), Wu (5), Guerst (33) and Acosta and Furuya (34). The fact that a cavity volume change in two-dimensional unbounded flow would create infinite pressures puzzled many researchers and was thought to be non-physical at the time. Wu (5) points out the fact that such cavity volume changes in two-dimensional flow are indeed physically plausible and mathematically they represent "inner" flows of some three-dimensional outer flows. Acosta and Furuya (34) rightly exemplify this fact by the existence of unsteady cavities in water tunnel experiments.

The presence of gases in an unsteady cavity flow makes the study of such flows even more interesting and introduces more complexities. Recently, Kato (35) has pointed out the general lack of knowledge that exists in understanding transport phenomena at the cavity surface. The results of the unsteady cavity flow experiments reported in Chapter 3 have clearly shown that the cavity pressure does not remain constant during the oscillation of a finite cavity and indeed even the steady gas pressure of an oscillating cavity depends on the frequency of oscillation! Clearly, the unsteady gas diffusion plays a role in the dynamics of an unsteady cavity.

The idealized closure condition in cavity flow means that at every instant, the cavity-body system is a closed body. Several models have been postulated in the past for the closure of an unsteady cavity. Among them are the kinematically closed model proposed by Tulin (36), the constant volume model proposed by Guerst (33), the fixed cavity terminus model proposed by Leehey (37) and the generalized cavity closure model proposed by Parkin (28). Acosta and Furuya (34) have demonstrated that Parkin's model which involves the evaluation of a difficult retarded integral has the proper quasi-steady limit when the reduced frequency goes to zero. The closure condition postulated by Parkin has been and remains to be difficult to evaluate from first principles of the analysis although Parkin proposed a step-by-step numerical scheme which has never been employed. In the present study, we shall evaluate the phase angle between foil motion and cavity motion by means of a simplified kinematic nonsteady closure condition and then relate the cavity pressure fluctuations and cavity volume fluctuations. Such an analysis should lead to (i) a better understanding of the gaseous entrainment behind nonsteady cavities and (ii) relate observed pressure pulsations to unsteady gaseous entrainment.

### 5.2 Steady Cavity Closure

We first look at the steady cavity closure when there exists a certain amount of gas in addition to water vapor within the cavity. Continuity of mass flux of gas through the cavity dictates in general that the mass flow rate of gases through the cavity must

equal the rate of entrainment behind the cavity plus a possible rate of change of air mass inside the cavity. In the limit of steady flow this last part will vanish. Thus, we can estimate the rate of entrainment of gases behind the cavity by estimating the gas diffusion rate through the cavity surface.

For a flat plate at a small angle of attack  $\alpha_0$ , we can estimate the cavity length  $\bar{l}_0$  at a cavitation number  $\sigma$  (28) as (see Appendix E.1)

$$\bar{l}_0 = \sqrt{\frac{2\alpha_0}{\sigma}} . \quad (5.1)$$

From the steady cavity pressure measurements reported in Chapter 3 (see Figure 3.14), we can approximate the dependence of cavity gas pressure and  $\sigma/\alpha_0$  as

$$\frac{p_G}{p_v} = -0.0976 \frac{\sigma}{\alpha_0} + 0.74 . \quad (5.2)$$

If we denote by  $\alpha_1$ , the amount of dissolved gas in tunnel water, the concentration difference (in ppm) that exists between the free stream and cavity surface may be expressed as

$$c = \alpha_1 - p_G/\beta . \quad (2.9)$$

Thus we observe from Eqs. (5.2) and (2.9) that the concentration difference  $c$  is a function of  $\sigma/\alpha_0$ . We can obtain the mass flux into the cavity from the upper surface as well as the lower surface of the two-dimensional cavity from a modification of Parkin's diffusion model as

$$\dot{M}_o = \frac{4\rho v_t c}{\sqrt{\pi}} [\sqrt{2R} + \sqrt{2\lambda L} - \sqrt{\pi}] , \quad (5.3)$$

where  $v_t$  is the turbulent eddy mass diffusivity and where  $l_0$  represents the cavity length on the upper surface and  $l_1$  represents the cavity length on the lower surface. Figure 5.1 shows the comparison between the gas entrainment rates when the cavity gas pressure is nonzero and for a hypothetical purely vaporous cavity. This fictitious vaporous cavity is used only to bound the diffusion rate. We observe that the entrainment rate decreases with the presence of gases within the cavity as expected. For small values of  $\sigma/\sigma_0$ , the difference in entrainment rate is hardly noticeable because at low values of  $\sigma/\sigma_0$  the mass diffusion rate due to an increase in cavity length is more significant than the decrease in mass flow rate resulting from increased cavity gas pressure.

### 5.3 Nonsteady Cavity Closure, Phase Relations

The difficulties encountered in measuring experimentally the phase angle between the foil motion and cavity motion has been alluded to in Chapter 3. Because of the lack of knowledge that exists in the literature in the determination of the present phase relations, we turn to physically motivated arguments aimed at finding the phase difference between cavity length oscillations and hydrofoil pitching oscillations.

Consider a two-dimensional cavity behind a foil, as shown in Figure 5.2a. The foil has a steady angle of attack  $\alpha_0$ . We suppose that the foil oscillates in pitch about  $B$  with a frequency of  $\omega$  radians per second, the amplitude of oscillation being  $\Delta\alpha$ . The angle of attack  $\alpha(t)$  at any instant is then given by  $\alpha(t) = \alpha_0 + \Delta\alpha \sin \omega t$ . We now approximate the upper surface and lower surface of

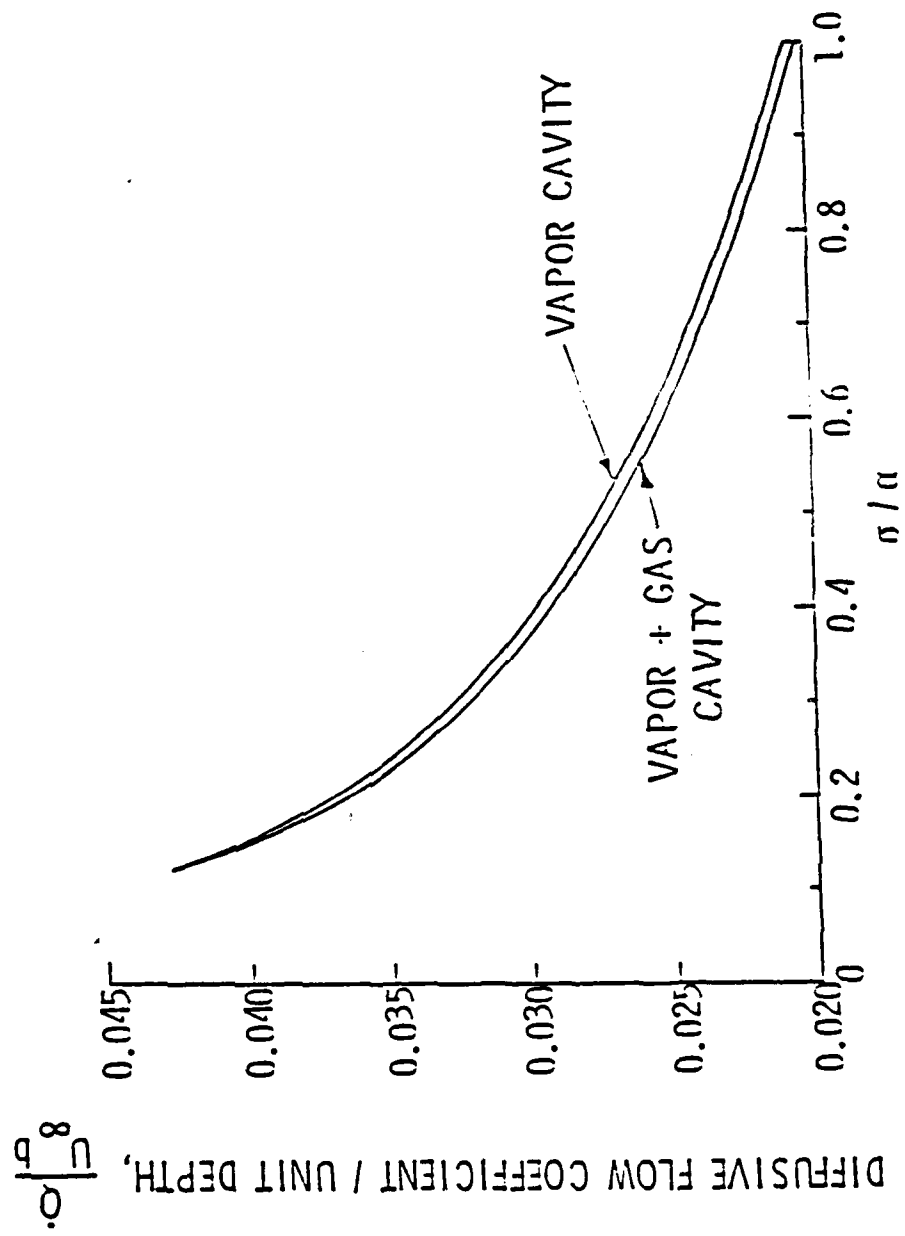
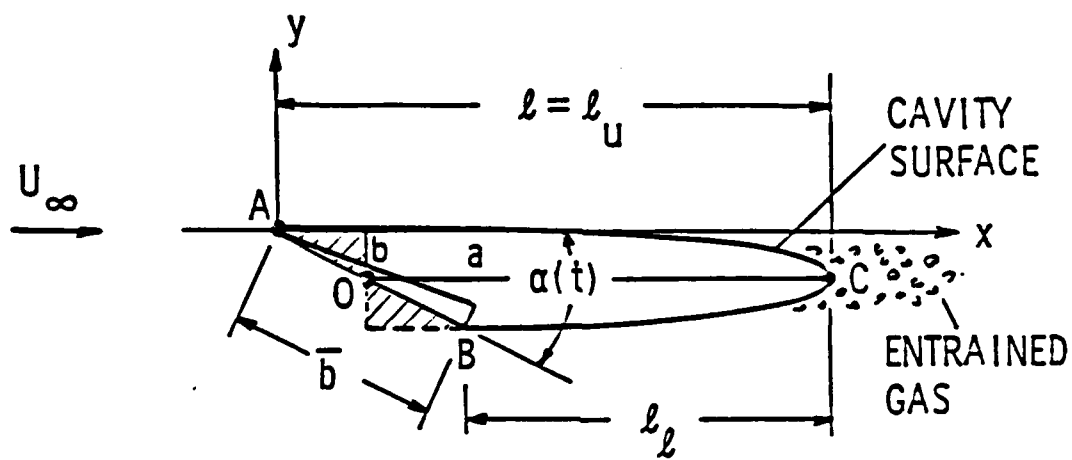
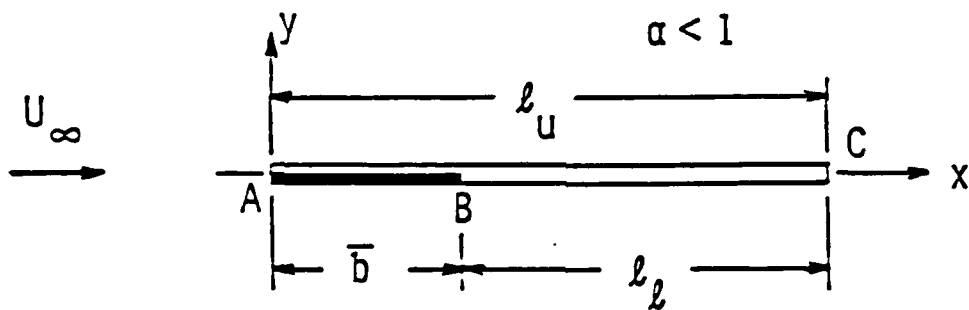


Figure 5.1. Entrainment Rate Behind a Steady Two-Dimensional Cavity.



5.2a Two-Dimensional Cavity Around an Oscillating Hydrofoil



5.2b Physical Plane Representation of Linearized Two-Dimensional Cavity

the cavity by the slits AC and BC respectively as shown in Figure 5.2b. The closure condition of the nonsteady cavity depends on kinematic waves (28), having constant celerity  $q_c$  but different travel distances on the upper and lower surfaces, terminating at a single point C behind the cavity. For kinematic waves originating simultaneously from points A and B to reach C at the same instant, there must exist a phase lag  $\phi$  in the wave originating from the lower surface relative to the wave originating from the upper surface. Since  $\alpha(t)$  is responsible for these waves, we can say that the phase of the cavity terminus oscillation lags that of the driver  $\alpha(t)$ .

If the travel distance on the upper surface is  $l_u$  and the travel time from A to C is  $t_u$ , then  $t_u$  is given by  $t_u/q_c$ . The travel time on the lower surface of distance,  $l_l$ , is given by  $t_l = (l_u - b)/q_c$  if the cavity is closed. But the difference in travel time between the upper and the lower surfaces is  $t_u - t_l = \Delta t = \frac{b}{q_c}$  and then  $\omega \Delta t = \frac{\omega b}{q_c}$ . Therefore the closed-cavity termination phase lag is determined by

$$\omega \Delta t = \phi = \frac{\omega b}{q_c} . \quad (5.4)$$

We now recognize the quantity  $\frac{\omega b}{q_c}$  as the modified reduced frequency  $k'$  and write

$$\phi = k' . \quad (5.5)$$

Thus we observe, within the limitations of the present assumptions that if the kinematic waves (28) from the upper surface and lower surface terminate at one point at the same instant, the phase angle equals the modified reduced frequency. This result conforms with the

qualitative visual observations made during the experimental investigation viz., at low frequencies there is hardly any phase difference discernible whereas at higher frequencies, there seems to be a noticeable phase difference between the foil motion and cavity motion.

We note in passing, that this simple analysis is consistent with the linearized approach of Parkin (28), but we have used the preceding physical argument in order to avoid the nasty retarded closure integral introduced in (28). If we were to relax this consistency, we would replace the factor  $\bar{b}$  by  $\bar{b} \cos \alpha_0$ , from which we would have the phase angle as  $k' \cos \alpha_0$  instead of  $k'$ . As to be expected, in the limit, for small oscillations of a vertical plate there would be little or no phase difference between the upper and lower surfaces of the cavity.

An additional aspect of the present approximate argument is that the value of  $\Delta t$  is independent of the fundamental frequency of the foil oscillation, the important factor being the constant value of  $q_c$ . Because of this fact this same phase lag,  $\phi$ , between profile and cavity terminus oscillations must apply to the higher harmonics of the cavity length fluctuations as reported in Figure 3.8 above and as also suggested by Eq. (3.3). This means that this phase lag angle depends on the basic foil oscillation. Cavity oscillation overtones of  $2\omega$  and  $3\omega$ , etc., would not have phase lags of  $2\phi$ ,  $3\phi$ , etc., as might be supposed at first glance.

#### 5.4 Nonsteady Cavity Closure, Entrainment Rates

If the cavity ordinate at any instant is  $n(x,t)$ , then the cavity closure condition is expressed as (28),

$$\int_{\text{body}} d\eta = 0 \quad (\text{t fixed}) \quad . \quad (5.6)$$

Now, we shall assume that the cavity behind a flat plate of chord length  $\bar{b}$ , at an angle of attack  $\alpha(t)$ , at any instant  $t$ , may be approximated by a part of an ellipse fitted to the cavity termination point,  $\ell(t)$ , and to the leading edge and trailing edge separation points, see Figure 5.2a. We also assume that the length of the cavity  $\ell(t)$  is measured from the nose of the flat plate as shown. Then, we take the equation of the ellipse to be

$$\frac{(x - h)^2}{a^2} + \frac{(y - k)^2}{b^2} = 1, \quad (5.7)$$

where  $(h, k)$  represents the center of the ellipse and the quantities  $a$  and  $b$  represent the semi-major axis and the semi-minor axis of the ellipse respectively. At any instant, the ellipse will pass through the points  $(0,0)$ ,  $(\ell, -\frac{\bar{b}}{2} \sin \alpha)$  and  $(\bar{b} \cos \alpha, -\bar{b} \sin \alpha)$ . These three conditions lead to

$$\frac{h^2}{a^2} + \frac{k^2}{b^2} = 1, \quad (5.8a)$$

$$\frac{(\ell - h)^2}{a^2} + \frac{(\frac{\bar{b}}{2} \sin \alpha + k)^2}{b^2} = 1, \quad (5.8b)$$

and

$$\frac{(\bar{b} \cos \alpha - h)^2}{a^2} + \frac{(\bar{b} \sin \alpha + k)^2}{b^2} = 1. \quad (5.8c)$$

For small values of the angle of attack  $\alpha$ , we can write from Equations 5.8a, b and c,

$$k = -\frac{\alpha}{2} \bar{b} , \quad (5.9)$$

$$h = \frac{\bar{b}}{2} , \quad (5.10)$$

$$a = \frac{\bar{b}}{2} (1 + 4\bar{l}(\bar{l}-1))^{1/2} , \quad (5.11)$$

and  $b = \frac{\alpha \bar{b}}{4} \left( \frac{1 + 4\bar{l}(\bar{l}-1)}{\bar{l}(\bar{l}-1)} \right)^{1/2} . \quad (5.12)$

It should be noted that the cavity length appearing in Eqs. (5.11) and (5.12) is dimensionless,  $(\bar{l}/\bar{b})$ . From Eqs. (5.9) and (5.10) it is clear that for small angles of attack, the center of the elliptical cavity is fixed to the center of the foil. From Fig. 5.2a it is apparent that the cavity volume  $V$  per unit depth is then simply the area of the semi ellipse

$$V = \frac{\pi \alpha \bar{b}^2}{2} \bar{l} \left( 1 - \frac{1}{2\bar{l}} \right) , \quad (5.13a)$$

where  $\alpha = \alpha_0 (1 + \Delta\alpha e^{j\omega t}) ,$

and  $\bar{l} = \bar{l}_0 (1 + \epsilon e^{j\omega t} e^{j\phi}) .$

Equation (5.13a) can be written as

$$V = \frac{\pi \alpha_0 \bar{b}^2}{2} \left( \bar{l}_0 - \frac{1}{2} \right) \left[ 1 + \frac{(\epsilon e^{j\phi} + \Delta\alpha - \Delta\alpha/2\bar{l}_0) e^{j\omega t}}{(1 - 1/2\bar{l}_0)} \right] . \quad (5.13b)$$

The steady cavity volume  $V_0$  from Eq. (5.13b) is

$$V_0 = \frac{\pi a_0^2 b^2}{2} \left( \tilde{l}_0 - \frac{1}{2} \right) , \quad (5.13c)$$

so that the cavity volume  $V$  at any instant can be written as

$$V = V_0 (1 + v e^{j\omega t}) , \quad (5.14)$$

where

$$v = \left( \epsilon e^{j\phi} + \Delta \alpha - \frac{\Delta \alpha}{2 \tilde{l}_0} \right) / \left( 1 - \frac{1}{2 \tilde{l}_0} \right) . \quad (5.15)$$

We now look at the conservation of mass flux of gas through the control volume consisting of the cavity surface, the gas within the cavity and the mass entrained from the cavity terminus. Let  $m$  be the total mass of gas within the cavity at any instant,  $\dot{M}_d$  be the mass flux of gas diffusing into the cavity through its surface and  $\dot{E}$  be the mass flux of gas entrained out of the cavity through the cavity end. Then we can write the continuity of mass as

$$\dot{M}_d = \frac{\partial m}{\partial t} + \dot{E} . \quad (5.16a)$$

Let  $\dot{M}_{d_0}$  represent the steady gaseous diffusion rate across the entire cavity surface. Then, from Eq. (5.16a), the gaseous mass entrainment rate  $\dot{E}$  relative to the steady gaseous mass entrainment rate  $\dot{M}_{d_0}$  is given by

$$\frac{\dot{E}}{\dot{M}_{d_o}} = \frac{\dot{M}_d}{\dot{M}_{d_o}} - \frac{1}{\dot{M}_{d_o}} \frac{\partial m}{\partial t} . \quad (5.16b)$$

By using a quasisteady approach, the incremental mass diffusion rate due to cavity pressure changes and cavity length changes may be written from Eq. (5.3) as,

$$\frac{\Delta \dot{M}_d}{\dot{M}_{d_o}} = \frac{\Delta c_o}{c_o} + \frac{\epsilon}{\sqrt{2 \bar{l}_{u_o} \bar{l}_{l_o}}} , \quad (5.17)$$

where  $\bar{l}_{u_o}$  and  $\bar{l}_{l_o}$  represent the steady dimensionless cavity lengths on the upper surface and lower surface respectively. The

quantity  $\frac{\Delta c_o}{c_o}$  has been evaluated in Appendix E.2 in terms of  $\sigma/\alpha_o$  and  $\Delta\alpha_o/\alpha_o$  and the result is

$$\frac{\Delta c_o}{c_o} = \frac{-0.0976 (\sigma/\alpha_o)(\Delta\alpha_o/\alpha_o)(p_v/\beta)}{\alpha_1 - \frac{p_v}{\beta} (0.74 - 0.0976 \frac{\sigma}{\alpha_o})} . \quad (5.18)$$

Assuming that the gas within the cavity behaves isothermally, one may use the equation of state (see Appendix E.3) to obtain for  $\partial m/\partial t$ ,

$$\frac{\partial m}{\partial t} = \frac{\pi \alpha_o \bar{b} p_{G_o} k' q_c j}{2RT} [(\bar{l}_{u_o} - \frac{1}{2})(\Delta\alpha + \delta e^{j\phi_a}) + \bar{l}_{u_o} \epsilon e^{j\phi}] , \quad (5.19)$$

where  $R$  = specific gas constant ( $=1718 \text{ ft.lb./slug } ^\circ\text{R}$ ),

$\phi_a$  = phase angle between cavity pressure fluctuation and foil oscillation,

$T$  = absolute temperature of the gas within the cavity.

From Eq. (5.3) the steady gaseous diffusion rate is given by

$$\dot{M}_{d_0} = \frac{4\rho v_t c}{\sqrt{\pi}} \left[ \sqrt{2R} \bar{i}_{u_0} + \sqrt{2R} \bar{i}_{l_0} \right], \quad (5.20)$$

where  $R$  in Eq. (5.20) is the diffusive Reynolds' number,

$R = U_\infty \bar{b} / 2v_t$ . Eqs. (5.17) through (5.20) may now be substituted in

Eq. (5.16b) to obtain the total entrainment rate  $\dot{E}/\dot{M}_{d_0}$  as

$$\frac{\dot{E}}{\dot{M}_{d_0}} = 1 - \frac{0.0976 \left( \frac{\sigma}{\sigma_0} \right) \left( \frac{\Delta\alpha}{\alpha_0} \right) \left( \frac{p_v}{\beta} \right)}{\alpha_1 - \frac{p_v}{\beta} (0.74 - 0.0976 \frac{\sigma}{\sigma_0})} + \frac{\epsilon}{2 \sqrt{\bar{i}_{u_0} \bar{i}_{l_0}}} - \frac{\frac{\pi \alpha_0 \bar{b} p_{G_0} k' q_c j}{2RT \dot{M}_{d_0}} \left[ (\bar{i}_{u_0} - 0.5) (\Delta\alpha + \delta e^{j\phi_a}) + \bar{i}_{u_0} \epsilon e^{j\phi} \right]}{[(\bar{i}_{u_0} - 0.5) (\Delta\alpha + \delta e^{j\phi_a}) + \bar{i}_{u_0} \epsilon e^{j\phi}]} . \quad (5.21)$$

A polar plot of the total entrainment rate for four different reduced frequencies is shown in Figure 5.3. The experimental data points from Figure 3.8 and 3.14 on cavity length amplitudes and a quasisteady gas pressure amplitude based on the linear regression of Figure 3.14 have been used in obtaining these calculated data points. (See Appendix E.3 and E.4 for sample calculations and tabulated results). It must be noted that the unsteady entrainment rate amplitudes in Figure 5.3 are root mean square values and that the calculated data points in Figure 5.3 refer to a single value of  $\sigma/\sigma_0$ . [For different values of  $\sigma/\sigma_0$ , one might naturally expect to obtain a family of curves similar to Figure 5.3].

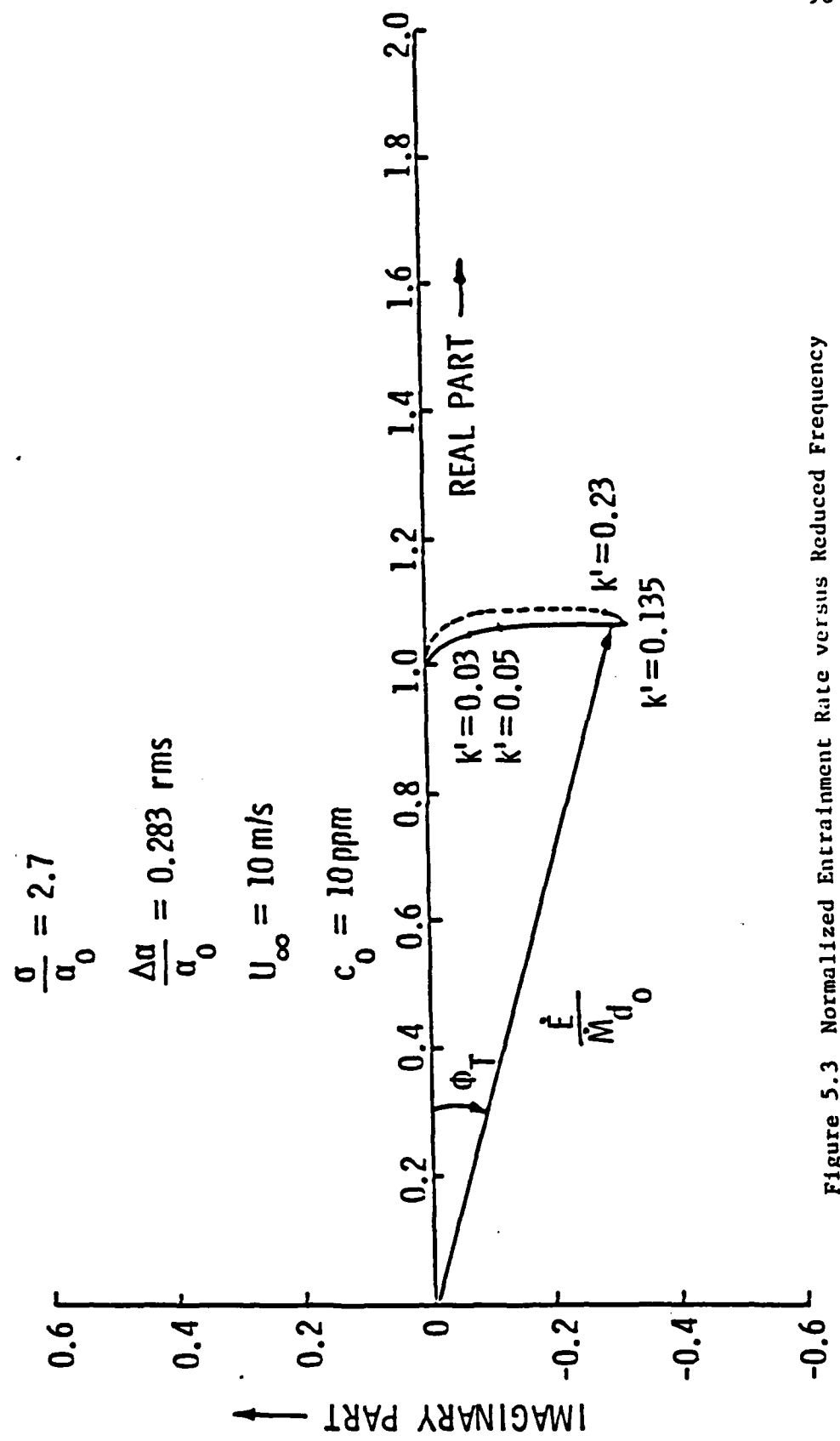


Figure 5.3 Normalized Entrainment Rate versus Reduced Frequency

It is observed from Figure 5.3 that the total entrainment rate at any oscillation frequency always lags the foil motion. The maximum phase angle  $\phi_T$ , is seen to be about 20 degrees. For large values of  $k'$ , the amplitude of the nonsteady entrainment rate tends to decrease rapidly, as shown by the dotted line in Figure 5.3, with the limiting value of zero for very high frequencies. At least, the present experimental data for reduced frequencies  $k'$  up to  $k' = 1.0$  would seem to indicate such a trend. The rapid decrease in cavity length amplitude at reduced frequencies  $k'$  higher than 0.23 in conjunction with the time resolution available from the video-tape records used for measuring cavity lengths made it impossible to obtain cavity length amplitudes for frequencies higher than  $k' = 0.23$ . It is of interest here to observe that the nonsteady entrainment rate lags the foil oscillation by nearly  $90^\circ$  at all frequencies. It appears that as the cavity is increasing in volume, the cavity is able to sustain higher cavity pressures and thus lower entrainment results behind the cavity. The uncertainty involved in obtaining data points in Figure 5.3 is difficult to predict, given the many variables and assumptions involved in the calculations. However, the trend predicted by the semi-empirical model is interesting and should serve as a guide for future research in this area.

### 5.5 Recapitulation

In this chapter, the two-dimensional gaseous cavity closure in steady as well as nonsteady cavity flow is analyzed. It is observed that the presence of gases within the cavity alters the gas entrainment rate behind the cavity. The change in steady gas

entrainment, however, is seen to be insignificant as the ratio  $\sigma/\alpha$  decreases. By imposing the fact that the surface of a nonsteady cavity is essentially a material surface at every instant and assuming that the surface waves from the upper surface and lower surface of the cavity terminate at one point behind the cavity at every instant, the phase relation between the foil motion and cavity motion is obtained. This phase relation is seen to be consistent with the experimental observations. The nonsteady gaseous entrainment behind the cavity is estimated using the nonsteady continuity equation, with the assumption that the gas within the cavity undergoes isothermal compression and expansion. The nonsteady gaseous entrainment is seen to depend primarily on the cavity volume fluctuations and cavity gas pressure fluctuations because it is found that for the range of reduced frequencies considered here the diffusion into the cavity is quasi-steady. It is also seen that the nonsteady entrainment rate always lags the foil oscillation.

## CHAPTER 6

### CONCLUSIONS AND RECOMMENDATIONS

It has been the aim of this thesis to address and resolve some of the aspects involving gaseous diffusion in steady and unsteady cavity flows so that the phenomenon of gaseous entrainment behind a cavity may be better understood and an improved representation for the influence of the nonsteady cavity in a water tunnel test section can be obtained.

We have demonstrated very clearly that existing mathematical models for gaseous diffusion across axisymmetric cavity surfaces are inadequate. While the exact solution of the three coupled integral equations formulated in Chapter 2 might result in a more accurate representation of the gas diffusion phenomenon across axisymmetric cavity surfaces than has been possible until now, it seems likely that a more realistic model of the important physics would be more fruitful. Even so, the highly simplified approach used with the best experimental results available from the literature appears to give satisfactory estimates of diffusive mass flows into the cavity from the free stream.

As noted above, a plausible alternative for the solution of the axisymmetric diffusion problem is by a two-layer diffusion model. Such an asymptotic solution of the problem will represent a more realistic physical model of the phenomena which could account for molecular gaseous diffusion from the free stream into the turbulent concentration layer and turbulent diffusion from the turbulent momentum layer into the cavity.

From the experimental results obtained at upstream and downstream locations with respect to the unsteady cavities, we have been able to identify and quantify the unsteady cavity as a dynamic element. The cavity behind an oscillating foil has been characterized as a dipole source at low frequencies of oscillation. Unsteady cavity length measurements have shown that for sinusoidal oscillations of the body, higher harmonics of the cavity oscillations are important to be considered, especially the first two harmonics are seen to be significant. Steady cavity pressures are generally seen to be much higher than the vapor pressure.

Further experiments are definitely warranted, perhaps in a larger water tunnel, to extend the range and scope of the present experimental investigation. The measurement of phase difference between body motion and cavity motion for several reduced frequencies would be most helpful in modeling unsteady cavity closure. Even so, the unsteady gas diffusion analysis presented in Chapter 4 in conjunction with the experimental results has enabled a more realistic cavity closure model to be developed than has been possible heretofore.

The steady cavity closure for gaseous cavities has shown that the presence of noncondensable gas in the cavity does affect the steady entrainment rate of gases at the cavity terminus. The formulation of nonsteady gaseous cavity closure involves the determination of phase angles between the foil motion and i) nonsteady gas diffusion through the cavity surface, ii) the cavity volume fluctuations, and iii) cavity pressure fluctuations, respectively. By a simple cavity terminus closure model, we have

been able to estimate the phase difference that could exist between the foil motion and the cavity length motion. The many variables involved in estimating the nonsteady entrainment rate clearly suggests the need for more refined experimentation and theory to understand more fully nonsteady gaseous cavities and the related turbulent entrainment rates.

## BIBLIOGRAPHY

1. Prevention of Coupled Structure-Propulsion Instability (POGO),  
NASA SP-3055 (October 1970).
2. Rubin, S., "Longitudinal Instability of Liquid Rockets due  
to Propulsion Feed Back (POGO)," *J. Spacecraft and Rockets*  
3(8) (1966).
3. Klose, G. J. and A. J. Acosta, "Unsteady Force Measurements  
on Superventilating Hydrofoils in Heaving Motion, *J. Ship*  
*Research* 13(1) (1969).
4. Shen, Y. T. and F. B. Peterson, "Unsteady Cavitation on an  
Oscillating Hydrofoil," 12th Symposium on Naval Hydrodynamics,  
Washington, DC (June 1978).
5. Wu, Y. T., "Cavity and Wake Flows," *Ann. Rev. of Fluid Mech.*  
4:243-284 (1972).
6. Gadd, G. E. and S. Grant, "Some Experiments on Cavities  
behind Disks," *J. Fluid Mech.* 23(4) (1965).
7. Epstein, P. S. and M. S. Plesset, "On the Stability of Gas  
Bubbles in Liquid-Gas Solutions," *J. Chemical Physics*  
18:1505-1509 (1950).
8. Parkin, B. R. and R. W. Kermeen, "The Roles of Convective  
Air Diffusion and Tensile Stresses during Cavitation  
Inception," Proceedings of IAHR Symposium on Cavitation  
and Hydraulic Machinery, Sendai, Japan (1963).
9. Brennen, C., "The Dynamic Balances of Dissolved Air and  
Heat in Natural Cavity Flows," *J. Fluid Mech.* 37(1):115-127  
(1969).

10. Swanson, W. M. and J. P. O'Neill, "The Stability of an Air Maintained Cavity behind a Stationary Object in Flowing Water," Report No. M24.3, Hydrodynamics Laboratory, California Institute of Technology (5 September 1951).
11. Cox, R. N. and W. A. Clayden, "Air Entrainment at the Rear of a Steady State Cavity," Report No. 12, Cavitation in Hydrodynamics, Proceedings of a Symposium held at NPL (14-17 September 1955).
12. Reichardt, H., "The Laws of Cavitation Bubbles at Axially Symmetrical Bodies in a Flow," Report No. 776, MAP Reports and Transactions (15 August 1956).
13. Billet, M. L. and D. S. Weir, "The Effect of Gas Diffusion on the Flow Coefficient for a Ventilated Cavity," J. Fluids Engr. 97:501-506 (1975).
14. Song, C. S., "Pulsation of Ventilated Cavities," Technical Paper No. 32, Serial B., St. Anthony Falls Hydraulic Laboratory, The University of Minnesota (February 1961).
15. Silberman, E. and C. S. Long, "Instabilities of Ventilated Cavities," Technical Paper No. 29, Serial B, St. Anthony Falls Hydraulic Laboratory, The University of Minnesota (September 1977).
16. Huse, E., "Effect of Cavitation on Propeller-Induced Vibratory Forces," Proceedings of the 14th ITTC, Vol. 4, Ottawa, Canada (September 1975).

17. Jiang, C. W. and P. Leehey, "Experimental and Theoretical Investigation of Unsteady Supercavitating Hydrofoils of Unit Span," Report No. 83481-4, Massachusetts Institute of Technology (September 1977).
18. Brennen, C. and A. J. Acosta, "The Dynamic Transfer Function for a Cavitating Inducer," *J. Fluids Engr.* 98 (1976).
19. Hord, J., "Cavitation in Liquid Cryogens. III. Ogives," *NASA CR-2242* (1973).
20. Greitzer, J., "The Stability of Pumping Systems," *J. Fluids Engr.* 103(2) (June 1981).
21. Catalogue of Facilities, Information Committee of the 16th ITTC.
22. Bobber, R. J., "Underwater Electro-Acoustic Measurements," *Naval Research Laboratory, Washington, DC* (1970).
23. Fernandez, J., "A Higher Order Surface Singularity Method for the Axisymmetric Inverse Problem," *ARL/PSU TM 79-125, Applied Research Laboratory, The Pennsylvania State University* (1979).
24. Hsu, C. C., "On Wall Effects in Cavity Flows," *J. Ship Research* 28(1):70-75 (March 1984).
25. Van Houten, R. J., "The Transient Cavitation of a Two Dimensional Hydrofoil-Comparison of Theory and Experiment," *MIT Ocean Engineering Report* (August 1979).

26. Ross, D., Underwater Noise, Pergamon Press (1976).
27. Billet, M. L. and D. E. Thompson, "Blade Surface Cavitation Noise," Joint Symposium on Design and Operation of Fluid Turbomachinery, ASCE/LAHR/ASME, Vol. II (1978).
28. Parkin, B. R., "Fully Cavitating Hydrofoils in Nonsteady Motion," Report No. RM-1939, RAND Corporation (July 1957).
29. Schlichting, H., Boundary Layer Theory, McGraw Hill, p. 753 (1979).
30. Sherwood, T. K. and R. L. Pigford, Absorption and Extraction, Second Edition, McGraw Hill Chemical Engineering Series, pp. 39-41 (1952).
31. Batchelor, G. H., An Introduction to Fluid Dynamics, Cambridge University Press, p. 33 (1981).
32. Goldstein, S. (editor), Modern Developments in Fluid Dynamics, Vol. 2, Dover Publications, p. 647 (1961).
33. Guerst, J. A., "Linearized Theory for Two-Dimensional Cavity Flows," Thesis, Technische Hogeschool, Delft, The Netherlands (1961).
34. Acosta, A. J. and O. Furuya, "A Brief Note on Linearized Unsteady, Supercavitating Flows," J. Ship Research 23(2) (1979).
35. Kato, H., "On the Structure of Cavity -- New Insight into the Cavity Flow: A Summary of the Keynote Speech," International Symposium on Jets and Cavities, FED Vol. 31 (November 1985).

36. Tulin, M. P., "Steady Two-Dimensional Cavity Flows about Slender Bodies," David W. Taylor Model Basin Report 834, Washington, DC (1953).
37. Leehey, P., "Boundary Conditions for Unsteady Supercavitating Flows," Proceedings of the 4th ONR Symposium on Naval Hydrodynamics (1962).

## APPENDIX A

## DETAILS OF AXISYMMETRIC DIFFUSION ANALYSIS

### A.1 Asymptotic Evaluation of Integral in Equation 2.10

The integral in Eq. (2.10) is

$$I = \int_0^{2\pi} \frac{e^{-\lambda \sqrt{m^2 - 2rcos\theta}}}{\sqrt{m^2 - 2rcos\theta}} d\theta , \quad (A.1.1)$$

where

$$m^2 = (x - \xi)^2 + r^2 + 1 . \quad (A.1.2)$$

(We recall here that the distances  $r$ ,  $x$  and  $\xi$  are non-dimensionalized with respect to the radius of the cavity and  $\lambda = U_\infty a/2k$  is a large number of the order 1000.)

We use Laplace's method (see, for example, Nayfeh, A. H., Introduction to Perturbation Techniques, John Wiley, 1981, p. 88) to evaluate the integral in Eq. (A.1.1).

Letting

$$f(\theta) = \frac{1}{\sqrt{m^2 - 2rcos\theta}} , \quad (A.1.3)$$

and

$$h(\theta) = -\sqrt{m^2 - 2rcos\theta} . \quad (A.1.4)$$

The integral in Eq. (A.1.1) may be written as

$$I = \int_0^{2\pi} f(\theta) e^{\lambda h(\theta)} d\theta . \quad (A.1.5)$$

We will now expand  $h(\theta)$  and  $f(\theta)$  in Taylor's series.

$$\frac{dh}{d\theta} = -\frac{rsin\theta}{\sqrt{m^2 - 2rcos\theta}} \text{ so that } \frac{dh}{d\theta} \Big|_{\theta=0} = 0 .$$

Also,

$$\frac{d^2h}{d\theta^2} = \frac{-(m^2 - 2rcos\theta)rcos\theta + r^2sin^2\theta}{(m^2 - 2rcos\theta)^{3/2}}$$

and

$$\frac{d^2h}{d\theta^2} \Big|_{\theta=0} = -\frac{r}{(m^2 - 2r)^{1/2}} , \text{ a negative quantity .}$$

Hence, the function  $h(\theta)$  has an absolute maximum value at  $\theta = 0$  and it may now be expanded in a Taylor's series about  $\theta = 0$ :

$$h(\theta) = h(0) + h'(0)\theta + \frac{1}{2} h''(0)\theta^2 + \dots$$

i.e.,

$$h(\theta) = -\sqrt{m^2 - 2r} - \frac{1}{2} \frac{r\theta^2}{\sqrt{m^2 - 2r}} + \dots . \quad (\text{A.1.6})$$

For the function  $f(\theta)$ ,

$$f(\theta) = \frac{1}{\sqrt{m^2 - 2rcos\theta}} \text{ so that } f(0) = \frac{1}{\sqrt{m^2 - 2r}}$$

$$\frac{df}{d\theta} = -\frac{rsin\theta}{(m^2 - 2rcos\theta)^{3/2}} \text{ so that } \frac{df}{d\theta} \Big|_{\theta=0} = 0$$

$$\frac{d^2 \xi}{d\theta^2} = \frac{3r^2 \sin^2 \theta - r \sin \theta (m^2 - 2r \cos \theta)}{(m^2 - 2r \cos \theta)^{5/2}}$$

$$\text{so that } \frac{d^2 \xi}{d\theta^2} \Big|_{\theta=0} = - \frac{r}{(m^2 - 2r)^{3/2}} .$$

Hence the function  $f(\theta)$  also has an absolute maximum value at  $\theta = 0$ .  $f(\theta)$  may now be expanded in a Taylor's series,

$$f(\theta) = \frac{1}{\sqrt{m^2 - 2r}} - \frac{r\theta^2}{2(m^2 - 2r)^{3/2}} + \dots \quad (A.1.7)$$

Substituting the series expansion for  $f(\theta)$  and  $h(\theta)$  in Eq. (A.1.5), we have

$$I = \int_0^\infty \left[ (m^2 - 2r)^{-1/2} - \frac{r\theta^2}{2} (m^2 - 2r)^{-3/2} + \dots \right] \frac{-\lambda \left[ (m^2 - 2r)^{1/2} + \frac{r\theta^2}{2 \sqrt{m^2 - 2r}} + \dots \right]}{d\theta} . \quad (A.1.8)$$

In Eq. (A.1.8), the limit  $\infty$  instead of  $2\pi$  appears because the absolute maximum value of the function  $h(\theta)$  occurs at  $\theta = 0$  and hence the maximum contribution to the integral results from the region in the neighborhood of  $\theta = 0$ . Equation (A.1.8) may be rearranged as

$$I = \frac{e^{-\lambda} \sqrt{m^2 - 2x}}{\sqrt{m^2 - 2x}} \int_0^{\sqrt{m^2 - 2x}} \exp(-\lambda r \theta^2/2 \sqrt{m^2 - 2x}) d\theta$$

$$= - \frac{r e^{-\lambda} \frac{m^2 - 2x}{2(m^2 - 2x)^{3/2}}}{2(m^2 - 2x)^{3/2}} \int_0^{\sqrt{m^2 - 2x}} \theta^2 \exp(-\lambda r \theta^2/2 \sqrt{m^2 - 2x}) d\theta .$$

(A.1.9)

The integrals in Eq. (A.1.9) may be evaluated (see, for example, Gradshteyn and Ryzhik, Table of Integrals, Series and Products, Academic Press, 1979) and the result is

$$I = \sqrt{\frac{\pi}{2\lambda r}} e^{-\lambda} \sqrt{m^2 - 2x} \left[ \frac{1}{(m^2 - 2x)^{1/4}} - \frac{1}{\lambda} \frac{1}{(m^2 - 2x)^{3/4}} + \dots \right] .$$

(A.1.10)

For large values of  $\lambda$ , we can neglect all but the first term in Eq. (A.1.10) and obtain

$$I \approx \sqrt{\frac{\pi}{2\lambda r}} \frac{e^{-\lambda} \sqrt{m^2 - 2x}}{(m^2 - 2x)^{1/4}} . \quad (A.1.11)$$

Substituting for  $m$  from Eq. (A.1.2), we have

$$I \approx \sqrt{\frac{\pi}{2\lambda r}} \frac{e^{-\lambda} \sqrt{(x - \xi)^2 + (r - 1)^2}}{[(x - \xi)^2 + (r - 1)^2]^{1/4}} . \quad (A.1.12)$$

### A.2 Simplification of Integral Equations

Simplification of Eqs. (2.21), (2.22) and (2.23): Consider Eq. (2.21). The third integral on the right-hand side of Eq. (2.21) is

$$\int_{x_2}^{\infty} \frac{f_2(\xi)e^{-2\lambda(\xi - x_2)}}{\sqrt{\xi - x_2}} d\xi .$$

Recognizing the fact that  $\lambda$  is a large number, the strong negative exponential causes the function  $f_2$  to be a slowly varying function and thus  $f_2$  may be assumed to contribute to the integral only near  $\xi = x_2$ . Thus,

$$\int_{x_2}^{\infty} \frac{f_2(\xi)e^{-2\lambda(\xi - x_2)}}{\sqrt{\xi - x_2}} d\xi = f_2(x_2) \int_{x_2}^{\infty} \frac{e^{-2\lambda(\xi - x_2)}}{\sqrt{\xi - x_2}} d\xi .$$

The upper limit  $\infty$  may be replaced by  $\infty$  and the integral evaluated to get  $f_2(x_2) \sqrt{\frac{\pi}{2\lambda}}$ . The very same arguments lead to the simplification of second integral of Eq. (2.22) and fourth integral of Eq. (2.23).

Similarly, the fourth integral on the right-hand side of Eq. (2.21) is

$$\text{Integral} = \int_{x_2}^{\infty} \frac{f_3 e^{-2\lambda(\xi - x_2)}}{\sqrt{\xi - x_2}} d\xi .$$

Letting  $\xi - x_2 = m$ , we have

$$\text{Integral} = \int_{2-x_2}^{\infty} \frac{f_3 e^{-2\lambda m}}{\sqrt{m}} dm .$$

Once again because of the strong negative exponential, we may write,

$$\text{Integral} = f_3 (2 - x_2) \left[ \int_0^{\infty} \frac{e^{-2\lambda m}}{\sqrt{m}} dm - \int_0^{2-x_2} \frac{e^{-2\lambda m}}{\sqrt{m}} dm \right] ,$$

$$\text{Integral} = f_3 (2 - x_2) \text{erfc} \sqrt{2\lambda(2 - x_2)} .$$

We now note that  $f_3$  is defined only in the interval  $2 < \xi < \infty$ .

Thus, the fourth integral on the right-hand side of Eq. (2.21) is zero. The fourth integral on the right-hand side of Eq. (2.22) is

$$\text{Integral} = \int_2^{\infty} \frac{f_3 e^{-2\lambda(\xi - x_1)}}{\sqrt{\xi - x_1}} d\xi , \quad x_1 < 0 .$$

By letting  $\xi - x_1 = m$ , we have

$$\text{Integral} = \int_{2-x_1}^{\infty} \frac{f_3 e^{-2\lambda m}}{\sqrt{m}} dm .$$

Once again, because of the strong negative exponential in the integrand, we may write,

$$\text{Integral} = f_3(l - x_1) \left[ \int_0^{2-x} \frac{e^{-2\lambda m}}{\sqrt{m}} dm - \int_0^1 \frac{e^{-2\lambda m}}{\sqrt{m}} dm \right] ,$$

$$\text{Integral} = f_3(l - x_1) \operatorname{erfc} \sqrt{2\lambda(2 - x_1)} .$$

Recalling the fact that  $x_1$  is negative, the integral is  $\approx 0$ .

A.3 Solution of Eq. (2.22a)

Equation (2.22a) is

$$\int_{-\infty}^{x_1} \frac{f_1}{\sqrt{x_1 - \xi}} d\xi + f_1(x_1) \sqrt{\frac{\tau}{2\lambda}} = 0 \quad . \quad (A.3.1)$$

We rewrite Eq. (A.3.1) as

$$f_1(x_1) + k \int_{-\infty}^{x_1} \frac{f_1(\xi)}{\sqrt{x_1 - \xi}} d\xi = 0 \quad , \quad (A.3.2)$$

where

$$k = \sqrt{\frac{2\lambda}{\pi}} \quad . \quad (A.3.3)$$

We shall use Picard's method with

$$f_{1,0}(x) = c_1 e^{px_1} \quad , \quad (A.3.4)$$

where  $p$  and  $c_1$  are unknown constants. Then substituting Eq. (A.3.4) in Eq. (A.3.2),

$$f_{1,1}(x_1) = -kc_1 \int_{-\infty}^{x_1} \frac{e^{p\xi}}{\sqrt{x_1 - \xi}} d\xi \quad . \quad (A.3.5)$$

If we now let  $t = x_1 - \xi$ , we have

$$f_{1,1}(x_1) = -kc_1 e^{px_1} \int_0^{\infty} \frac{e^{-pt}}{\sqrt{t}} dt \quad .$$

i.e.,

$$f_{1,1}(x_1) = -kc_1 e^{px_1} \sqrt{\frac{1}{p}} . \quad (A.3.6)$$

We note that  $f_{1,1}(x_1)$  is not very different from  $f_{1,0}(x_1)$ . Hence we choose  $p$  such that  $f_{1,0}(x_1) = f_{1,1}(x_1)$ . Thus we obtain

$$e^{px}(1 \pm k \sqrt{\frac{1}{p}}) = 0 .$$

Taking the negative square root\* so  $p$  is real, we get

$$1 - k \sqrt{\frac{1}{p}} = 0$$

or

$$p = \pi k^2 . \quad (A.3.7)$$

Thus

$$f_1(x_1) = c_1 e^{\pi k^2 x_1} , \quad x_1 < 0 . \quad (A.3.8)$$

---

\*This is required for the function  $f_1(x_1)$  to satisfy the integral equation.

A.4 Solution of Eq. (2.21a)

Equation (2.21a) is

$$\frac{c_0}{A} = \int_{-\infty}^0 \frac{f_1}{\sqrt{x_2 - \xi}} d\xi + \int_0^{x_2} \frac{f_2}{\sqrt{x_2 - \xi}} d\xi + \sqrt{\frac{\pi}{2\lambda}} f_2 . \quad (A.4.1)$$

Substituting the value of  $f_1$  from Eq. (2.24), we have

$$\frac{c_0}{A} = \int_{-\infty}^0 \frac{c_1 e^{2\lambda\xi}}{\sqrt{x_2 - \xi}} d\xi + \int_0^{x_2} \frac{f_2}{\sqrt{x_2 - \xi}} d\xi + \sqrt{\frac{\pi}{2\lambda}} f_2 . \quad (A.4.2)$$

Consistent with our approximations in the first integral appearing on the right hand side of Eq. (A.4.2), we shall assume that the strong negative exponential will cause  $\frac{1}{\sqrt{x_2 - \xi}}$  to vary slowly so that it can be assumed to contribute to the result only near  $\xi = 0$ .

Thus,

$$\frac{c_0}{A} = \frac{c_1}{2\lambda} \frac{1}{\sqrt{x_2}} + \int_0^{x_2} \frac{f_2}{\sqrt{x_2 - \xi}} d\xi + \sqrt{\frac{\pi}{2\lambda}} f_2 .$$

Taking the Laplace transform and simplifying, we have

$$F_2 = \frac{c_0}{A} \sqrt{\frac{2\lambda}{\pi}} \frac{1}{\sqrt{s} (\sqrt{s} + \sqrt{s\lambda})} - \frac{c_1}{\sqrt{2\lambda}} \frac{1}{(\sqrt{s} + \sqrt{2\lambda})} , \quad (A.4.3)$$

where  $F_2$  is the Laplace transform of  $f_2$ . Taking the inverse Laplace transform, we find for  $f_2$ ,

$$f_2(x_2) = \frac{c_0}{A} \sqrt{\frac{2\lambda}{\pi}} e^{2\lambda x_2} \text{erfc} \sqrt{2\lambda x_2} - \frac{c_1}{\sqrt{2\lambda}} \left[ \frac{1}{\sqrt{\pi x_2}} - \sqrt{2\lambda} e^{2\lambda x_2} \text{erfc} \sqrt{2\lambda x_2} \right]$$

(A.4.4)

APPENDIX B

EXPERIMENTAL RESULTS AND ANALYSIS

B.1 Sample Data Corresponding to Figure 3.14 Regression Line

Run No.	Tunnel Velocity	Tunnel Pressure psia	Cavity Pressure psia	$\sigma$ based on $P_C$	Freq. of Full Hz	Angle of Attack degrees	$\Delta\sigma$ deg	$\sigma$ corrected	$\sigma/a$	Alt. $\mu_r$ , psia	$\tau$ msec	$\alpha_1$ ppm
51	24.60	3.0	0.478	0.610	10	5.850	2	0.54	5.34	14.22	148	11
52	24.60	3.1	0.459	0.633	10	7.587	2	0.57	4.34	14.22	148	11
53	24.54	3.1	0.482	0.630	10	10.030	2	0.57	3.27	14.22	148	11
54	24.54	2.3	0.494	0.433	10	12.000	2	0.37	1.78	14.22	148	11
55	24.66	4.1	0.499	0.864	10	14.150	2	0.81	3.28	14.22	148	11
56	24.66	3.8	0.506	0.700	10	16.500	2	0.73	2.54	14.22	148	11
57	24.54	3.7	0.520	0.763	10	18.120	2	0.71	2.25	14.22	148	11
58	24.54	3.4	0.525	0.690	10	20.040	2	0.64	1.82	14.22	148	11

### B.2 Measurement of Free Air Content in the Test Section

The change in acoustic velocity as a function of free gas concentration is given as [see for example, John M. Killen and John F. Ripken, "A Water Tunnel Air Content Meter," St. Anthony Falls Hydraulic Laboratory Report No. 70]

$$\frac{C_x}{C_v} = \sqrt{\frac{P_a}{xE_w + (1 - x)P_a}} \quad (B.2.1)$$

where

$C_x$  = velocity of sound in the mixture

$C_v$  = velocity of sound in water

$x$  = concentration of free gas by volume

$E_w$  = bulk modulus of pure water

$P_a$  = absolute pressure in the test section.

In order that Eq. (B.2.1) applies, it must be established that the gas bubble sizes present in the test section are smaller than the resonant size corresponding to the frequency of the measuring acoustic signal. From Eq. (B.2.1) we can obtain an expression for the concentration of gas,

$$x = \frac{P_a \left( \frac{C_v^2}{C_x^2} - 1 \right)}{(E_w - P_a)} \quad (B.2.2)$$

Example: For a measured time delay of 140 microseconds at a tunnel test section pressure of 4 psia, the concentration of gas is determined as follows:

The time delay  $T_d$  may be expressed as

$$T_d = \frac{1.443/12}{5000} + \frac{6/12}{C_x} \quad (B.2.3)$$

where the first term represents the time delay through the lucite walls and the second term represents the time delay through gas water mixture.

Hence, for  $T_d = 140$  microseconds,  $C_x$  is calculated from Eq. (B.2.3) to be

$$C_x = 4312 \text{ ft/sec} .$$

The bulk modulus for pure water is  $32 \times 10^4$  psi. Hence from Eq. (B.2.2),

$$x = \frac{4 \left( \left( \frac{5000}{4312} \right)^2 - 1 \right)}{\left( 32 \times 10^4 - 4 \right)} = 4.3 \times 10^{-6}$$

i.e.,  $x = 4.3$  ppm by volume.

B.3 Analysis of Experimental Error(1) Cavitation Number

The cavitation number  $\sigma$  is defined as

$$\sigma = \frac{p_o - p_c}{1/2 \rho_\infty U_\infty^2} , \quad (B.3.1)$$

where

$p_o$  = test section pressure

$p_c$  = steady cavitation pressure

$\rho_\infty$  = density of tunnel water

$U_\infty$  = free stream velocity in the test section.

From Eq. (B.3.1),

$$\ln \sigma = \ln(p_o - p_c) - \ln \frac{1}{2} - \ln \rho_\infty - 2 \ln U_\infty ,$$

so that

$$\frac{\Delta \sigma}{\sigma} = \frac{\Delta(p_o - p_c)}{(p_o - p_c)} - \frac{2 \Delta U_\infty}{U_\infty} , \quad (B.3.2)$$

where the  $\Delta$  before a quantity signifies a small error involved in measuring/estimating that quantity.

The maximum error in calculating  $(p_o - p_c)$  is 0.12 psi. The minimum value of  $(p_o - p_c)$  during the experiments is seen to be 2.7 psi. The maximum error in calculating the free stream velocity is 0.05 ft/sec. The minimum value of  $U_\infty$  during the experiments is 25 ft/sec. With these extreme values, the maximum absolute error in estimating the cavitation number may be calculated as

$$\left| \frac{\Delta \sigma}{\sigma} \right| = \frac{0.12}{1.7} + \frac{0.1}{25} = 0.048 .$$

Hence the error in estimating the cavitation number is at the most 4.8%.

(2) Concentration of Gas

From Eq. (B.2.2) the concentration of gas is given by

$$x = \frac{p_a}{(E_w - p_a)} \left[ \left( \frac{c_v}{c_x} \right)^2 - 1 \right] , \quad (B.3.2)$$

where

$p_a$  = test section pressure

$E_w$  = bulk modulus of pure water

$c_v$  = speed of sound in pure water

$c_x$  = speed of sound in the mixture.

We want to bound the error in the estimation of concentration of gas when there is a known uncertainty in the measurement of speed of sound in the mixture.

From Eq. (B.2.2),

$$\left| \frac{\Delta x}{x} \right| = \frac{2 \left( \frac{c_x}{c_v} \right)}{1 - \left( \frac{c_x}{c_v} \right)^2} + \frac{\Delta p_a}{p_a} , \quad (B.3.3)$$

noting that  $E_w \gg p_a$ .

The maximum error in measuring the speed of sound in the mixture is 30 ft/sec. The minimum speed of sound in the mixture during the experiments is seen to be about 4000 ft/sec. The error in reading the tunnel pressure is 0.1 psi and the minimum tunnel pressure is 3 psia. Hence from Eq. (B.3.3),

$$\left| \frac{\Delta x}{x} \right| = \frac{2 \left( \frac{30}{4000} \right)}{1 - \left( \frac{4000}{5000} \right)^2} + \frac{0.1}{3.0} \sim 8\% .$$

Therefore the bound on the error in estimating the concentration of gas is 8%.

#### B.4 Wall Effect Correction for Cavitation Number

The technique described by Hsu (24) is used in obtaining the true cavitation number. Following Hsu, the linearized results for a two-dimensional flat plate hydrofoil with trailing cavity in a closed tunnel are:

$$\sigma_1 = \left( \frac{\lambda_f}{1 - \lambda_f} \right) \lambda_w \quad , \quad (B.4.1)$$

where

$$\lambda_f = 2\alpha \left( \frac{L}{c} - 1 \right)^{1/2} \quad , \quad (B.4.2)$$

and

$$\lambda_w = \frac{1}{2} \left( \frac{2\pi L}{H} \right)^{1/2} \left[ \cosh \left( \frac{\pi L}{H} \right) + 1 \right]^{1/4} \left[ \cosh \left( \frac{\pi L}{H} \right) - 1 \right]^{-1/4} \quad . \quad (B.4.3)$$

In the above equations,

$\alpha$  = angle of attack

$c$  = chord length of foil

$l$  = cavity length

$L = l + c$

$H$  = tunnel diameter.

Having found  $\sigma_1$  from Eq. (B.4.1), the true cavitation number is found from

$$\sigma = \frac{(2 + \sigma_1)\sigma_1}{2 + 2\sigma_1 + \sigma_1^2} \quad . \quad (B.4.4)$$

Example: The cavitation number calculated from the measured cavity pressure is 0.75. The cavity length  $l$  is 7.32 cms. The chord length of the foil is 7.14 cms. The angle of attack is 10 degrees.

From Eq. (B.4.2),

$$\lambda_f = 2\left(\frac{\pi}{180} 10\right) \left[\frac{14.46}{7.14} - 1\right]^{1/2}$$

$$\lambda_f = 0.353 .$$

From Eq. (B.4.3) for  $\frac{\pi L}{H} = 2.981$ ,

$$\lambda_w = \frac{1}{2} (2 \times 2.981)^{1/2} [\cosh(2.981) + 1]^{1/4} [\cosh(2.981) - 1]^{1/4}$$

$$\lambda_w = 2.34 .$$

From Eq. (B.4.1),

$$\sigma_1 = \frac{0.353}{1 - 0.353} 2.34 = 1.277 .$$

From Eq. (B.4.4),

$$\sigma = \frac{(2 + 1.277)1.277}{2 + 2 \times 1.277 + 1.277^2}$$

$$\sigma = 0.676 .$$

## APPENDIX C

## DETAILS OF UNSTEADY DIFFUSION ANALYSIS

### C.1 Fundamental Solution of Eq. (4.13b)

Fundamental solution to Equation (4.13b) for an oscillating unit source at the origin:

Equation (4.13b) is

$$\frac{\partial \bar{c}_u}{\partial t} + U_\infty \frac{\partial \bar{c}_u}{\partial x} = v_t \left( \frac{\partial^2 \bar{c}_u}{\partial x^2} + \frac{\partial^2 \bar{c}_u}{\partial y^2} \right) . \quad (C.1.1)$$

We assume that the cavity length fluctuations are harmonic. Then, the entire concentration field  $\bar{c}_u$  is harmonic so that

$$\bar{c}_u(x, y, t) = c(x, y) e^{j\omega t} , \quad (C.1.2)$$

where  $\omega$  is the circular frequency of harmonic oscillations and  $j = \sqrt{-1}$ . It is to be noted that only the real part of the analysis that follows is physically pertinent. Substituting Equation (C.1.2) in (C.1.1), we obtain

$$j\omega c + U_\infty \frac{\partial c}{\partial x} = v_t \left( \frac{\partial^2 c}{\partial x^2} + \frac{\partial^2 c}{\partial y^2} \right) . \quad (C.1.3)$$

We normalize the  $x$  and  $y$  coordinates by the flat plate chord  $\bar{b}$  and simplify Eq. (C.1.3) as

$$2 j k c + 2 \frac{\partial c}{\partial x'} = \frac{1}{R} \left( \frac{\partial^2 c}{\partial x'^2} + \frac{\partial^2 c}{\partial y'^2} \right) , \quad (C.1.4)$$

where  $x' = \frac{x}{\bar{b}} , \quad (C.1.5)$

$$y' = \frac{v}{\bar{v}} b , \quad (C.1.6)$$

$$k = \frac{\omega b}{U_\infty} = \text{reduced frequency}, \quad (C.1.7)$$

$$R = \frac{U_\infty b}{2v_t} = \text{Diffusive Reynolds' number} \quad (C.1.8)$$

To solve Equation (C.1.4) we replace the Laplacian on the right-hand side by its counterpart in plane polar coordinates when variations only in the radial direction are permitted. Then,

$$2jkcR + 2R \frac{\partial c}{\partial x} = \frac{\partial^2 c}{\partial r^2} + \frac{1}{r} \frac{\partial c}{\partial r} , \quad (C.1.9)$$

where

$$\left. \begin{array}{l} x = r \cos \theta \\ y = r \sin \theta \\ \theta = \tan^{-1}(\frac{y}{x}) \end{array} \right\} . \quad (C.1.10)$$

It must be noted that the coordinates  $x$  and  $r$  appearing in Eq. (C.1.9) are dimensionless.

By letting

$$\frac{x}{2R} = s , \quad (C.1.11)$$

Equation (C.1.9) can be written as

$$2cjkR + \frac{\partial C}{\partial s} = \frac{\partial^2 C}{\partial r^2} + \frac{1}{r} \frac{\partial C}{\partial r} . \quad (C.1.12)$$

We now use separation of variables to solve Equation (C.1.12). By substituting

$$C(s, r) = S(s)X(r) , \quad (C.1.13)$$

Equation (C.1.12) may be written as

$$2jkR + \frac{S'}{S} = \frac{X''}{X} + \frac{1}{r} \frac{X'}{X} = \kappa_1^2 , \quad (C.1.14)$$

where  $\kappa_1^2$  is an unknown constant. Therefore,

$$X'' + \frac{X'}{r} - \kappa_1^2 X = 0 , \quad (C.1.15)$$

$$\frac{S''}{S} = \kappa_1^2 - 2jkR . \quad (C.1.16)$$

Equation (C.1.15) may be rewritten as

$$r^2 \frac{d^2 X}{dr^2} + r \frac{dX}{dr} - \kappa_1^2 r^2 X = 0 , \quad (C.1.17)$$

and the solution for  $\kappa_1^2 > 0$  is

$$X(r) = A_1 I_0(\kappa_1 r) + A_2 K_0(\kappa_1 r) , \quad (C.1.18)$$

where  $A_1$  and  $A_2$  are constants and  $I_0$  and  $K_0$  are the modified Bessel's function of zeroth order of first and second kind respectively.

Note: Negative values of  $\kappa_1^2$  yield functions

$J_0$  and  $Y_0$  (Bessel's function of zeroth order of first and second kind respectively) which do not satisfy the boundary conditions.

Note 2:  $\kappa_1^2 = 0$  yields a logarithmic function which again does not satisfy the boundary conditions.

For large distances from the origin, the function  $c(s, r)$  should vanish.

Hence, we set  $A_1 = 0$  in Equation (C.1.18). Therefore,

$$X(r) = A_2 K_0(\kappa_1 r). \quad (C.1.19)$$

The solution of Equation (C.1.16) is easily written as

$$S(s) = B e^{(\kappa_1^2 - 2jkR)s}, \quad (C.1.20)$$

where  $B$  is an unknown constant. Hence, from Equation (C.1.13),

$$C(s, r) = B_1 e^{(\kappa_1^2 - 2jkR)s} K_0(\kappa_1 r), \quad (C.1.21)$$

where  $B_1 = BA_2$  is a new unknown constant. The arbitrary constant  $B_1$  and the separation constant  $\kappa_1$  are obtained by requiring that Eq. (C.1.21) go to the proper steady state limit (8) when the reduced frequency  $k$  goes to zero. This results in

$$B_1 = \frac{1}{2\pi\rho\nu}, \quad (C.1.22)$$

and

$$\kappa_1 = R. \quad (C.1.23)$$

Hence, for a unit oscillating source,

$$c(x, r) = \frac{1}{2\pi\rho\nu} e^{-jkx} e^{Rx} K_0(Rr) \quad (C.1.24)$$

### C.2 Inverse Laplace Transform

To obtain the inverse Laplace Transform of the function

$$F(s, t) = \frac{0 \sqrt{s + jk}}{s [\sqrt{2R - jk} + \sqrt{s + jk}]} . \quad (C.2.1)$$

Let

$$a = jk, \quad (C.2.2)$$

and

$$b = \sqrt{2R - jk} . \quad (C.2.3)$$

Then

$$F(s, t) = \frac{0 \sqrt{s + a}}{s [\sqrt{s + a} + b]} , \quad (C.2.4)$$

$$F(s, t) = Q \left[ \frac{\sqrt{s + a} + b}{s [\sqrt{s + a} + b]} - \frac{b}{s [\sqrt{s + a} + b]} \right] , \quad (C.2.5)$$

or

$$F(s, t') = Q \left[ \frac{1}{s} - \frac{b}{s [\sqrt{s + a} + b]} \right] . \quad (C.2.6)$$

Let

$$H(s) = \frac{b}{s [\sqrt{s + a} + b]} \quad (C.2.7)$$

or

$$H(s) = \frac{b [\sqrt{s + a} - b]}{s [s + a - b^2]}$$

Denote

$$\bar{a} = a - b^2 . \quad (C.2.8)$$

Then,

$$H(s) = \frac{b \sqrt{s+a}}{s(s+\bar{a})} - \frac{b^2}{s(s+\bar{a})} . \quad (C.2.9)$$

Denote

$$Z(s) = \frac{b \sqrt{s+a}}{s(s+\bar{a})} \quad (C.2.10)$$

$$\frac{Z(s)}{b} = \frac{s + \bar{a} + b^2}{s(s+\bar{a}) \sqrt{s+a}}$$

$$\frac{Z(s)}{b} = \frac{1}{s \sqrt{s+a}} + \frac{b^2}{s(s+\bar{a}) \sqrt{s+a}}$$

$$\frac{Z(s)}{b} = \frac{1}{s \sqrt{s+a}} + \frac{b^2}{\bar{a}} \left( \frac{1}{s \sqrt{s+a}} - \frac{1}{(s+a) \sqrt{s+a}} \right) . \quad (C.2.11)$$

Substituting Equation (C.2.11) in (C.2.9), one has

$$H(s) = \frac{b}{s \sqrt{s+a}} + \frac{b^3}{\bar{a}s \sqrt{s+a}} - \frac{b^3}{\bar{a}} \frac{1}{(s+\bar{a}) \sqrt{s+a}} - \frac{b^2}{s(s+\bar{a})} . \quad (C.2.12)$$

Substituting Equation (C.2.12) in Equation (C.2.6), one gets

$$F(s,t) = Q \left[ \frac{1}{s} - \frac{b}{s \sqrt{s+a}} - \frac{b^3}{\bar{a}s \sqrt{s+a}} + \frac{b^3}{\bar{a}(s+\bar{a}) \sqrt{s+a}} + \frac{b^2}{s(s+\bar{a})} \right] . \quad (C.2.13)$$

Taking the inverse Laplace Transform on both the sides, one finds

$$f(x,t) = Q \left[ \frac{a}{\bar{a}} - \frac{b^2}{\bar{a}} e^{-\bar{a}x} \operatorname{erfc} b \sqrt{x} - \frac{b \sqrt{a}}{\bar{a}} \operatorname{erf} \sqrt{\bar{a}x} \right] . \quad (C.2.14)$$

C.3 Integral Evaluation

Equation (4.25) is

$$\frac{dM}{dt} = \int_0^{I(t)} f(x, t) dt, \quad (C.3.1)$$

where

$$f(x, t) = \frac{0}{a} \left( a - b^2 e^{-ax} \operatorname{erfc} b \sqrt{x} - b \sqrt{a} \operatorname{erf} \sqrt{ax} \right). \quad (C.3.2)$$

Substituting Equation (C.3.2) in (C.3.1),

$$\frac{dM}{dt} = \frac{0}{a} \left[ \int_0^{I(t)} adx - b^2 \int_0^{I(t)} e^{-ax} \operatorname{erfc} b \sqrt{x} dx - b \sqrt{a} \int_0^{I(t)} \operatorname{erf} \sqrt{ax} dx \right]. \quad (C.3.3)$$

Let

$$I_1 = \int_0^{I(t)} e^{-ax} \operatorname{erfc} b \sqrt{x} dx, \quad (C.3.4)$$

and

$$I_2 = \int_0^{I(t)} \operatorname{erf} \sqrt{ax} dx. \quad (C.3.5)$$

The integral in Equation (C.3.4) may be evaluated by parts.

$$I_1 = \operatorname{erfc} b \sqrt{x} \frac{e^{-ax}}{-a} \Big|_0^{I(t)} + \frac{1}{a} \int_0^{I(t)} e^{-ax} (-1) \frac{b}{\sqrt{\pi}} \frac{e^{-b^2 x}}{\sqrt{x}} dx$$

$$I_1 = \frac{1}{a} - \frac{e^{-al} \operatorname{erfc} b}{a} - \frac{b}{a \sqrt{\pi}} \int_0^l \frac{e^{-ax}}{\sqrt{x}} dx . \quad (C.3.6)$$

By setting  $ax = u^2$  in Equation (C.3.6), we can show that

$$I_1 = \frac{1}{a} - \frac{e^{-al} \operatorname{erfc} b}{a} - \frac{b}{a \sqrt{a}} \operatorname{erf} \sqrt{al} . \quad (C.3.7)$$

The integral in Equation (C.3.5) can be obtained by parts,

$$I_2 = x \operatorname{erf} \sqrt{ax} \Big|_0^l - \int_0^l x \frac{\frac{1}{a} e^{-ax}}{\sqrt{\pi}} dx$$

i.e.,

$$I_2 = l \operatorname{erf} \sqrt{al} - \frac{\sqrt{a}}{\sqrt{\pi}} \int_0^l \sqrt{x} e^{-ax} dx . \quad (C.3.8)$$

The integral in Equation (C.3.8) may be evaluated again by parts and the result is

$$I_2 = l \operatorname{erf} \sqrt{al} + \frac{l}{\pi a} e^{-al} - \frac{1}{2a} \operatorname{erf} \sqrt{al} . \quad (C.3.9)$$

Hence from Equation (C.3.3),

$$\begin{aligned} \frac{dM}{dt} = & \frac{Q}{a} \left[ al - \frac{b^2}{a} + \frac{b^2}{a} e^{-al} \operatorname{erfc} b \sqrt{l} + \frac{b^3}{a \sqrt{a}} \operatorname{erf} \sqrt{al} \right. \\ & \left. + \frac{b}{2 \sqrt{a}} \operatorname{erf} \sqrt{al} - b \frac{l}{\pi} e^{-al} - b \sqrt{a} l \operatorname{erf} \sqrt{al} \right] . \quad (C.3.10) \end{aligned}$$

## APPENDIX D

## SENSITIVITY ANALYSIS FOR MASS DIFFUSION RATE

The quasi steady mass flow rate across a two-dimensional cavity is, from Equation (4.28)

$$\dot{M}_{QS} = 4A_T R c_0 \left( \frac{e^{2R\tilde{z}} \operatorname{erfc} \sqrt{2R\tilde{z}}}{2R} + \sqrt{\frac{2\tilde{z}}{\pi R}} - \frac{1}{2R} \right) \quad (4.28)$$

For large values of the argument  $2R\tilde{z}$ ,

$$e^{2R\tilde{z}} \operatorname{erfc} 2R\tilde{z} = \frac{1}{\sqrt{\pi}} \left( \frac{1}{\sqrt{2R\tilde{z}}} - \frac{1}{2(2R\tilde{z})}^{3/2} + \dots \right). \quad (D.1)$$

Substituting Eq. (D.1) in Eq. (4.28) above,

$$\dot{M}_{QS} = \frac{4A_T c_0}{\sqrt{\pi}} \left( \sqrt{2R\tilde{z}} - \frac{\sqrt{\pi}}{2} + \frac{1}{2\sqrt{2R\tilde{z}}} - \frac{1}{4(2R\tilde{z})}^{3/2} + \dots \right). \quad (D.2)$$

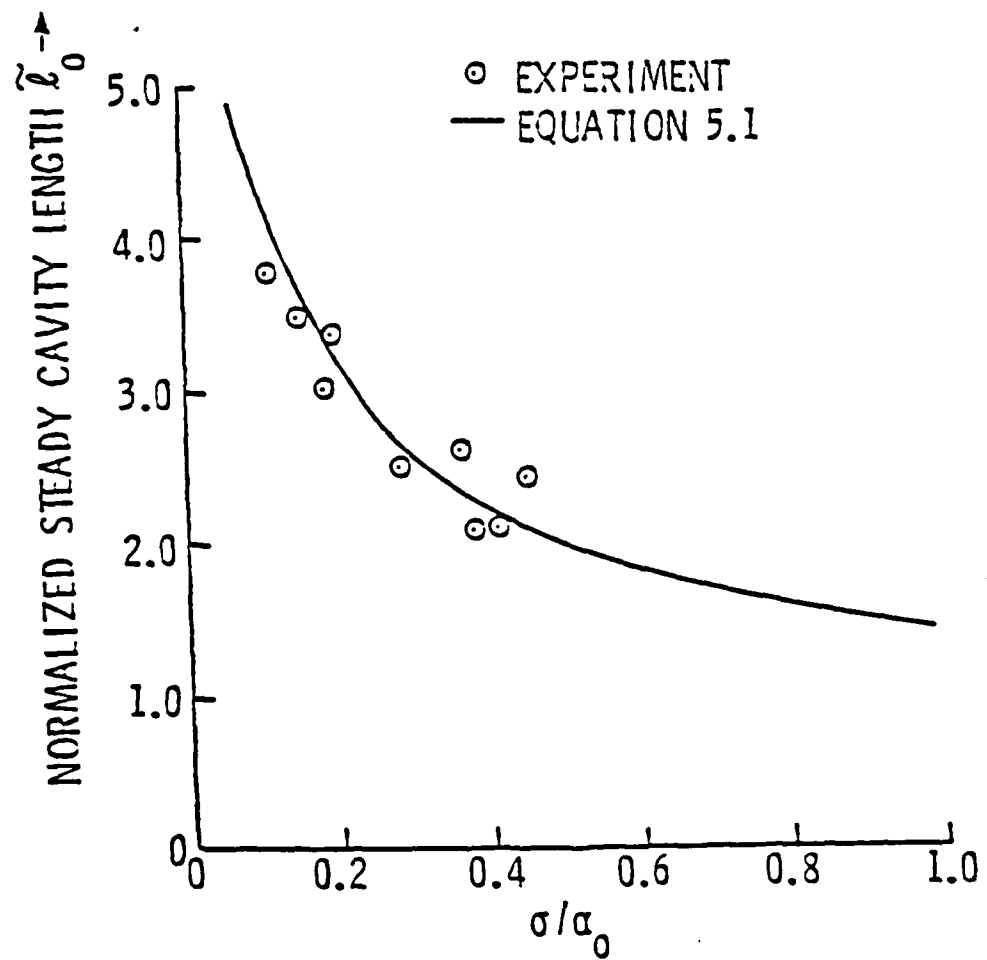
Retaining only the first term within the brackets in Eq. (D.2), we take the logarithm on both sides and then differentiate to obtain

$$\frac{\dot{M}_{QS}}{\dot{M}_{QS}} = \frac{\Delta c_0}{c_0} + \frac{\Delta \tilde{z}_0}{2\tilde{z}_0}. \quad (D.3)$$

and this is the basis of the order of magnitude discussion surrounding Eq. (4.31) of Chapter 4.

## APPENDIX E

## UNSTEADY ENTRAINMENT DATA AND CALCULATIONS

E.1 Quasisteady Concentration Fluctuation Amplitude

## E.2 Quasi-Steady Concentration Fluctuation Amplitude

Equation (5.2) is

$$\frac{p_{G_0}}{p_v} = -0.0976 \frac{\sigma}{\alpha_0} + 0.74 . \quad (5.2)$$

Taking logarithms on both sides and then differentiating Eq. (5.2), one obtains

$$\Delta p_{G_0} = 0.0976(\sigma/\alpha_0)(\Delta\alpha_0/\alpha_0) p_v . \quad (E.2.1)$$

From Eq. (2.9), the concentration difference  $c$  expressed in ppm by modes is

$$c_0 = \alpha_1 - \frac{p_{G_0}}{\beta} , \quad (2.9)$$

so that

$$\frac{\Delta c_0}{c_0} = - \frac{\Delta p_{G_0}/\beta}{c_0} .$$

Substituting from Equation (E.2.1),

$$\frac{\Delta c_0}{c_0} = \frac{-0.0976 (\sigma/\alpha_0)(\Delta\alpha_0/\alpha_0)(p_v/\beta)}{\alpha_1 - (p_v/\beta)(0.74 - 0.0976 \sigma/\alpha_0)} . \quad (E.2.2)$$

### E.3 Evaluation of $\frac{\partial m}{\partial t}$ in Eq. (5.16b)

Let  $V$  = total volume of cavity in cubic feet,

$m$  = total mass of gas in the cavity, in slugs.

Then, at any instant, the equation of state for the gas within the cavity is

$$p_G V = mRT \quad , \quad (E.3.1)$$

Where  $R$  is the specific gas constant and  $R = 1718 \text{ ft.lb./slug } {}^{\circ}\text{R}$  for air.

Assuming that the temperature of gas within the cavity remains constant, Eq. (E.3.1) may be partially differentiated with respect to time to obtain

$$\frac{\partial m}{\partial t} = \frac{1}{RT} \left( V \frac{\partial p_G}{\partial t} + p_G \frac{\partial V}{\partial t} \right) \quad . \quad (E.3.2)$$

From Eq. (5.13a), the cavity volume  $V$  is

$$V = \frac{\pi a^2}{2} \left( \tilde{z} - \frac{1}{2} \right) \quad , \quad (5.13a)$$

where  $a = a_0 (1 + \Delta \alpha e^{j\omega t})$

and  $\tilde{z} = \tilde{z}_0 (1 + \epsilon e^{j(\omega t + \phi)}) \quad .$

Differentiating Eq. (5.13a) partially with respect to  $t$  and neglecting terms of order  $\epsilon \Delta \alpha$ , one obtains after suppressing the  $e^{j\omega t}$  factor

$$\frac{\partial V}{\partial t} = \frac{a_0 \pi b k' q_c j}{2} \left[ \tilde{z}_0 \epsilon e^{j\phi} + \left( \tilde{z}_0 - \frac{1}{2} \right) \Delta \alpha \right] \quad . \quad (E.3.3)$$

Now, from Eq. (4.17), the cavity gas pressure  $p_G(t)$  is

$$p_G(t) = p_{G_0} (1 + \delta e^{j(\omega t + \phi_a)}) . \quad (4.17)$$

Differentiating Eq. (4.17) partially with respect to  $t$  and suppressing  $e^{j\omega t}$  factor,

$$\frac{\partial p_G}{\partial t} = \frac{p_{G_0} k' q_c \delta j}{\bar{b}} e^{j\phi_a} . \quad (E.3.4.)$$

Substituting Eqs. (E.3.3) and (E.3.4) in Eq. (E.3.2), one obtains

$$\frac{\partial m}{\partial t} = \frac{\pi \alpha_0 \bar{b} p_{G_0} k' q_c j}{2RT} [(\bar{\iota}_0 - \frac{1}{2})(\delta e^{j\phi_a} + \Delta \alpha) + \bar{\iota}_0 \epsilon e^{j\phi}] . \quad (E.3.5)$$

#### E.4 Unsteady Entrainment Calculated Data

The sample calculations below show how the tabulated results were obtained for one case at a 10 Hz frequency and 2° peak to peak foil amplitude.

From Eq. (5.3),

$$\dot{M}_{d_o} = \frac{4\rho v_t c}{\sqrt{\pi}} [\sqrt{2R\tilde{i}_{u_o}} + \sqrt{2R\tilde{i}_{l_o}}] . \quad (5.3)$$

For  $R = \frac{U_{\infty b}}{2v_t} = 2500$ ,  $c = 10 \text{ ppm}$ ,  $\sigma/\sigma_o = 2.7$ ,

$$\tilde{i}_{u_o} = 2.32, \quad \tilde{i}_{l_o} = 1.32, \quad \dot{M}_{d_o} = 1.46 \times 10^{-5} \text{ slugs/sec ft}$$

From Eq. (E.2.2),

$$\frac{\Delta c_o}{c_o} = -0.0025$$

$$\frac{\epsilon}{2 \tilde{i}_{u_o} \tilde{i}_{l_o}} = \frac{0.165 \times 0.707}{2 \sqrt{2.32 \times 1.32}} = 0.033$$

The last term in Eq. (5.21) is

$$\frac{\pi \alpha_o \bar{b} p_{G_o} k' q_c j}{2RT \dot{M}_{d_o}} [(\tilde{i}_{u_o} - \frac{1}{2})(\Delta a + \delta e^{j\phi_a}) + \tilde{i}_{u_o} \epsilon e^{j\phi}] .$$

From Eq. (5.5)  $\phi = k' = 0.03$  radians = 1.72°. From Equation (5.2) and (E.2.1),  $\delta = 0.05$ .

From Eq. (5.15),

$$v = (\epsilon e^{j\phi} + \Delta\alpha - \frac{\Delta\alpha_0}{2i_{u_0}}) / (1 - \frac{1}{2i_{u_0}})$$

$$v = 0.239 + 0.006j = 0.239 @ 1.44^\circ$$

$$\phi_a = 180^\circ + 1.44 = 181.44^\circ .$$

From Fig. (3.14), for  $\sigma/\alpha_0 = 2.7$ ,  $p_{G_0} = 72 \text{ lb/sq.ft.}$

Substituting the values, the last term in Eq. (5.21) is  
 $-0.002 + 0.065j$ , as tabulated.

E.4 Unsteady Entrainment Calculated Data

$k'$	$\epsilon$	$\frac{\Delta c_0}{c_0}$	$\frac{\epsilon}{\sqrt{2\lambda_{10}\lambda_{10}}}$	$\dot{M}_{10}$ Slug/sec ft	$\frac{\partial m}{\partial t} \div \dot{M}_{10}$	$\dot{E} / \dot{M}_{10}$
0.030	0.165	-0.0025	0.033	$1.46 \times 10^{-5}$	-0.002 + 0.065j	$1 + (0.047 - 0.065j)$
0.050	0.210	-0.0025	0.041	$1.46 \times 10^{-5}$	-0.004 + 0.142j	$1 + (0.043 - 0.142j)$
0.135	0.180	-0.0025	0.035	$1.46 \times 10^{-5}$	-0.031 + 0.318j	$1 + (0.056 - 0.318j)$
0.230	0.100	-0.0025	0.020	$1.46 \times 10^{-5}$	-0.055 + 0.298j	$1 + (0.080 - 0.298j)$

VITA

Krishnaswamy Ravindra is a native of India. He graduated from The University of Mysore, India, in 1971 with a Bachelor's degree in Mechanical Engineering. In 1973 he obtained a Master's degree in Aeronautical Engineering from the Indian Institute of Science, Bangalore. He was a graduate research assistant at the Applied Research Laboratory of The Pennsylvania State University from December 1976 to September 1982.

He is an associate member of ASME and SAE and a member of AIAA. He is also a member of Phi Kappa Phi, Tau Beta Pi, Sigma Xi and honorary member of Alpha Eta Rho. He is a registered Professional Engineer in the state of New York.

He has been a faculty member in Aeronautics and Airway Science at Dowling College, Long Island, since February 1983.